Dynamic Ball & Socket Joint Force Simulator

BY

C2011
Ryan Farmer

Submitted to the graduate degree program in Mechanical Engineering and the Graduate Faculty of the University of Kansas in partial fulfillment of the requirements for the degree of Master of Science.

Committee:

Dr. Terence E. McIff
Chairperson

Dr. Kenneth J. Fischer

Dr. Lorin P. Maletsky

Date defended: 4/28/2010

The Thesis Committee for Ryan Farmer certifies that this is the approved version of the following thesis:

Dynamic Ball & Socket Joint Force Simulator

Committee:

Dr. Terence E. McIff
Chairperson

Dr. Kenneth J. Fischer

Dr. Lorin P. Maletsky

Date approved: 5/11/2011

TABLE OF CONTENTS

LIST OF FIGURES

LIST OF TABLES

Abstract

The stability of an implant in the bone, one factor in joint replacement survival, is usually tested using biaxial fatigue loading. These loading protocols do not replicate physiological loading conditions. The Dynamic Ball and Socket Joint Force Simulator (DBSJFS) was designed to apply physiological loads through an articular surface to study implant stability.

The DBSJFS was custom built to integrate with a MTS 858 Mini Bionix machine. The design allows femoral components to be tested dynamically in three dimensions with four degrees of freedom. Two rotary actuators turn the distal end of the femur around perpendicular axes while the linear actuator applies a downward force through the centroid of the femoral component head. The rotations of the femur and the dynamic loading patterns are correlated together to replicate the resultant joint force in the hip. Procedures replicating the gait cycles of a person walking normally, going up and down stairs, and sitting down and standing up were developed using component hip force data taken from *HIP98*, a study performed in Berlin, Germany by Bergmann that recorded hip joint forces *in vivo* using instrumented femoral stems implanted into patients.

The DBSJFS can operate at $1/3^{rd}$ physiological speed under loads representing a 900 N individual. At $1/5^{th}$ physiological speed and 700 N loads, the average and maximum absolute error produced in each channel for the normal walking gait are as follows: Y' axis motor 0.63 deg, 1.49 deg; X' axis motor 0.45, 1.39 deg; linear actuator 10.78, 27.04 N.

Acknowledgements

There were many people who helped me complete my research and thesis. I am grateful to them all and appreciate the time and effort they contributed to this project. I would first like to recognize my thesis supervisor, Dr. Terence McIff, for giving me the opportunity to be one of his graduate students. I learned a great deal while working in his laboratory and appreciate all the time he spent helping me work through the challenges of this project. Next, I would like to thank Patrick Moodie for the excellent input and ideas that he always had. You helped make the laboratory a great place to work. I would like thank Dr. Kelly Hendricks for his time and contributions to the project and for allowing me to shadow him in clinic and surgery. I want to thank Phyllis Robinson for her contributions in helping the research laboratory operate day to day. Next, I would like to thank Dr. David Anderson for his efforts in helping to make new parts for the hip simulator when it broke during the early phases of testing. Also, I want to thank Dr. Hugh Brock for teaching me how to properly insert a femoral component into a femur. Next, I want to thank my committee members Dr. Kenneth Fischer and Dr. Lorin Maletsky. Thank you both for the guidance and feedback with this project. You both were also two of the best teachers that I have had, and I learned much in each of your classes. I would also like to thank two faculty members from Kansas State University, Dr. Asad Esmaeily and Dr. Chris Lewis. Dr. Esmaeily, thank you for helping me with the design of the frame, and Dr. Lewis, thank you for assisting me with the mathematics involved with this project.

Lastly, I want to thank my friends and family for all their support. Mom and Dad, thank you for everything that you have done. I would not have been able to accomplish the things I have in life without your support. You helped mold me into who I am today, and I grateful for everything that you both have done for me. Thank you for always being there to provide guidance, wisdom, and love. Kelli, I will never be able to thank you enough for all the late nights that you spent with me in the laboratory helping me finish this project. Thank you for helping me write and edit this thesis and for providing love and support. I could not have done it without you.

Notation and Conventions

Avg	average
BW	body weight
deg	degree
DJD	Degenerative Joint Disease
Err	Error
F_R, Fr	resultant force
GDS	Going down stairs
GU and DS	Going up and down stairs
GUS	Going up stairs
Max	Maximum
N	Newtons
Phys, phys	physiological speed
SD	Sitting down
Sitting Down	the movement of stand to sit
SU	Standing up
Standing Up	the movement of sit to stand
SU and SD	Standing up and sitting down
THA	Total Hip Arthroplasty
WN	Walking normally, defined in HIP98 by Bergmann as 1.09 m/s
X’ axis	nonstationary axis of the dynamic ball & socket joint force simulator
Y’ axis	stationary axis of the dynamic ball & socket joint force simulator

Chapter 1 INTRODUCTION

Chapter 1 INTRODUCTION

1.1 Total Hip Arthroplasty

The hip is a ball and socket joint composed of the acetabulum and femoral head. The configuration of the human hip joint allows a great range of motion along with excellent stability. Normal motion for a person is 110°-120° for flexion, 10°-15° for extension, 30°-50° for abduction, 25°-30° for adduction, 30°-40° for internal rotation, and 40°-60° for external rotation [1]. Even though the hip has great inherent strength and stability, individuals may often experience pain and reduced range of motion in the hip as they get older due to degenerative joint disease (DJD). The primary causes of DJD are osteoarthritis, rheumatoid arthritis, and osteonecrosis. One of the surgical options available to patients to treat this disease is a total hip arthroplasty (THA).

THA is a surgical procedure in which the hip joint is replaced with an acetabulum cup and a femoral stem prosthetic. This requires several steps. First, the femoral head is removed by cutting through the neck of the femur with a saw. Next, a femoral stem is placed in the proximal end of the femur after the diaphysis has been reamed and/or rasped to the proper shape. Finally, an acetabular cup is secured into the coax after the acetabulum has been properly shaped. The purpose of this procedure is to restore the function and the normal range of motion to the hip. THAs began to have reproducible results in the 1960s when surgical treatment for end stage DJD of the hip was developed by Sir John Charnley [2]. Over the last half century,

THAs have become one of the most successful surgical endeavors. This success is due in part to the evolution of surgical technique and implant design.

1.1.1 Growth Rate

With improved geometrical design of current implants and use of enhanced materials and advanced surgical methods, conservative prosthetic hip implants can now be expected to last 10 to 20 years [3]. This success and an aging population in the United States means this area of orthopedics should grow rapidly over the next 25 years. An estimated demand for primary THAs will grow from 208,600 in 2005 to 570,000 by 2030, a 174% increase [4, 5]. Additionally, THA revisions should also increase substantially from 40,800 in 2005 to 96,700 by 2030, a 137% increase [4, 5]. This expected rise in the demand for THA revision will compound the economic burden that THA revisions have already imposed on Medicare. From 1997-2003, 19% of Medicare expenditures for hip replacements was apportioned to THA revision surgery [4, 5].

1.1.2 Risk Factors

Many long term studies have shown that a 90% success rate can be expected from a THA after ten years [3, 6, 7]; however, not all patients can expect to do this well. Aseptic loosening, joint instability, wear-related failure, painful hemiarthroplasty, and periprosthetic fractures all contribute to the need for revision

surgery after primary THA. Additionally, aseptic loosening is one of the most common causes at 30% of early (within the first five years) failures of the implant [8].

Other risk factors include infection, pulmonary embolism, stress shielding caused by the implant, and teratogenicity [9]. Additionally, hip replacements are becoming more common in younger patients (less than 60 years old) who are active; this increases the likelihood that the patient will outlive an implant. These risk factors and the expected growth in the need for revisions shows the need for continually improving hip implants.

1.2 Hip Implants

A variety of hip replacements are currently on the market. Aspects that vary from implant to implant include the geometrical stem design, fixation technique used to secure the stem, the surface coating, the material of which the stem is made, and the bearing surfaces used between the head of the implant and the acetabular cup. These all contribute to the survival rate of the femoral component and must be considered simultaneously when choosing which implant should be placed in a particular patient.

1.2.1 Cemented Stems

Cemented femoral components use polymethylmethacrylate (PMMA) to secure the femoral stem and provide initial and long term stability for the implant. Cemented femoral components were the first available stems on the market, and

cementing was the preferred technique for many years. The design of the hip stems and the surgical techniques have seen many advances since the initial THA dating back to Charnley's designs [10]. Stiffer materials like cobalt-chrome with high fatigue strengths now prevent stems from breaking. Components' edges are smoother to reduce stresses in bone cement, and many femoral stems today are also tapered to transmit the load through the PMMA in compression, which is the situation where the bone cement is strongest [2].

1.2.2 Press Fit (Uncemented) Stems

Press fit stems components are wedge shaped, a design that provides initial stability within the femur. Press fit stems get their long term stability from bone ingrowth which occurs in and on the surface of these stems over time. Proximal coatings were first introduced and used in the early 1970's. These first generation press fit stems had many problems, ranging from implantation technique to actual geometrical design. The main causes of failure in these early designs were an under sized stem , inadequate coating, non-circumferential coating, and an inadequate acetabular design [11]. Many of these design features and surgical techniques have improved over the past few decades; however, techniques and designs are still not perfect.

In press fit stems, aseptic loosening is currently a serious problem, one of the major causes of failures in THA, especially with active patients and patients younger than 60 years old [2]. In one study, aseptic loosening was the cause of approximately

30% of all the failures [12]. Aseptic stem loosening may be due to the design of the proximal part of the prosthesis. Rotational stability of an implant decreases in prosthetics with smaller radii because of the larger pressures, due to less surface area, produced at the bone-implant interface [13]. Additional research shows that using a collar decreases axial subsidence and that curved stems have significantly less motion at the bone-implant interface than straight stems [14].

The overall size of a stem also affects how the body interacts with it. Typically, titanium and cobalt-chrome are used in manufacturing femoral stems, and they have a much higher modulus of elasticity than cortical bone. This causes stress shielding to occur (the bone around the implant is reabsorbed because of decreased stress levels). Improving the geometrical design of the implant to reduce the cross-sectional area and moments of inertia can partly solve this problem. However, materials with increased fatigue resistance and lower modulus of elasticity are still needed to better mimic cortical bone.

1.2.3 Geometrical Stem Design

Stem design has an enormous impact on the performance of a hip implant. A few attributes of the femoral stem design that affect its performance are the use of a collar, the amount of curvature of the distal stem, the width of the stem in the medio-lateral and anterior-posterior directions, and the use of a taper. All of these features affect the performance of the hip replacement differently and must be considered

simultaneously in the overall design of the femoral stem to ensure optimal performance.

1.2.4 Surface Coatings

Many types of coating are used on cementless hip stems. Surface coatings are applied to the stems in different ways and have various physical properties that make them unique. Since the 1980's, the focus has been to coat only the proximal portion of the stem with some type of surface coating because extensively coated stems appeared to cause proximal stress shielding when a distal pedestal formed around the stem. This pedestal transferred the loads through the distal end of the stem straight to the shaft of the femur instead of to the proximal portion of the femur and then through the shaft of the femur. Additionally, a stem with ingrowth only on the proximal portion is easier to remove if a revision is required later [11].

A few of these surface coatings include cobalt-chromium or titanium beads, hydroxyapatite, plasma sprayed titanium, titanium wire mesh (fiber mesh), and trabecular metal (TM) [15]. Each of these coating are applied to the substrate of the stem differently to create biocompatible surfaces that will elicit a positive biological response involving osteointegration. Examples of Co-Cr alloy, titanium wire mesh, plasma sprayed titanium, and hydroxyapatite coatings are shown in Figure A 1 in Appendix A.

Cobalt-chromium and titanium beads are typically applied to the surface of the femoral stem by sintering. These types of surfaces have pore sizes ranging from 80-250 μm with 35-40% porosity that has interconnectivity.

Hydroxyapatite (HA) is applied to a titanium surface with a process known as plasma spray. HA coating increases the rate at which the bonding strength between the bone and implant develops in animal tests; however, long term bonding strength with and without HA are similar [16].

Plasma sprayed titanium involves a heated titanium alloy powder sprayed onto the substrate surface creating a randomly roughened surface with a pore size distribution between 100 and 1,000 μm.

Fiber mesh is made from titanium and looks like many thin wires bonded to the surface of the stem; it produces a porous surface where bone ingrowth can occur. Some implants with this type of surface also have a HA coating applied to the wire mesh to further increase osteointegration.

TM is porous biomaterial made of tantalum with mechanical properties very similar to bone, which makes it well suited for bone and joint reconstruction. TM has excellent corrosion resistance and great biocompatibility due to TaO5 which is its natural passivating oxide layer. This material was originally developed for the aerospace industry and will continue to have a large impact in reconstructive surgery [17, 18].

1.3 Micromotion

Implant micromotion, the amount of movement that occurs at the bone-implant interface, is one of many factors that influence the success of an implant [19]. Micromotion is affected by, among other factors, post-operative loading and stem surface coating [16, 20-22]. High post-surgical loads may cause excessive shearing motions at the bone-implant interface leading to fibrous tissue ingrowth instead of boney ingrowth [19]. The fibrous tissue ingrowth can lead to increased pain for the patient, resulting in a need for THA revision [23]. The various surface coatings applied to press fit stem all have different coefficients of friction, which affect how much the femoral stem moves under physiological loads. To prevent aseptic loosening caused by excessive motion, several studies suggest interface micromotion should be limited to a range of 30 to 150 μm [19, 24].

1.4 History and Background of Hip Joint Simulators

To study hip joint replacements, wear testing machines and joint force simulators have been developed and used for several years. One goal of these machines is to replicate the physiological loading conditions and motion patterns produced by the human body. Each machine has a different mechanism and is accordingly designed to accomplish different objective(s). Human gait is complex and difficult to replicate. For example, a machine theoretically needs six degrees of freedom to fully replicate the physiological conditions of the hip joint. Many simulators are simplified and only provide a few degrees of freedom, possibly because designing a simulator that can articulate more complex movements does not

guarantee that the simulation will be more accurate. In fact, errors committed by each individual actuator may very well create a larger inaccuracy than a simplified system. Moreover, designing and producing an extremely complex simulator is not always economically feasible [25].

1.4.1 Wear Hip Simulators

Many wear testing joint simulators have been developed. Most of these machines are designed to test the wear of the acetabular cup by rotating the acetabular cup around the femoral head of the prosthesis while under a specified loading pattern. Examples of this type of machine are a ten-station, multi-axis hip joint simulator by Goldsmith and Dawson [26]; the Leeds hip joint simulator [27], a three axial, single-station hip joint simulator by Saikko, shown in Figure A 2 in Appendix A [28]; a 12-station anatomic hip joint simulator by Saikko [29]; a hip wear simulator with 100 test stations by Saikko [30]; a 12-station hip simulator by Bragdon [31]; MATCO hip simulator [32]; an eight station hip simulator by Mejia, pictured in Figure A 3 and Figure A 4 in Appendix A [33]; and the Rocky Mountain Joint Simulator by Green [34].

Many wear testing machines were developed to study the effects on the acetabular cup of polyethylene wear. Polyethylene debris is associated with adverse tissue reactions that can cause osteolysis around the implant leading to component loosening [26, 28, 31, 33, 35]. This type of testing thus addresses the long term stability of the hip implant for this type of failure.

1.4.2 Joint Force Simulators

Joint force simulators can be used to study the micromotion of an implant at the bone-implant interface while being loaded. For hip replacements, the bone-implant interface lies between the femoral stem and the proximal end of the femur. Researchers have used three main experimental set ups for this type of study. The first two simulate a one legged stand, one by potting the distal end of the femur, rigidly fixing it to a table, and then applying axial and torsional loads through the head of the femur. Sugiyama [36], Gortz [37], and Naidu [38] used this protocol. Figure A 5, Figure A 6, and Figure A 7 in Appendix A show the schematic of each experimental set up. The second experiment is set up by creating a hinge mechanism with the distal end of the femur and then applying axial and torsional loading through the head of the femur as in the first protocol. This is a slight improvement because it eliminates the moments around the medial to lateral axis by mimicking the mechanics that occur at the knee. Engh [39], Monti [19], and Kligman [40] used this protocol. Figure A 8,Figure A 9, and Figure A 10 in Appendix A show the experimental set ups for these three projects. The third of the three experimental set ups fixes the shaft of the femur to a table or another solid object and then applies a torsional load through the center of the femoral head so that the femur is twisted. Thus, a researcher can see the effects on the femoral stem of raising and lowing oneself in and out of a chair and going up and down stairs. However, this represents only a small portion of each of these activities. Hua [23] and Baleani [24] have both used a version of this technique

in their studies, and Figure A 11 and Figure A 12 show these experimental set ups in Appendix A. Additionally, Schneider designed and used another experimental set up that applied axial and torsional loads through the stem with the distal end of the femur potted; however, the pot was attached to an x-y table, so the fixture would not create moments around either of the transverse axes. Figure A 13 in Appendix A shows this set up [41].

1.5 Purpose

The DBSJFS was designed and built to measure the micromotion of an implanted prosthesis at the bone-implant interface while the prosthesis is loaded under three dimensional physiological conditions. The DBSJFS improves on the current experimental methodology of micromotion studies involving the hip joint. The DBSJFS allows researchers to better mimic what a hip prosthesis experiences in vivo. Previous hip joint force simulators used in micromotion studies have not simulated human hip joint loads physiologically; these earlier simulators typically load a static femur in one or two dimensions.

The DBSJFS may be used for full scale experiments in testing the initial stability of several different types of femoral stems used for hip replacements that are currently on the market. The knowledge gained from these studies may help improve the design of future press fit hip stems, leading to fewer THA revisions and, therefore reducing the enormous health care costs of THA revisions incurred by Medicare.

Chapter 2 MACHINE DESIGN

Chapter 2 MACHINE DESIGN

2.1 Design Objectives

Requirements for the DBSJFS included the following:

1) Integrated with an MTS 858 Mini Bionix machine so the linear actuator could be used for dynamic loading of specimens. To meet this requirement, the femur specimens were positioned inside a gimbal with one stationary axis, Y', and one nonstationary axis, X'. The femoral heads were positioned at the center of its rotation, and the applied load passed directly through the center of the femoral head on the hip stem.
2) Mimics physiological human hip joint loading conditions given that the linear actuator always moves along a fixed vertical axis. To accomplish this requirement, the DBSJFS functioned by correlating the rotations about the X' and Y' of the gimbal with the dynamic loading patterns applied through the femoral head to replicate the physiological loading conditions that occur during various daily activities.
3) Uses two SS.2A hydraulic rotary actuators to properly orient specimens in three dimensions; purchasing new actuators was not possible. To meet this requirement, two SS.2A hydraulic servo motors were attached to the gimbal to rotate the femur around the perpendicular axes.

Additionally, Figure 1 on the following page is an Autodesk rending of the DBSJFS that shows the orientation of the X', Y', and Z axes on the simulator.

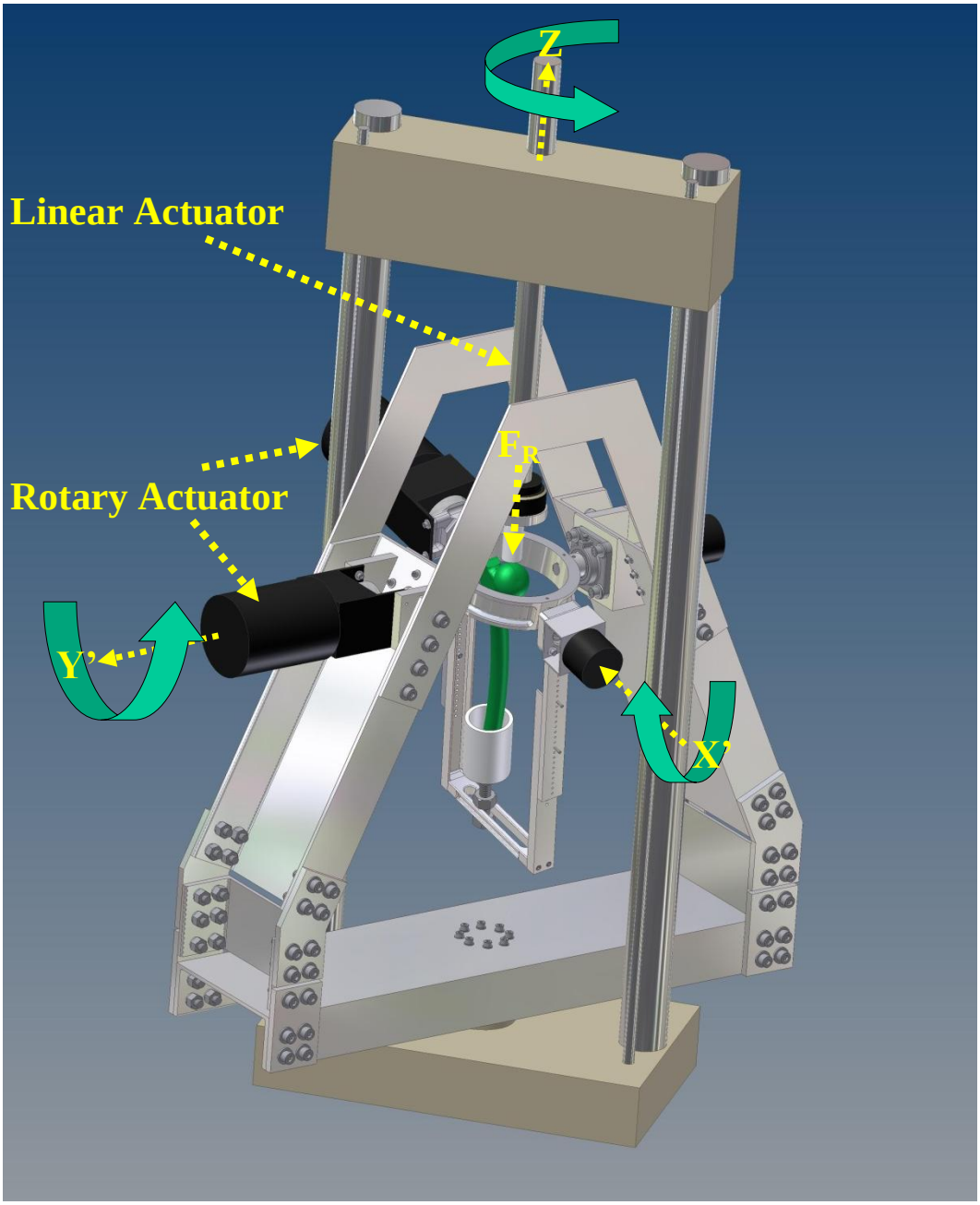

Figure 1. Autodesk rendering of the DBSJFS mounted inside the 858 Mini Bionix Machine; the X', Y', and Z axes are labeled, as is the resultant forces vector, F_R.

2.2 Description of the DBSJFS

Figure B 1 and Figure B 2 in Appendix B are digital photographs of the DBSJFS; showing it assembled and mounted within the 858 Mini Bionix for testing. The hip simulator has many unique features integrated into the frame and gimbal that help meet the design objectives.

The A-frame, made out of ten inch 6061 aluminum channel, provides adequate structural support to reduce global deflection under maximum loading conditions. The frame also provides the means by which every other part can be attached to the simulator. The base portion of the frame has a circular hole pattern, so the hip simulator can be mounted in the MTS machine without the rotary actuators or optical encoders interfering with the columns of the MTS (Appendix B; Figure B 3). The frame also extends vertically to provide space for the hydraulic rotary actuator and optical encoder, both attached along the X' axis of the gimbal to rotate through a larger range of motion.

The gimbal allows the distal end of a femur to rotate around two perpendicular axes while providing space for the linear actuator to apply loads directly to the femoral head. Key ways were used in conjunction with set screws to keep the shafts, which insert into the gimbal ring, locked in place after assembly (Appendix B; Figure B 4). Four windows were milled out of the gimbal ring to reduce its overall weight. The diameter of the ring was chosen to provide clearance for the greater trochanter on the proximal femur (Appendix B; Figure B 4).

The swing arms of the pendulum allow gross vertical adjustment to move the potted femur up and down for alignment. A slot in the horizontal member of the pendulum allows gross alignment adjustments along the X' axis (Appendix B; Figure B 5). Fine vertical and horizontal adjustments along the X' and Y' axes are made by manually moving the position of the base of the femur and securing it with thumb screws that insert through the sides of the potting cup (Appendix B; Figure B 6).

2.3 Structural Analysis

The frame of the fixture is made out of 10 inch aluminum channel bolted together into three different sections. This aluminum channel was chosen because aluminum is light weight, machines easily, and provides sufficient strength for our experiment.

The global deflection of the frame was calculated using the equations in Appendix C, section C.1. The global deflection of the frame itself will not affect the results obtained from the displacement of the femoral component between the bone and metal interface; however, the deflection must be minimized to prevent binding of the shafts during rotation. The total global deflection of the frame at point A (Figure C 1) with a 10 inch aluminum channel will be at most 0.0672 in. This deflection is small, so it does not affect the length of the femur used in the experiment because the constraints for medial to lateral adjustment and the pendulum motion needed to duplicate a person sitting down constrain the femur length to 13.5 in at most as measured from the distal cut to the center of the femoral head.

2.4 Input Loads and Profiles

The loading profiles used to control the DBSJFS were developed from data taken from *HIP98,* Bergmann's study at the Free University of Berlin in Germany [42]. This study provided in vivo dynamic hip joint loads during various activities for which the hip simulator would be programmed. The raw data from HIP98 included dynamic hip joint loading patterns for the activities of walking normally, going up stairs, going down stairs, standing up, and sitting down. In addition to being used to develop loading profiles, this data was also used to graph the corresponding motion envelope of the pendulum attached to the gimbal. The motion envelope of each activity was graphed because of potential interference problems between the simulator and the MTS machine, such as the pendulum hitting the columns of the MTS machine. The in vivo hip joint loading patterns and derived motion envelopes for the activities of walking normally (

Figure D 1 through Figure D 3), going up stairs (Figure D 4 through Figure D 6), going down stairs (Figure D 7 through Figure D 9), standing up (Figure D 10 through

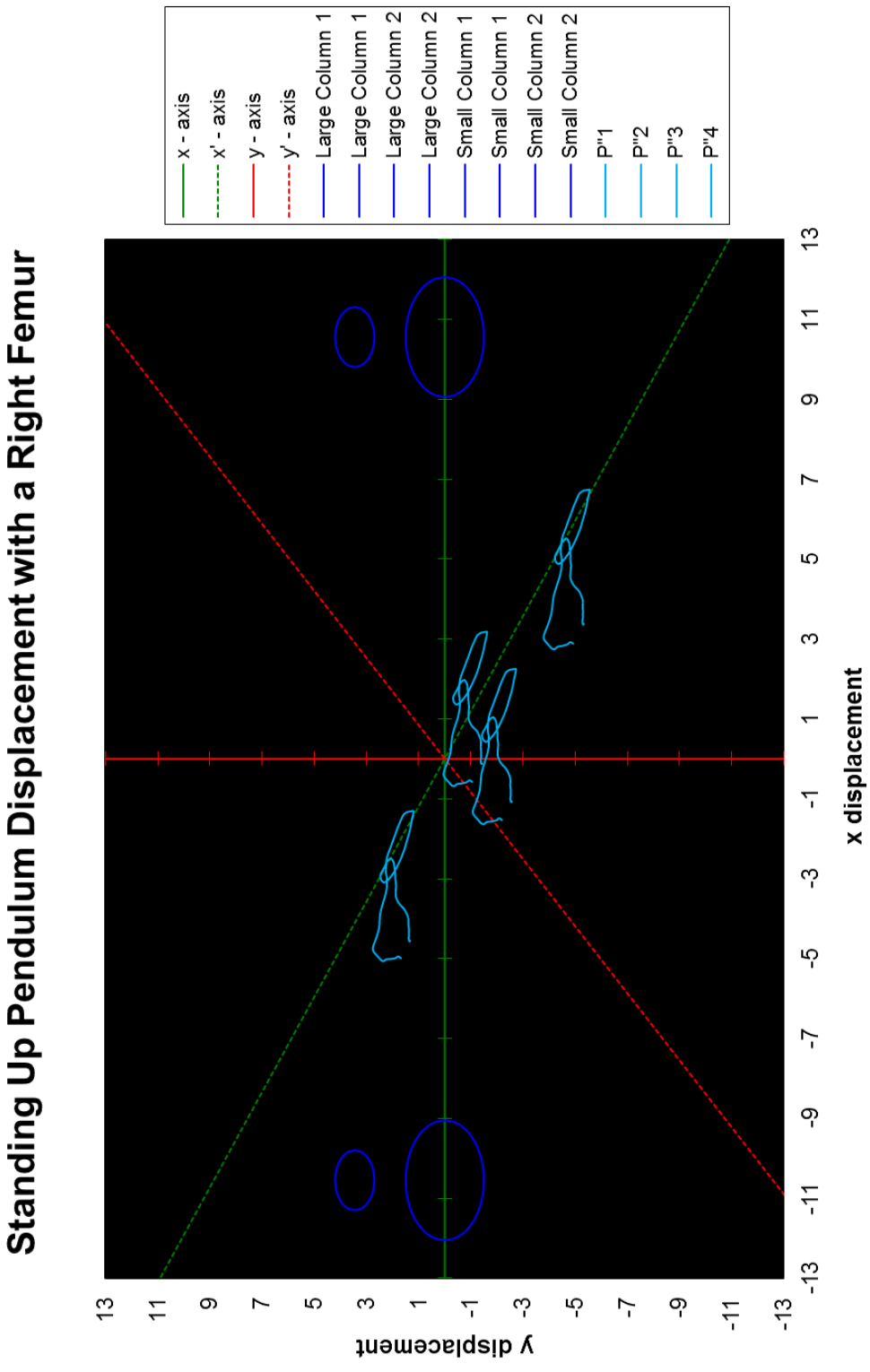

Figure D 12), and sitting down (

Figure D 13 through

Figure D 15) are listed in Appendix D. The three figures for each activity above include a graph of the in vivo average hip contact forces, the pendulum motion envelope for the left femur, and the pendulum motion envelope for the right femur. In the average hip contact force figures, the hip joint forces were plotted as a percentage of body weight against time. The forces graphed are resultant force (blue-green), force in the X direction (black), force in the Y direction (pink), and force in the Z direction (yellow). These X, Y, and Z axes correspond to the local coordinate system for the head of the femur used by Bergmann in HIP98. The figures of the pendulum motion envelopes depict a top down view of the DBSJFS. The dark blue circles define the columns of the MTS machine and each light blue shape details the path of one point on the pendulum. The positions of these points are shown in Figure C 6 and Figure C 7 in Appendix C. The solid red line indicates the Y axis of the MTS machine, the solid green line indicates the X axis of the MTS machine, the dashed red line is the Y' axis of the gimbal, and the dashed green line is the X' axis of the gimbal.

2.4.1 Mathematical Development

To develop the initial loading profiles, rotation matrices were used to derive the equations that give the desired rotations about the X' and Y' axes with the following known conditions. Please refer to Figure B 1, Figure B 2, and Figure B 4 for the location of these axes within the gimbal system.

1. The actuator can only push in the negative direction along the Z axis (Figure B 1).

2. Right femurs are placed in the simulator so the +X axis of the femoral head (lateral to medial) is aligned with the +Y axis of the MTS machine, the +Y axis of the femoral head (posterior to anterior) aligned with the +X axis of the MTS machine, and the +Z axis of the femoral head (inferior to superior) aligned with the +Z axis of the MTS machine (Figure B 1 through Figure B 3).
3. Left femurs are placed in the simulator so the +X axis of the femoral head (lateral to medial) is aligned the –Y axis of the MTS, the +Y axes of the femoral head (posterior to anterior) aligned with the +X axes of the MTS machine, and the +Z axis of the femoral head aligned with the +Z axis of the MTS machine (Figure B 1 through Figure B 3).

The derivation of the equations that give the rotations around the X’ and Y’ axes is in Appendix C, section C.4.

The axes around which the gimbal rotates are not aligned with the coordinate system of the MTS machine. Therefore, to graph the motion envelope of the pendulum, the displacement values calculated in relationship to the X’ and Y’ axes had to be transformed using another rotational matrix to graph the path the pendulum would take through the various gait patterns with respect to the MTS coordinate system. The derivations of these equations are given in Appendix C, section C.5.

2.5 Controls

The motion of the DBSJFS is produced by two hydraulic servo motors in displacement control. Optical encoders are secured to the opposite end of each shaft to which both motors are attached to give the computer feedback about the position of the each shaft. The software for the MTS mini Bionix machine has built in tuning parameters that include a proportional-integral-derivative (PID) controller, feed forward and feed backward input, and a forward loop (FL) filter, which are used to control the hydraulics of the servo motors.

The linear actuator attached to the frame of the MTS machine (Figure B 1) is also run with the same tuning parameters; however, it was under force control during the gait cycle and then displacement control at the beginning and end of each test.

A PID controller is a control loop feedback mechanism designed to correct the error between a measured process variable and a preferred setpoint. For example, with the DBSJFS, the PID software reduces the error between the actual rotational positions of each shaft versus the desired rotations for which each were programmed. A generic PID controller uses three basic components in its algorithm to correct this error. The proportional gain, P, changes the output proportional to the current error value. The larger the P value the more change will occur for a given increase in error and vice versa. However, the proportional gain alone will not allow the system to reach its target value, and if it is set too high, it can cause the system to become unstable. With P gain only, at best, the system will remain continually in a steady state error because as the error is reduced so is the proportional output. The second

component integral gain, I, helps correct the error in the system by calculating the integral term of the area under the error curve over time. This accelerates the process towards its desired setpoint, which eliminates the steady state error produced with P gain only. However, the I gain can cause the process to overshoot the setpoint because it works by responding to the buildup of past errors. This overshoot is controlled by the derivative, D, gain setting. D gain calculates the rate of change of the process error. For the DBSJFS, D determines how fast the hydraulic rotary motors spin the pendulum around the X' and Y' axes. D gain reduces ringing effects but can cause the system to become unstable if it is set too high.

Feed forward control is a mechanism by which a system can adjust the input signal to compensate for a known external disturbance. For example, feed forward input can be used to reduce continuous lag in the system by sending an input signal early. To improve control even more, input signals can also be adjusted with a feed backward control. The feed backward control changes the input signals based on the output obtained. The DBSJFS uses both feed forward and feed backward to alter the input rotational angles of the hydraulic rotary actuators. This allowed signal adjustment based on the dynamic loading patterns the motors experienced which reduced lag in the system.

A FL filter adjustment compensates for noise in a feedback signal. The noise typically originates from sensor feedback. For the DBSJFS control system, noisy sensor feedback was not a problem, and this parameter was not altered from the preset values.

Chapter 3 Materials and Methods

Chapter 3 Materials and Methods

3.1 Introduction

HIP98 was the first study to synchronously measure the forces in the hip joint with ground reaction forces and movement [42]. It, thus, served as the foundation for the loading profiles developed to test hip stems in the DBSJFS. The X, Y, and Z forces that Bergmann collected in his study were used to calculate resultant forces and the corresponding rotation angles that would allow the simulator to run each gait cycle with three dimensional constraints.

Dynamic loading patterns that mimic the joint force produced in walking normally, going up and down stairs, sitting down, and standing up were all mathematically developed. Each loading profile consists of three parts: 1) the resultant load applied vertically through the femoral head, 2) the X'-axis rotation, and 3) the Y'-axis rotation.

3.2 Preparation of Femur

An analog model was used in the DBSJFS to obtain the approximate PID and control settings needed to safely run the machine. The analog model used in validating the DBSJFS was a 3rd generation saw bone that had a cemented femoral stem placed within it. The saw bone was cut to a length of approximately 9.5 inches as measured along the axis of the diaphysis from a point that is perpendicular to the

femoral head to a distal point on the shaft of the bone. To place the cemented femoral stem, the steps listed below were followed.

1. Remove the femoral head with a transverse cut through the femoral neck.
2. Make two subsequent cuts on the proximal femur to resect additional material of the femoral neck to provide room for placement of the stem.
3. Ream out the inner material representing the cancellous bone to the appropriate size so that the femoral stem can be placed within the diaphysis.
4. Mix the bone cement and place it on the femoral stem.
5. Insert the femoral stem into the saw bone.
6. Take radiograph images with a C arm to confirm proper placement of the stem.

Figure 2 on the following page shows the proximal end of the 3rd generation saw bone with the femoral stem inserted into it.

Figure 2. Image of the proximal end of a 3rd generation saw bone with a cemented femoral stem inserted.

3.3 Potting Process

After the stem was cemented in the saw bone, the distal end of the femur was potted in the aluminum cup fixed to the pendulum of the DBSJFS. To ensure proper alignment of the femur, the following steps were taken.

1. Attach the femoral head alignment jig to the universal ring.
2. Place the distal end of the femur in the aluminum cup attached to the bottom half of the pendulum.
3. Slide the bottom half of the pendulum and femur into place so that the femoral head is held within the alignment jig.
4. Insert bolts to fix the swing arms of the pendulum.

5. Using a level, rotate the pendulum so that the swing arms are vertical to both the Z-X and Z-Y planes.
6. Manipulate the femur so it is correctly oriented. Align the axes by visual inspection. Right femurs are placed in the simulator so that the X and Y axes of the femoral head are aligned with the Y and X axes of the MTS machine. Left femurs are placed in the simulator so the X and Y axes of the femoral head are aligned with the -Y and X axes of the MTS machine.
7. Tighten the thumb screws on the sides of the aluminum cup to hold the femur in the correct position.
8. Grease the inside of the aluminum cup and then mix and pour bone cement into it.
9. After the bone cement has dried, remove the femoral head alignment jig.

Figure 3 on the following page shows the femoral head in the alignment jig described in step 3, and Figure 4 on the following page shows the assembly of the pendulum and potted distal femur with the DBSJFS. The thumbs screws used to hold the femur in place during step 5 can be seen around the outside of the aluminum pot.

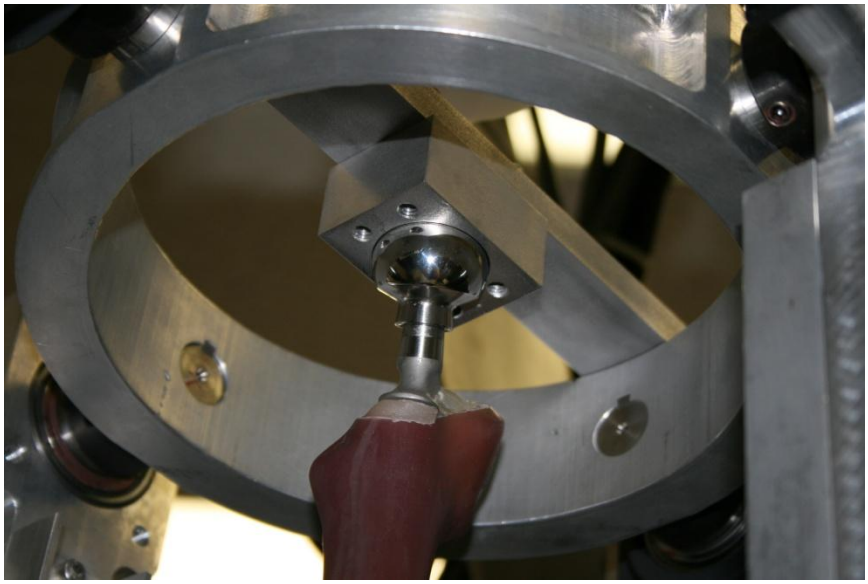

Figure 3. Image of the femoral head within the alignment jig.

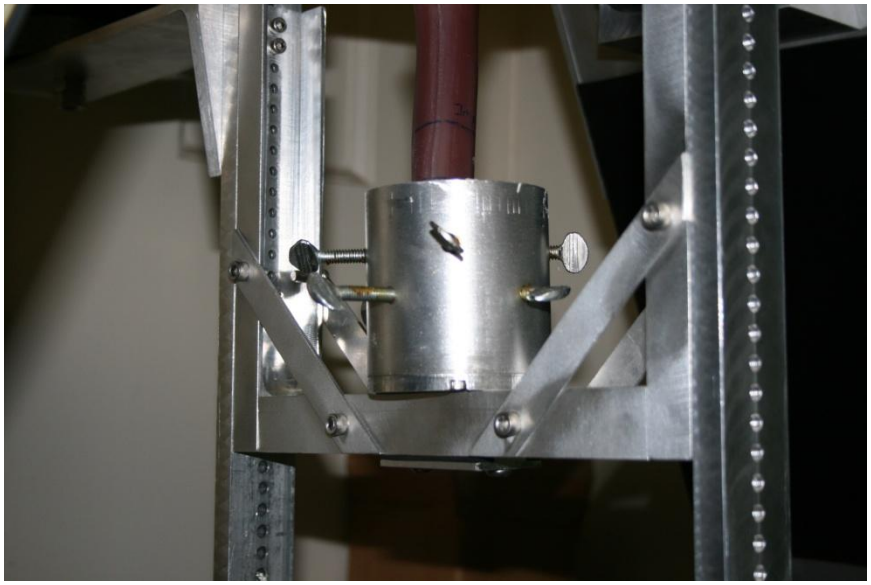

Figure 4. Image of the potted distal femur attached to the pendulum.

3.4 Loading Profile

Ten loading profiles were generated for the DBSJFS, five for the right hip and five for the left hip. The profiles produced for right and left hips were walking normally, going up stairs, going down stairs, standing up, and sitting down. As explained in Chapter 2, the X' and Y' rotations and the axial loading patterns for each gait cycle used data from HIP98. However, these gait cycles could not be used for testing without modification because they were misaligned. First, the data used was an average of the participants of the HIP98 study. Second, the swing phase of each gait was not recorded and included only the data from the time right before heel strike to just after toe off. Third, the average values for the sitting down cycle did not include the female participant although the average values for standing up did. This caused a discrepancy in magnitude and location of the hip forces at the beginning and end of these cycles because females have a different anatomical structure. These three factors necessitated slight adjustments to the beginning and end of each cycle to achieve a smooth transition, which is important for safely operating the DBSJFS. Smooth transitions allow the machine to have more fluid motion and better stability. The PID control can also be tuned more accurately leading to greater control of the machine.

After the input profiles were created, each was entered into a procedure made using the MTS software, which controlled the DBSJFS. Graphs of the input data for the left hip are provided in Figure 6, Figure 8, and Figure 10 on the following pages. Figure 5, Figure 7, and Figure 9 show the original data before modification. Original

and smoothed gait profiles for the right hip are provided in appendix D in Figure D 16 through Figure D 21. Three cycles of the each gait are shown in each of these figures, demonstrating the transition between the beginning and end of a cycle. Comparing the original profile and the smooth profile of any given gait illustrates the corrected gap between cycles. These gaps had to be reduced so the machine could run smoothly. The three cycles are differentiated by a solid line followed by a dashed line followed by another solid line.

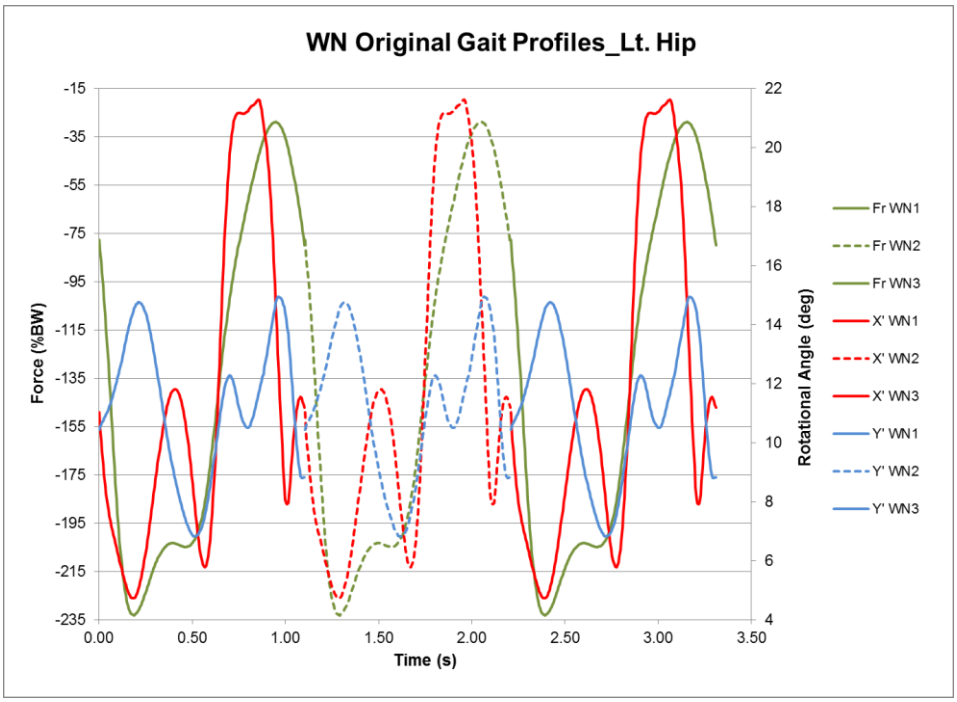

Figure 5. Walking normally original gait profile of the left hip.

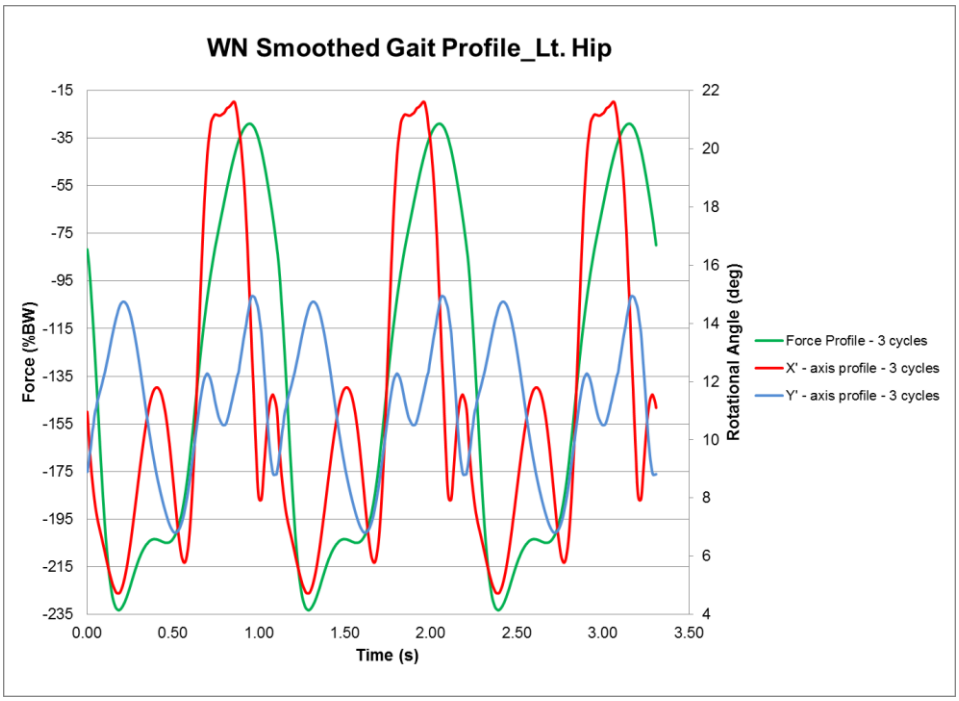

Figure 6. Walking normally smoothed gait profile of the left hip.

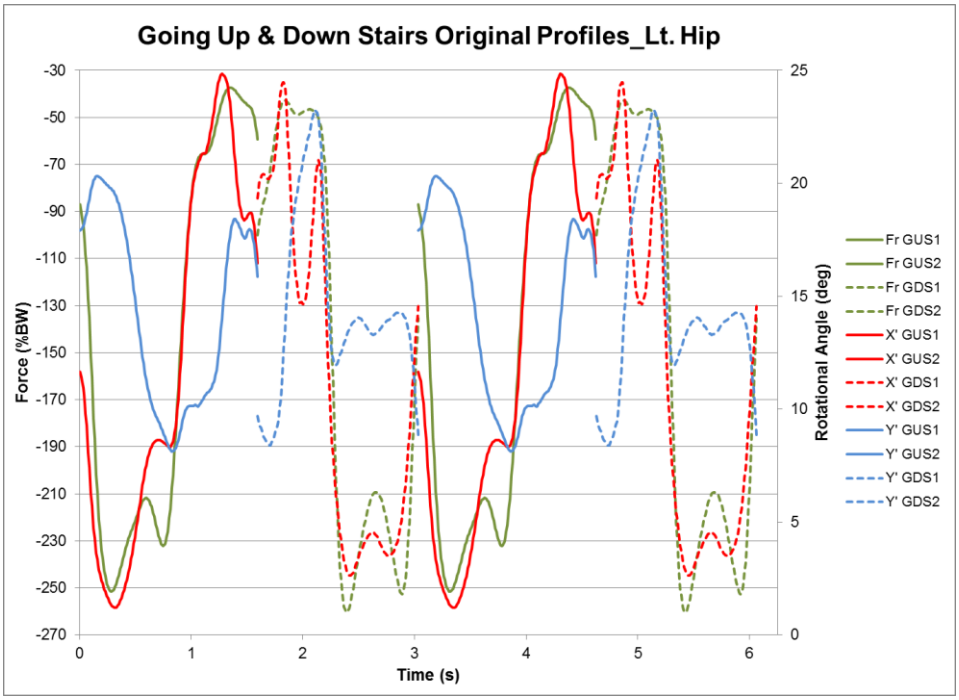

Figure 7. Going up and down stairs original profile of the left hip.

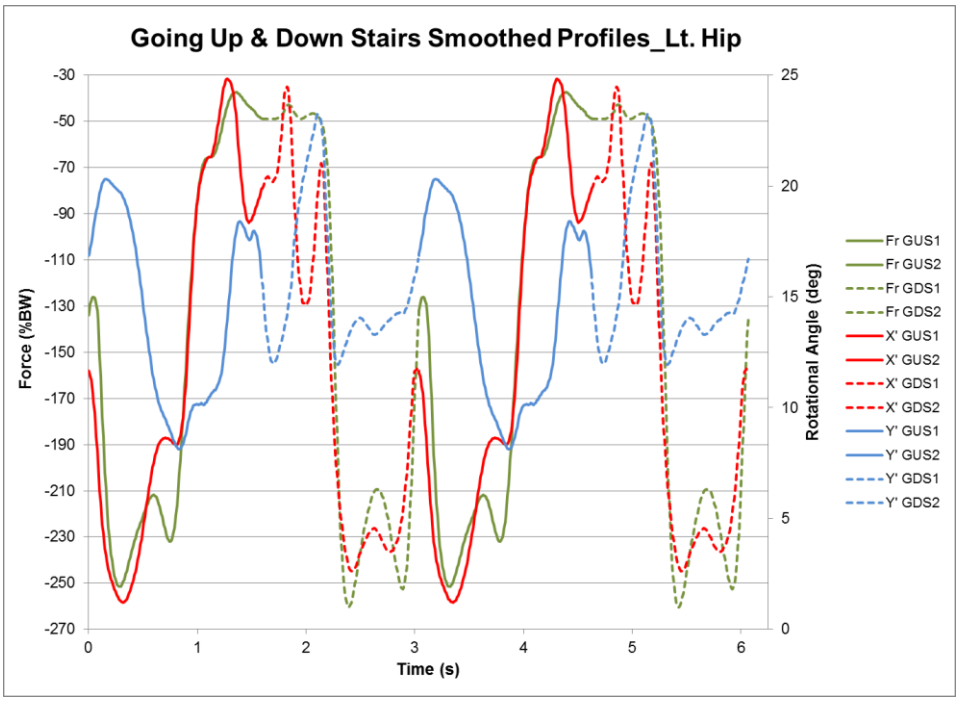

Figure 8. Going up and down stairs smoothed profile of the left hip.

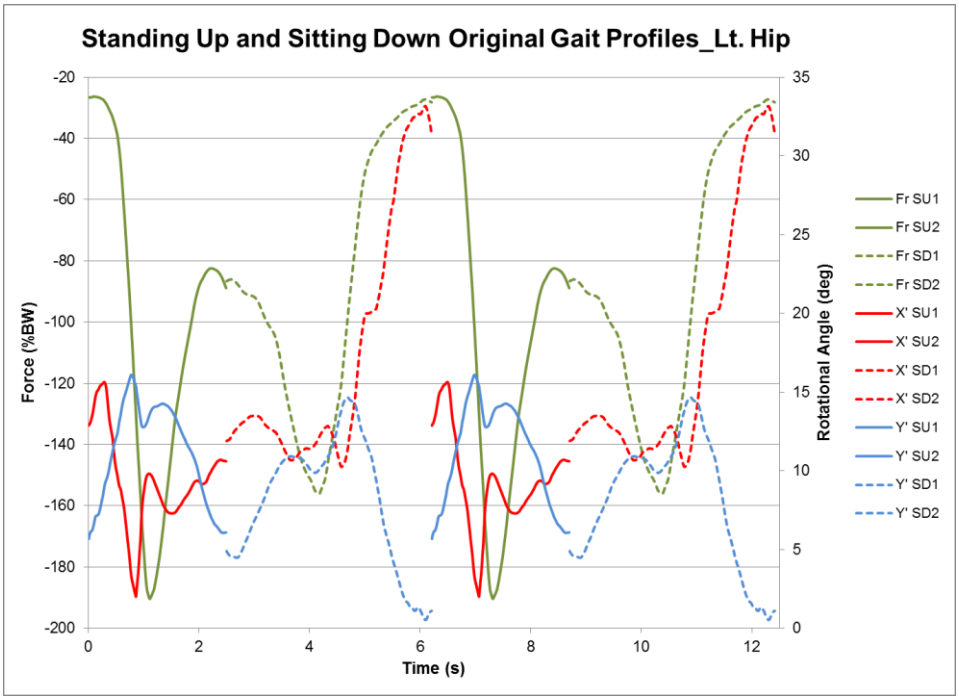

Figure 9. Standing up and sitting down original gait profiles for the left hip.

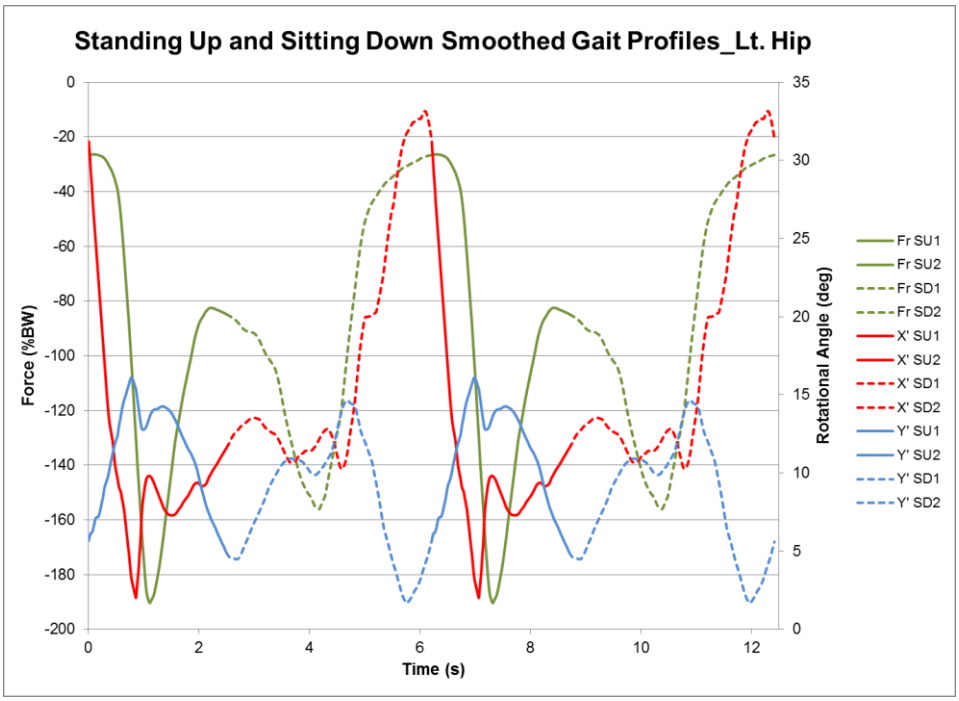

Figure 10. Standing up and sitting down smoothed gait profiles for the left hip.

3.5 Data Collected

To validate the DBSJFS, data was collected for the left femur only. However, future tests should be run with a right femur using these procedures. The gait patterns for WN, GU & DS, and SU & SD were run at frequencies equivalent to $1/10^{th}$, $1/5^{th}$, and $1/3^{rd}$ physiological speeds. At $1/10^{th}$ and $1/5^{th}$ physiological speeds, tests used body weights of 100 N, 175 N, 250 N, 325 N, 400 N, 500 N, 600 N, 700 N, 800 N, and 900 N. At $1/3^{rd}$ physiological speed, tests used body weights of 800 N and 900 N.

The data gathered during each test included the following: average axial force absolute error, maximum axial force absolute error, average upper angle absolute error, maximum upper angle absolute error, average lower angle absolute error, and maximum lower angle absolute error. Each gait was run for 100 cycles. Data was collected during cycles 20, 40, 60, 80, and 100. An average for each of these cycles was calculated to indirectly analyze the machine for repeatability, and an average of the five cycles was calculated and reported.

3.6 Tuning Parameters

To tune each of the channels for the DBSJFS, a guess, test, and revise method was used first for each individual channel and then with multiple channels running at the same time. Individually, the hydraulic rotary actuators were tuned unloaded to a ramp function and a sine wave. The rotary actuators were then tuned together while running simultaneously with each following off-setting sine waves to create a circular

pattern. The linear actuator was then tuned without the rotary actuators in motion for both displacement control and force control.

Next, all the channels were tuned, with having the rotary actuators turning the pendulum in a circle while the linear actuator applied a constant load through the femoral head. Once tuning parameter values were obtained that did not greatly affect the control of the DBSJFS as loads changed or circular motion varied, validation testing of the DBSJFS began, running the gait cycles created. Tuning parameters used during testing are reported in Chapter 4.

Chapter 4 CAPABILITIES AND PERFORMANCE

Chapter 4 CAPABILITIES AND PERFORMANCE

4.1 Results

For the procedure of walking normally the maximum and average error produced by the linear actuator were directly related to both the speed of the gait and the applied body load; the values increased together in a positively sloping linear trend line. Additionally, the average force error recorded for all tests run at a body weight of 600 N deviated downward from the trend line; however, the maximum force error did not deviate from the trend line for those same tests. This can be seen in **Error! Reference source not found.** and Figure 14.

The upper angle, Y' rotation, average error during tests on walking normally followed a flat linear trend for all speeds and loads between 200 and 900 N and depended only on speed. The body weight at which the DBSJFS was loaded did not affect the error produced in this channel. The average error for all recorded tests between 200 and 900 N was within a range of 0.6 to 0.75 degrees. The upper angle max error also increased with increasing speeds but also depended on the body weight load as error increased with increasing body weights. This can be

seen in

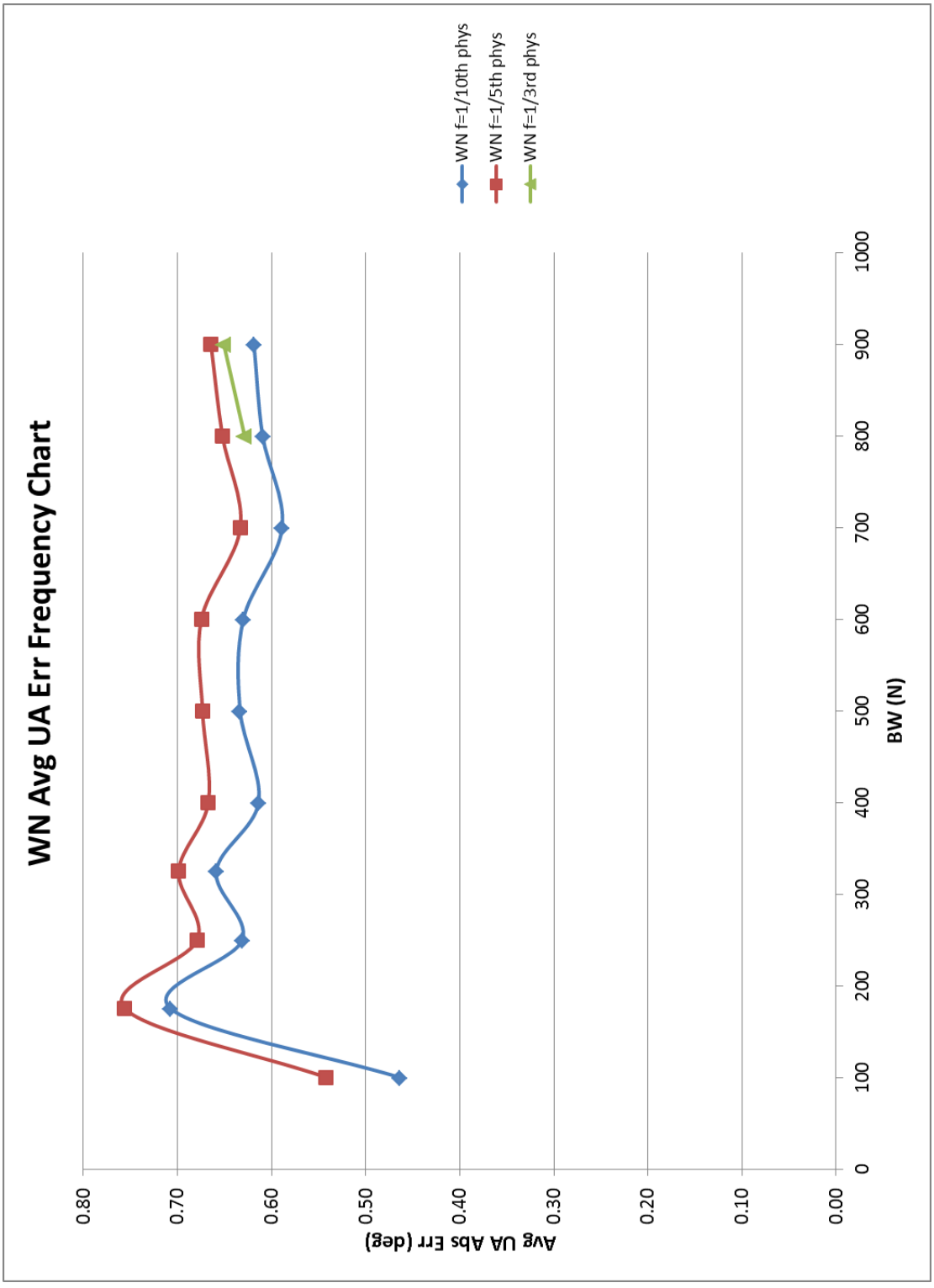
WN Avg UA Err Frequency Chart
WN f=1/10th phys
WN f=1/5th phys
WN f=1/3rd phys
Avg UA Abs Err (deg)
0.80
0.70
0.60
0.50
0.40
0.30
0.20
0.10
0.00
0
100
200
300
400
500
600
700
800
900
1000
BW (N)

Figure 12 and Figure 15.

The lower angle, X'axis rotation, average error for the tests on walking normally demonstrated behavior similar to the Y' axis rotation for loads up to 700 N. However, as the applied body weight load increased beyond 700 N, both the average and maximum lower angle errors increased greatly. This increase in error was a limiting factor in the performance of the DBSJFS (Figure 13 and Figure 16).

Except for tests with 600 N body loads, the repeatability for walking normally average and maximum error in all channels was acceptable; the data followed flat linear trend lines. For the tests run at 600 N at $1/10^{th}$ physiological speed, the repeatability for the maximum force absolute error and the upper angle absolute error was not as predictable as other tests. The maximum force absolute error varied from approximately 17 to 23 N of error where the repeatability at all other loads at the same frequency did not vary by more than 1.5 N. This data is shown in Figure 17 through Figure 22. Walking normally repeatability data for frequencies at $1/5^{th}$ and $1/3^{rd}$ physiological speed are shown in Figure F 13 through Figure F 24 in Appendix F.

Figure 23 through Figure 28 display the force/upper angle/lower angle command, output, and absolute error for each channel at the frequency and body weight loads specified. These figures show how the error changes in each channel throughout the entire cycle. The error tended to increase with increasing load throughout the cycle; however, the rate of change of the applied force was directly related to the error

generated in the channels. Additionally, the rate of change of the upper and lower angles was positively related to the error generated in those channels. The data shows that some of the largest error values occurred in the cycle when the rotatory and linear actuators changed position and force the fastest.

The test results for going up and down stairs and standing up and sitting down followed similar trends with slightly different ranges; they are shown in Figure F 1 through Figure F 12 in Appendix F. Exceptions include the following:

1. GU & DS average force error showed decreases in error at loads of 400 and 600 N (Figure F 1).
2. SU & SD average force error was extremely high for the tests that used loads of 400 N. The high average and maximum error appear to be load dependent; each occur at both $1/5^{th}$ and $1/10^{th}$ physiological speeds (Figure F 7 and Figure F 10).

Comparing the walking normally force error data to the command load values instead of using the data as absolute values demonstrated a low percentage error. The WN average force error was approximately 1% of the average commanded force over the entire cycle when the DBSJFS operated at $1/10^{th}$ physiological speed with loads equivalent to a 400 N individual. Moreover, at the instant during the cycle when the maximum error is reached, the WN maximum force error was approximately 1.2% of the commanded force.

The DBSJFS operated most effectively with the smallest acceptable error for all channels under loads representing a 700 N individual at a frequency of $1/5^{th}$ physiological speed.

At these parameters, the hydraulic rotary motors tended to produce approximately the same amount of average and maximal error as at lower loads. If the load and frequency increased, the

slope of the average and maximum lower angle error significantly increased (

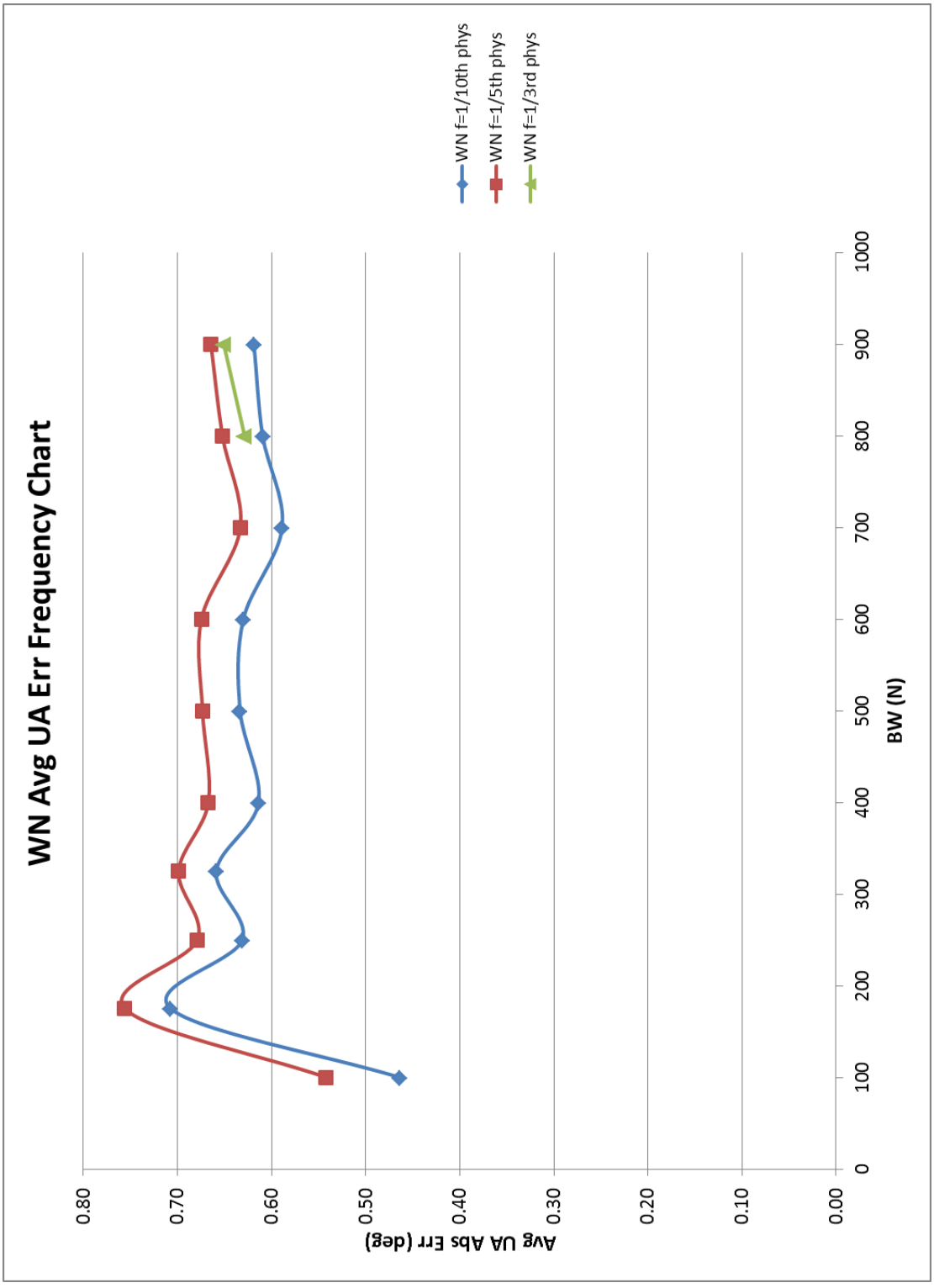

Figure 12 and Figure 15). The error charts of the linear actuator also became slightly steeper, with the frequency lines beginning to deviate away from each other. The DBSJFS can operate at loading cycles representing a 900 N individual at 1/3rd physiological speed. It was not tested at parameters higher than this.

4.2 Walking Normally Average Error Frequency Charts

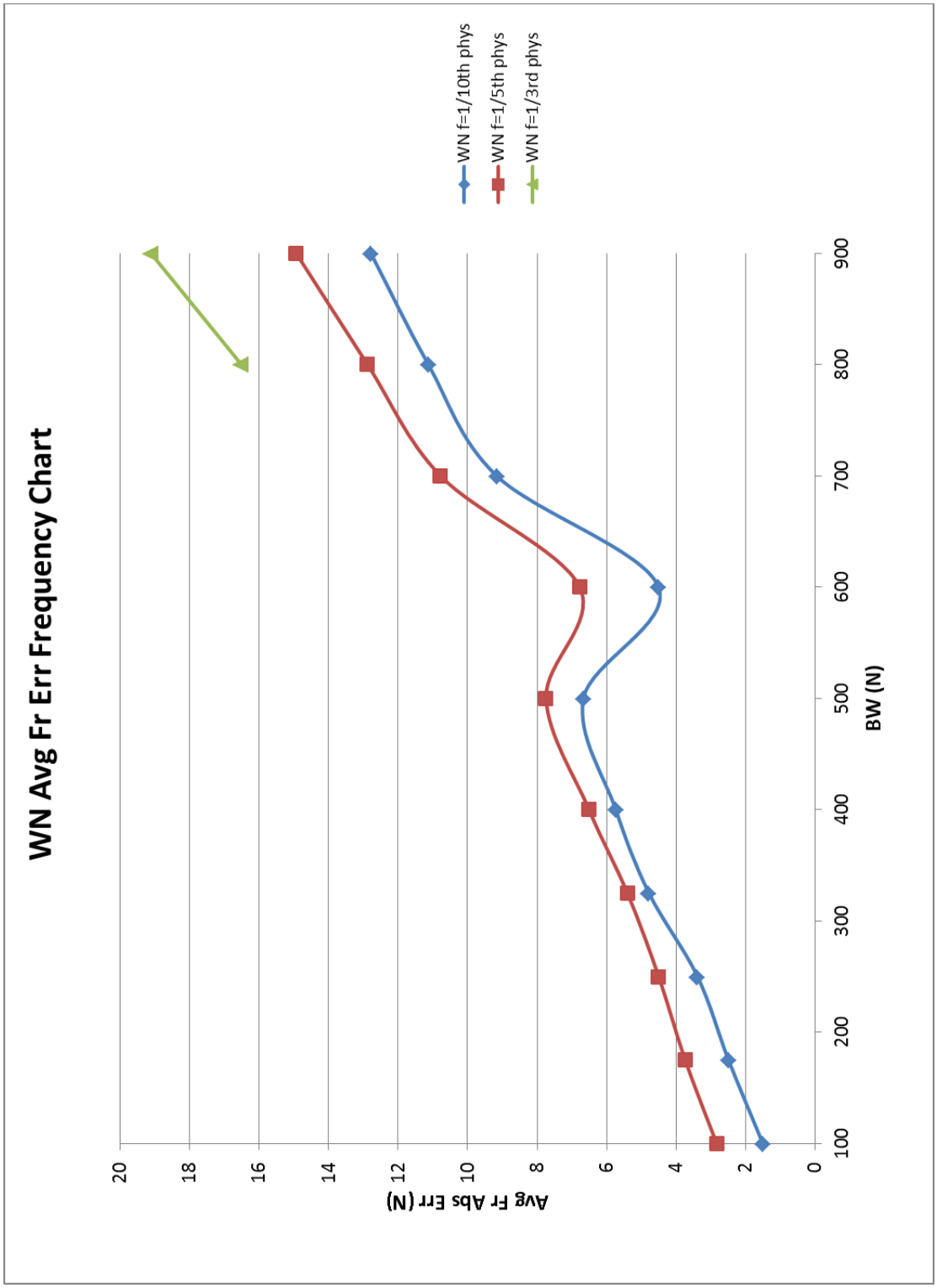

Figure 11. WN Avg F_R Err frequency chart.

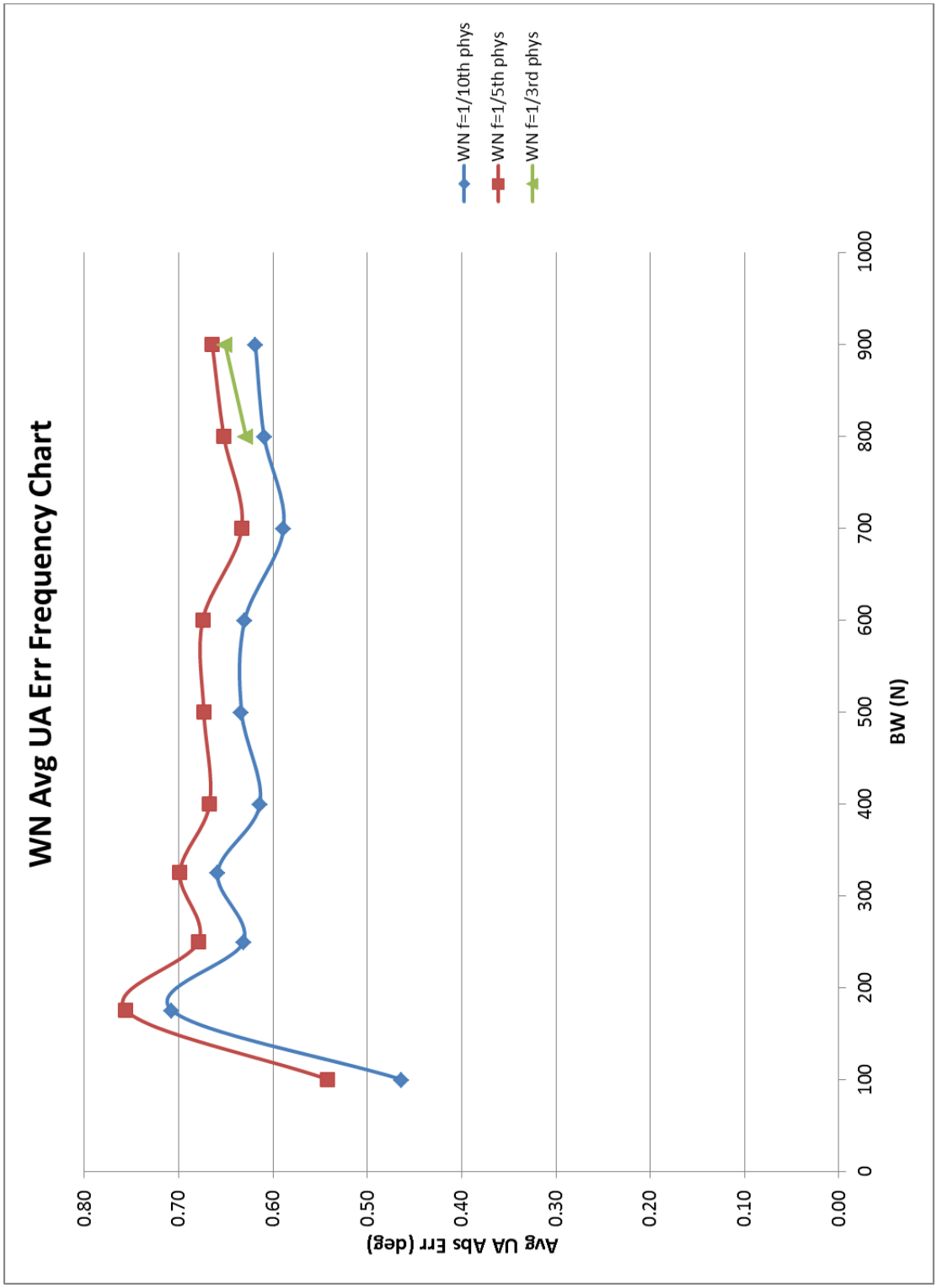

Figure 12. WN Avg UA Err frequency chart.

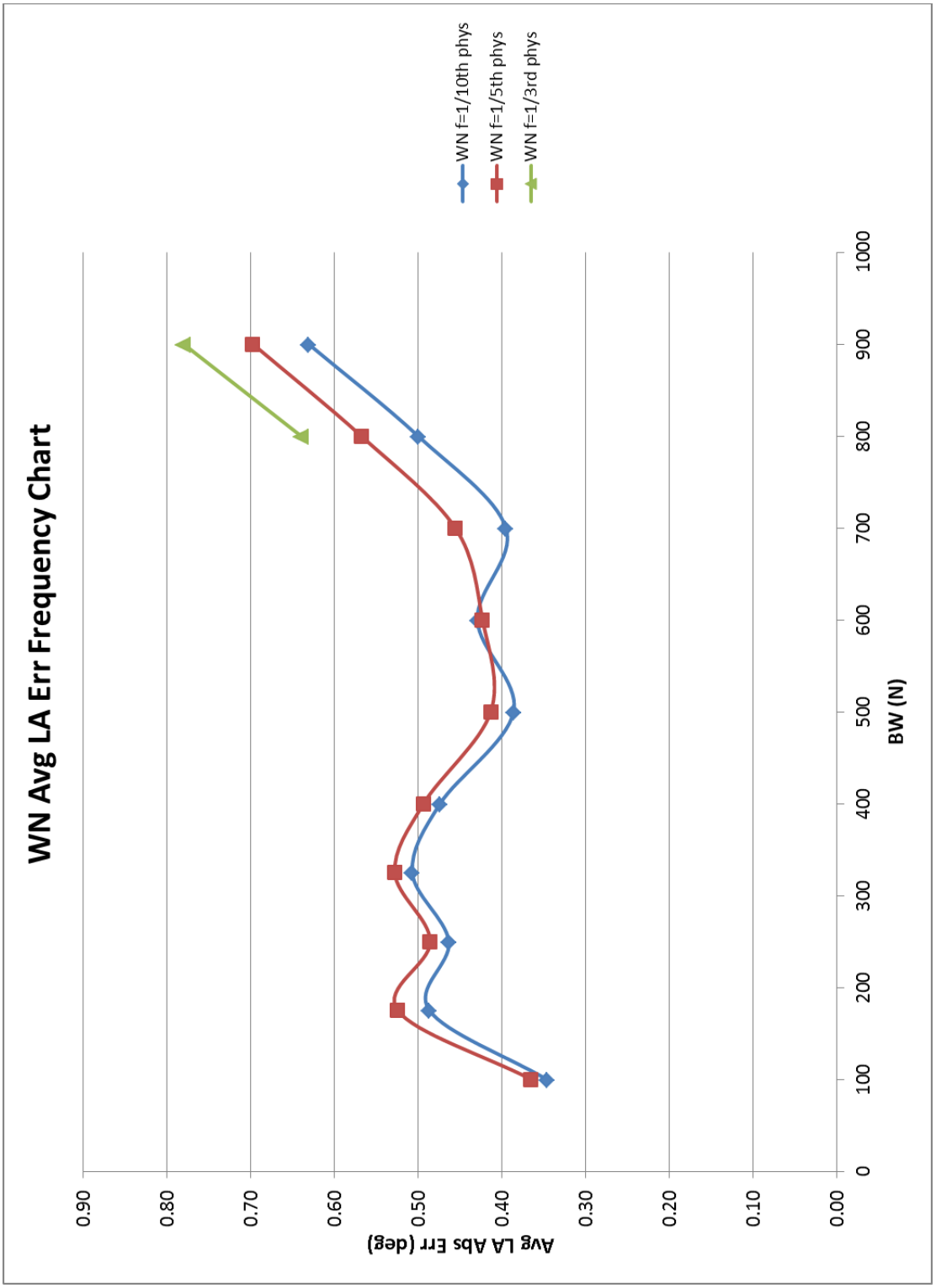

Figure 13. WN Avg LA Err frequency chart.

4.3 Walking Normally Maximum Error Frequency Charts

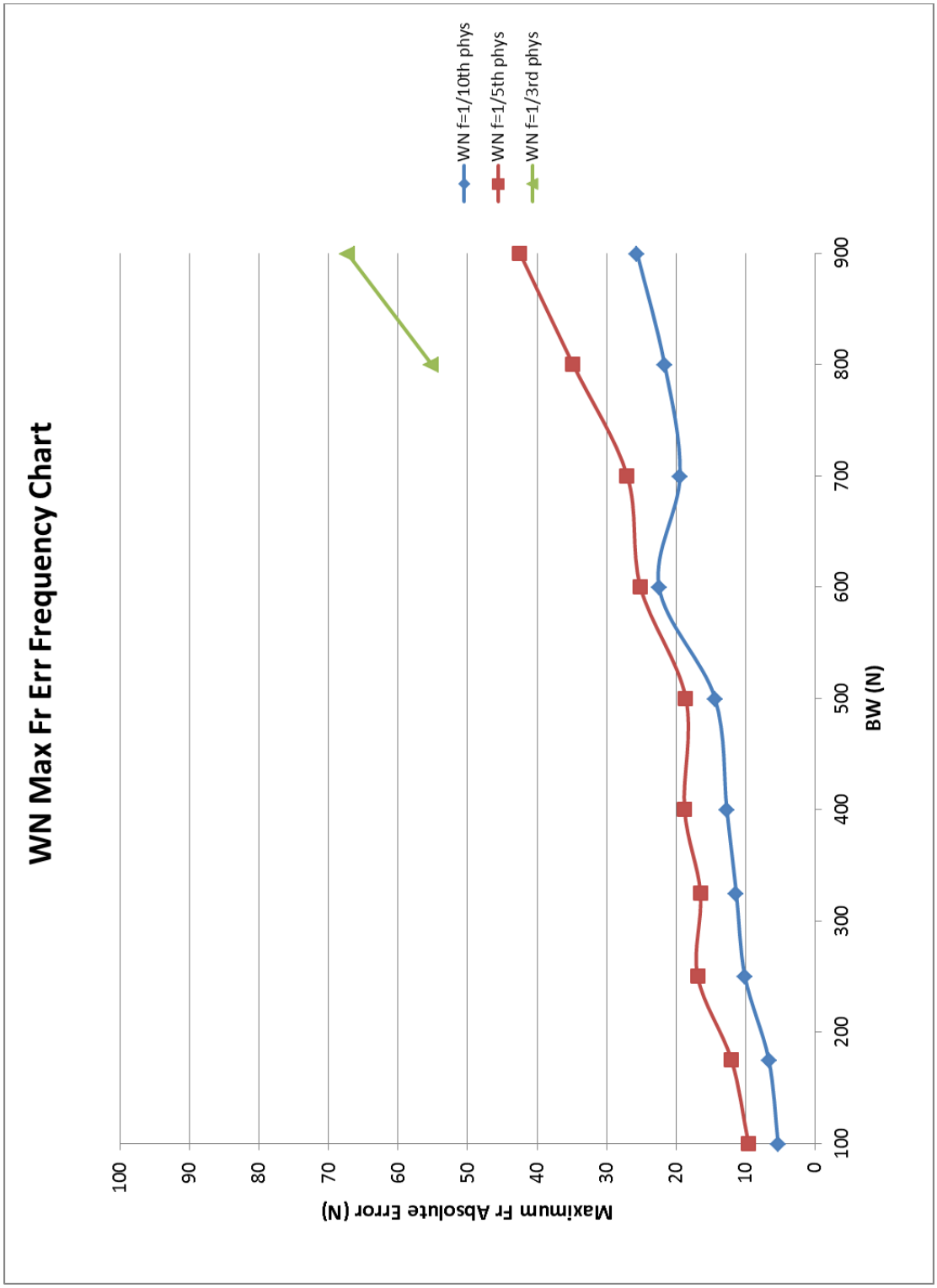

Figure 14. WN Max F_R frequency chart.

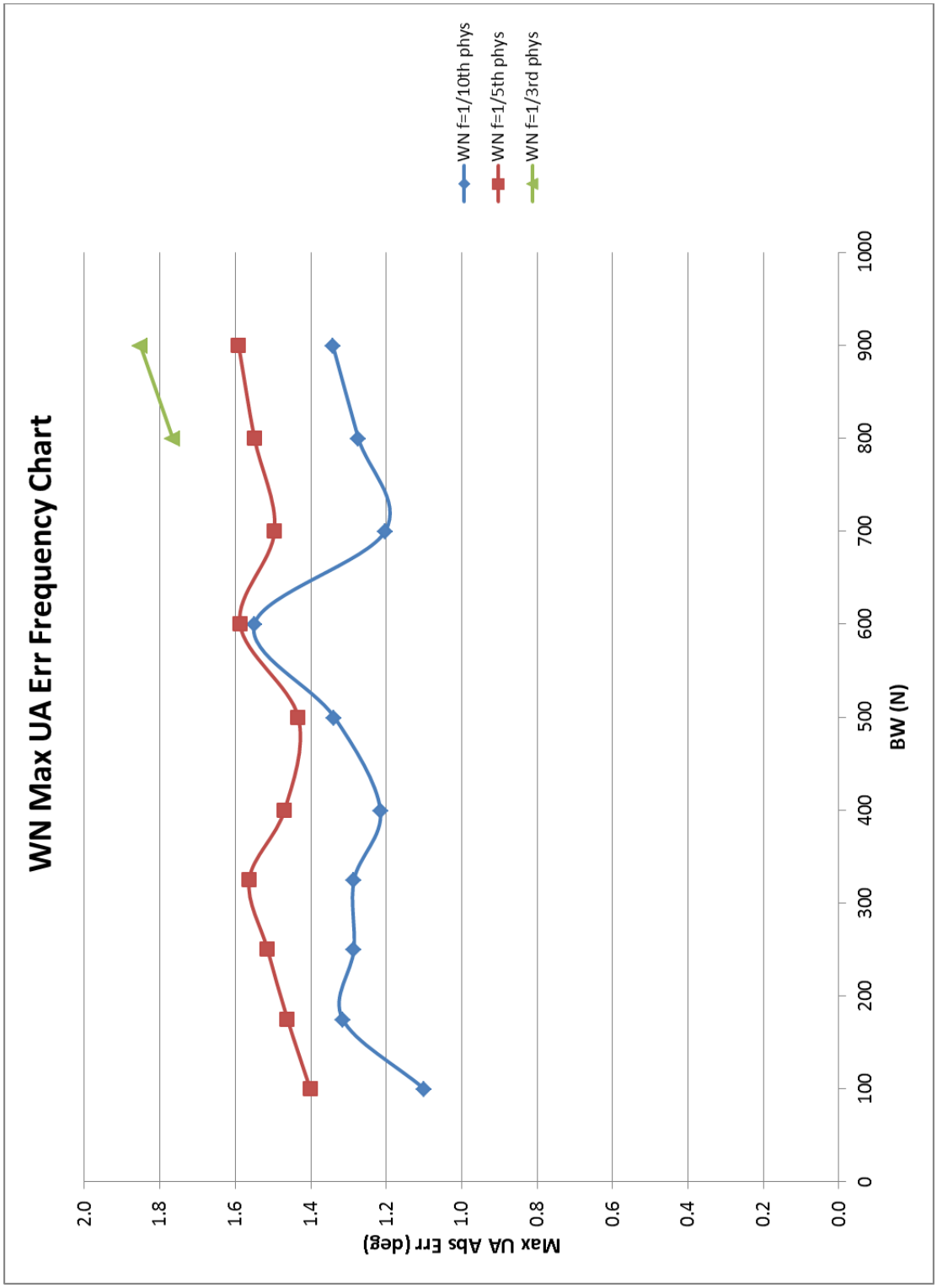

Figure 15. WN Max UA Err frequency chart.

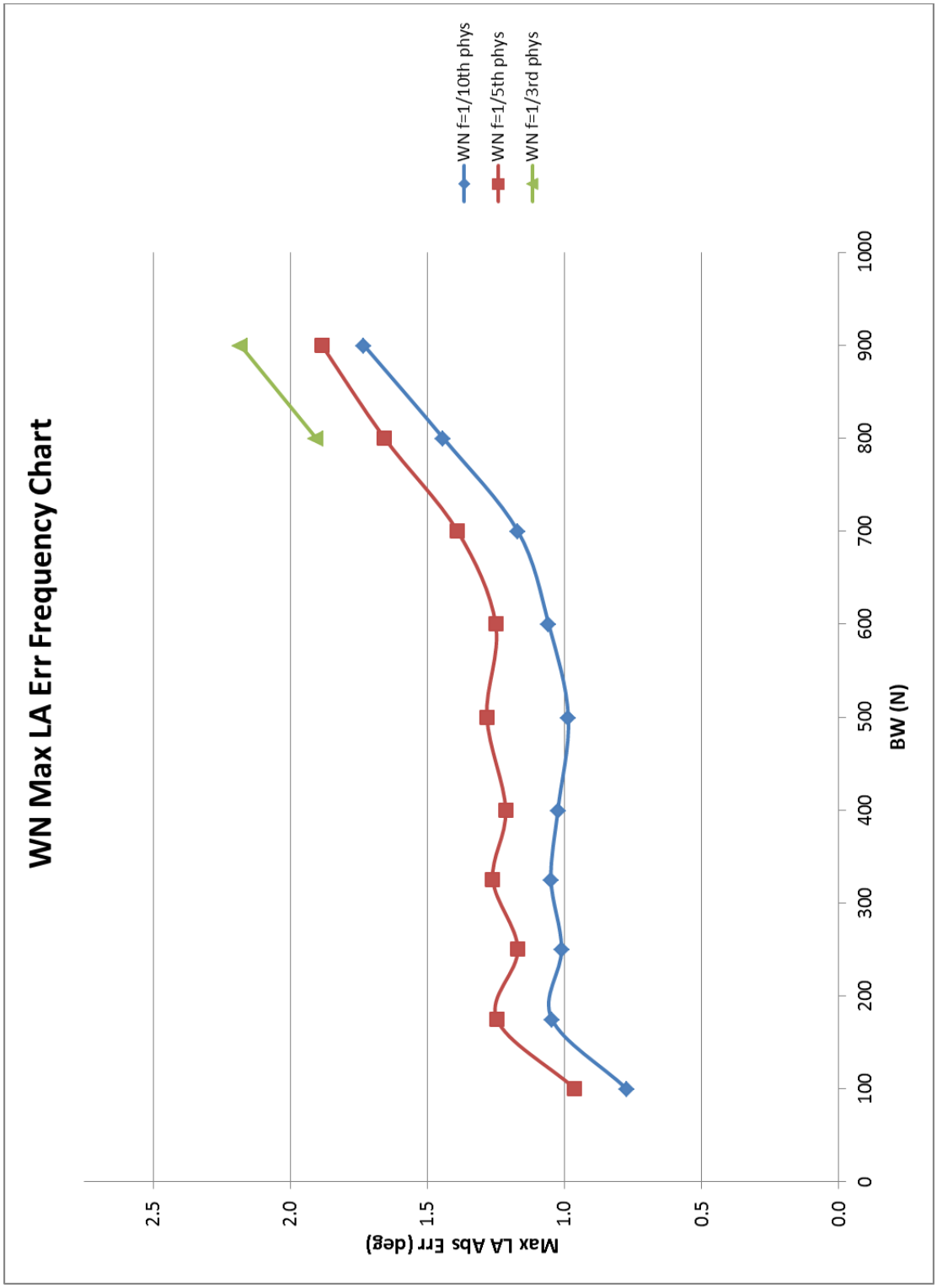

Figure 16. WN Max LA Err frequency chart.

4.4 Walking Normally Average Error Repeatability

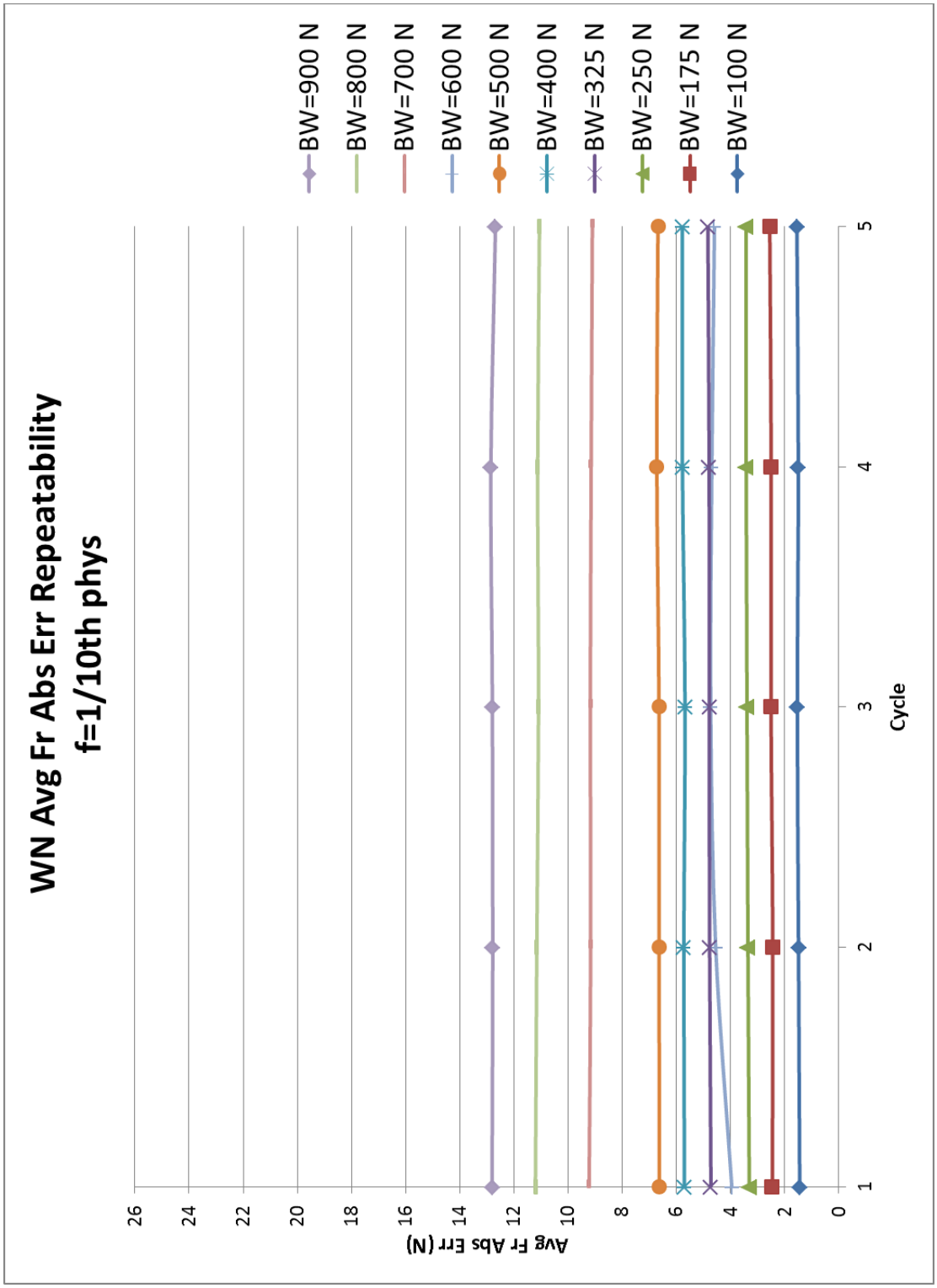

Figure 17. WN Avg F_R Abs Err repeatability at 1/10th Phys.

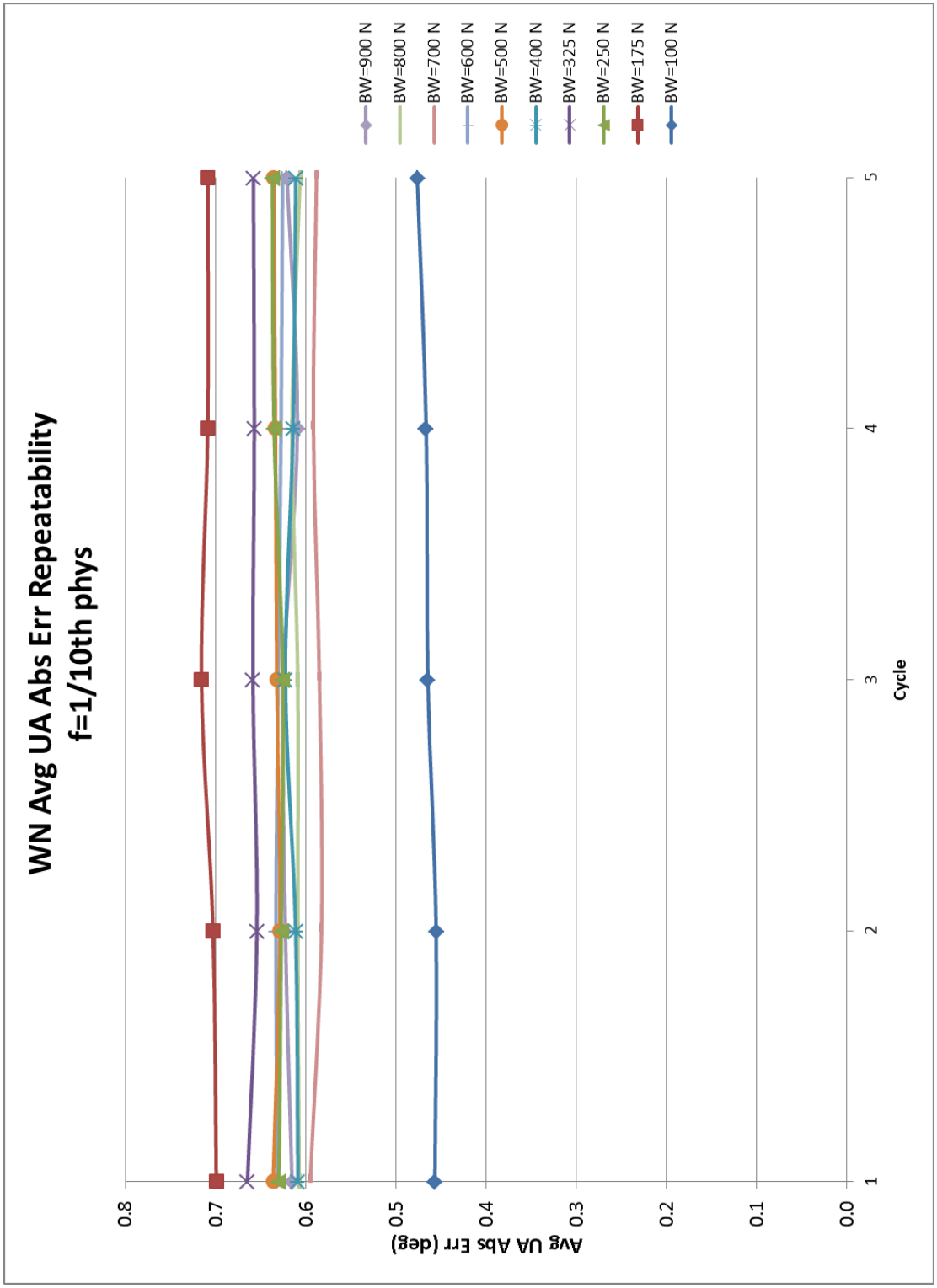

Figure 18. WN Avg UA Abs Err repeatability at 1/10th Phys.

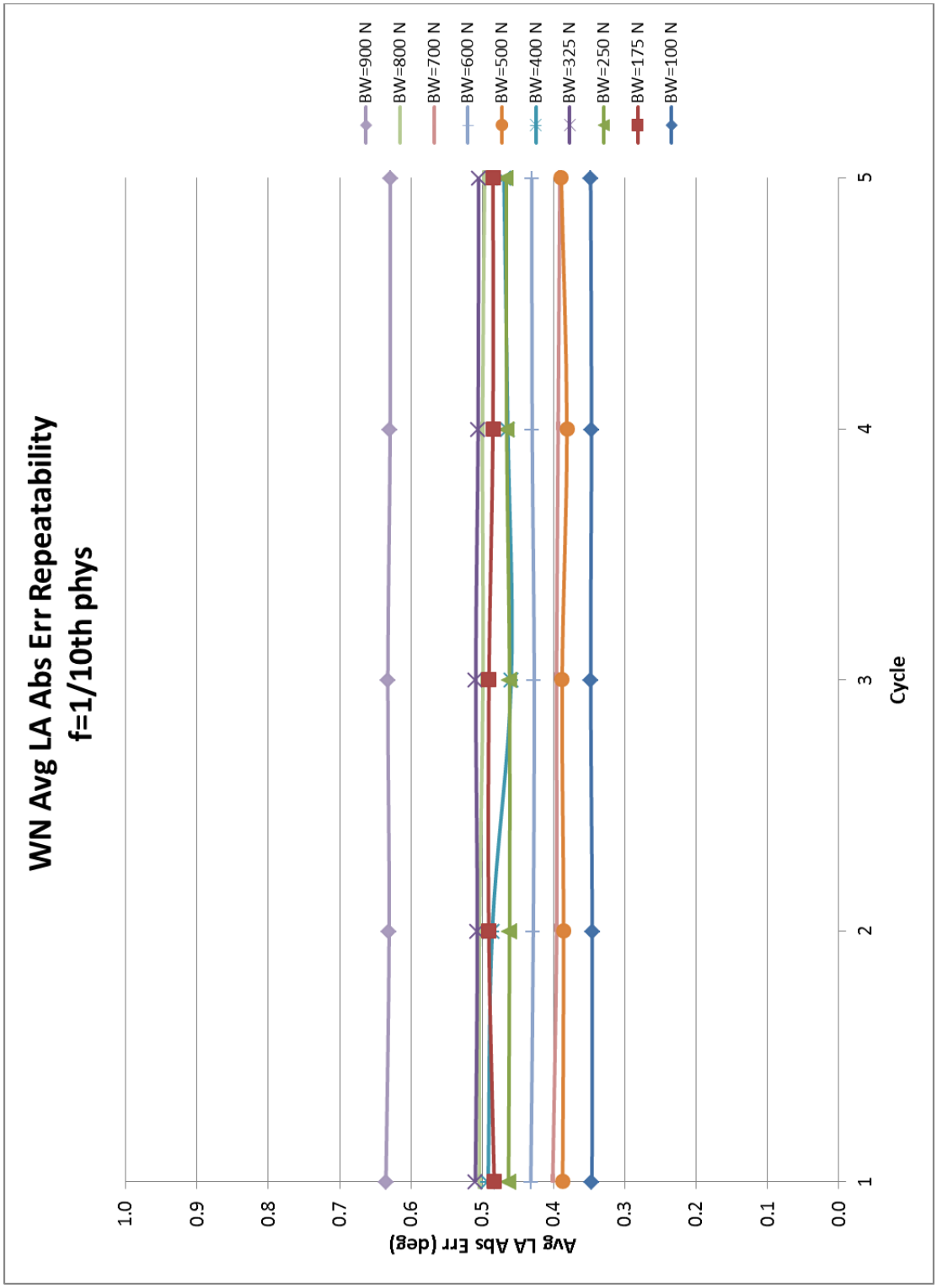

Figure 19. WN Avg LA Abs Err repeatability at 1/10th Phys.

4.5 Walking Normally Maximum Error Repeatability

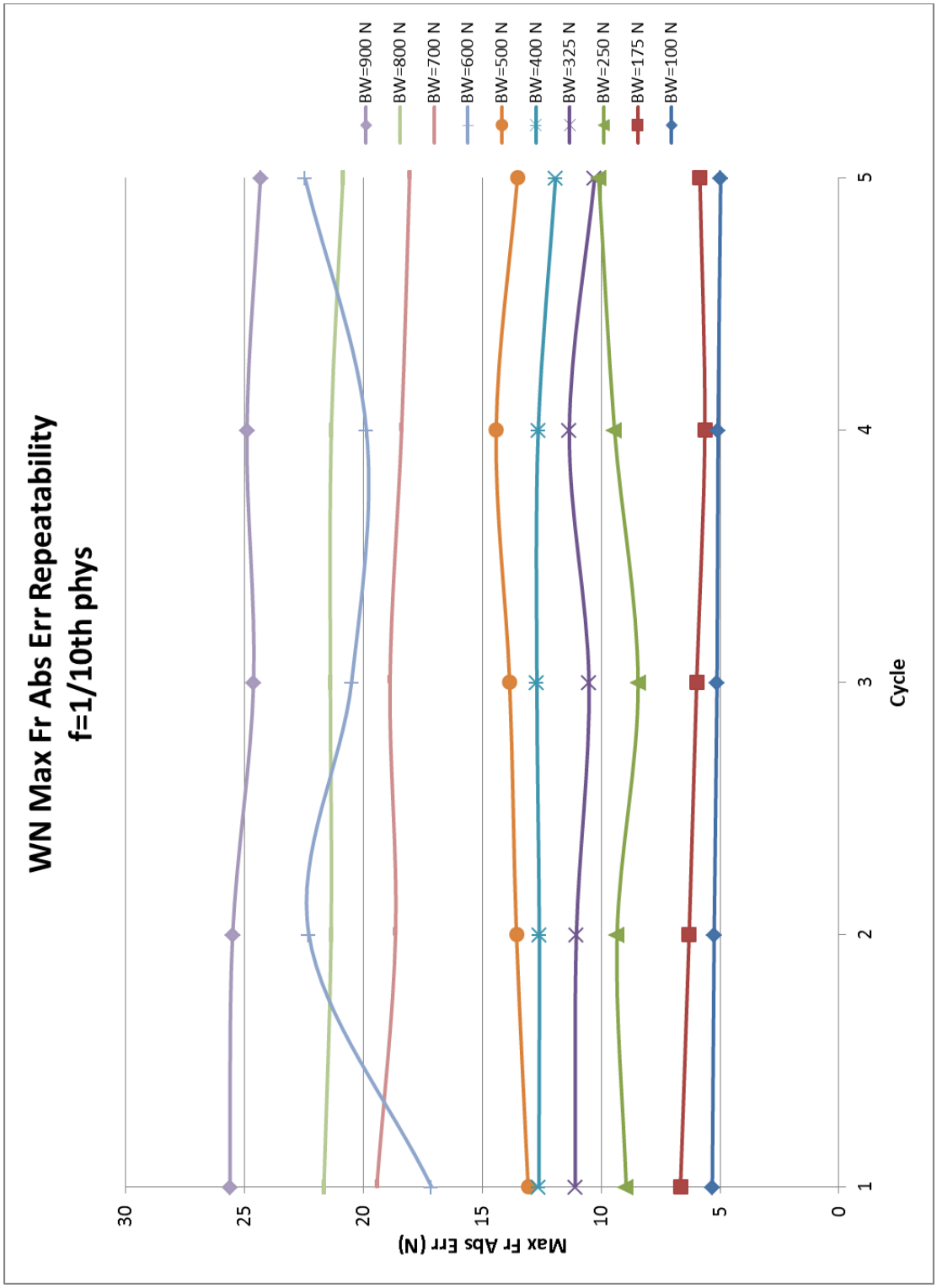

Figure 20. WN Max F_R Abs Err repeatability at 1/10th Phys.

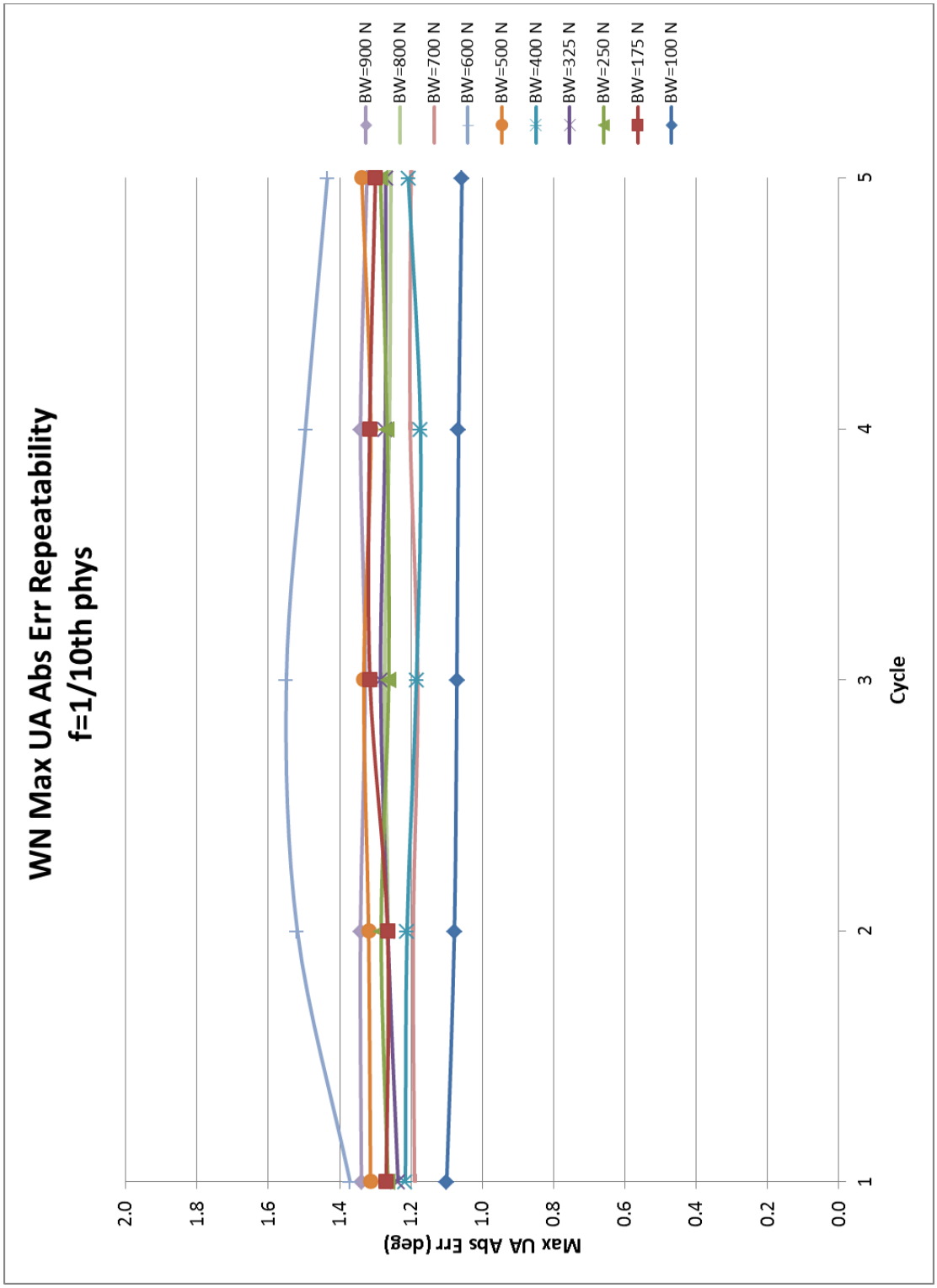

Figure 21. WN Max UA Abs Err repeatability at 1/10th Phys.

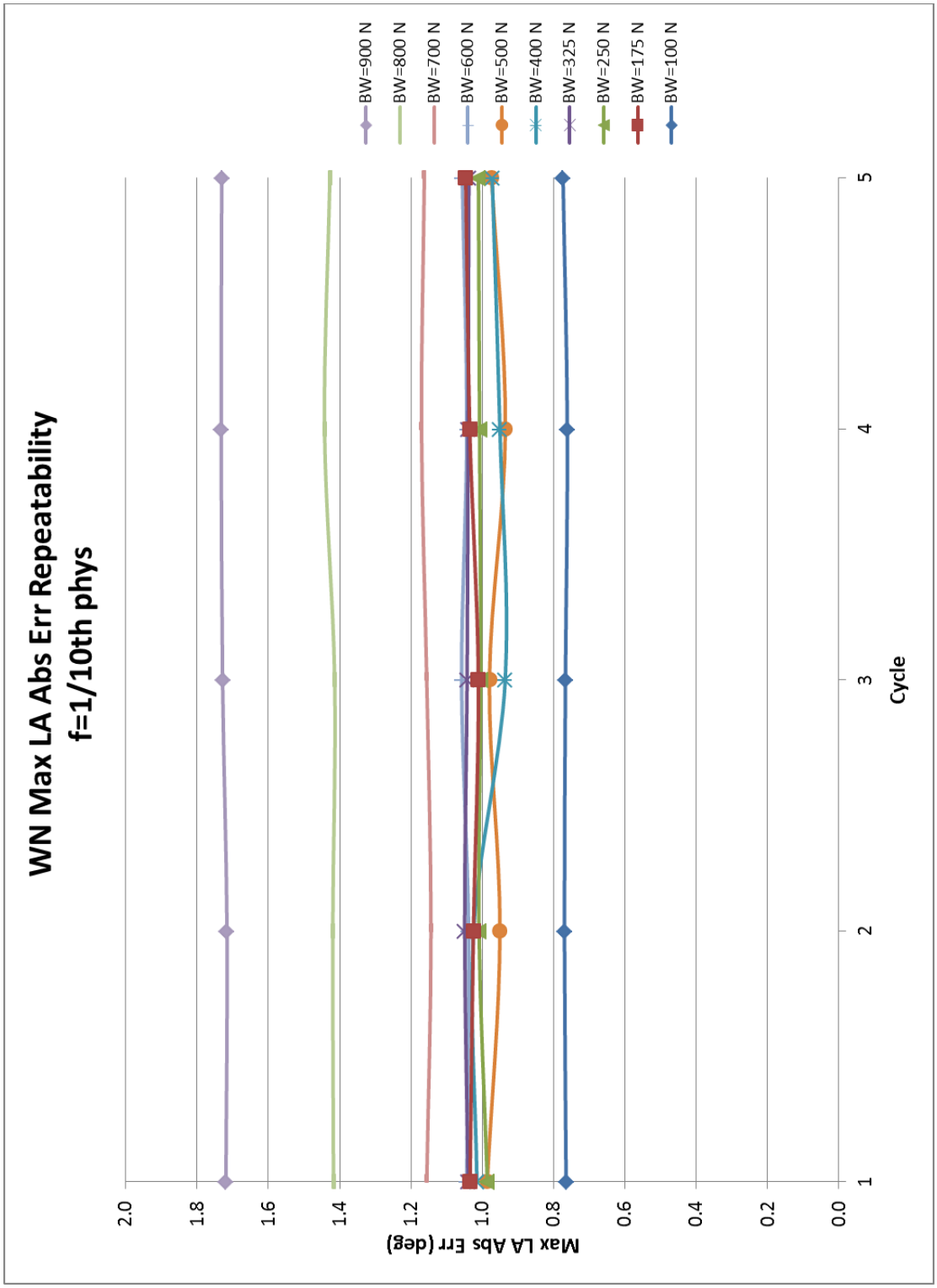

Figure 22. WN Max LA Abs Error repeatibility at 1/10th Phys.

4.6 Command, Output, and Error Charts

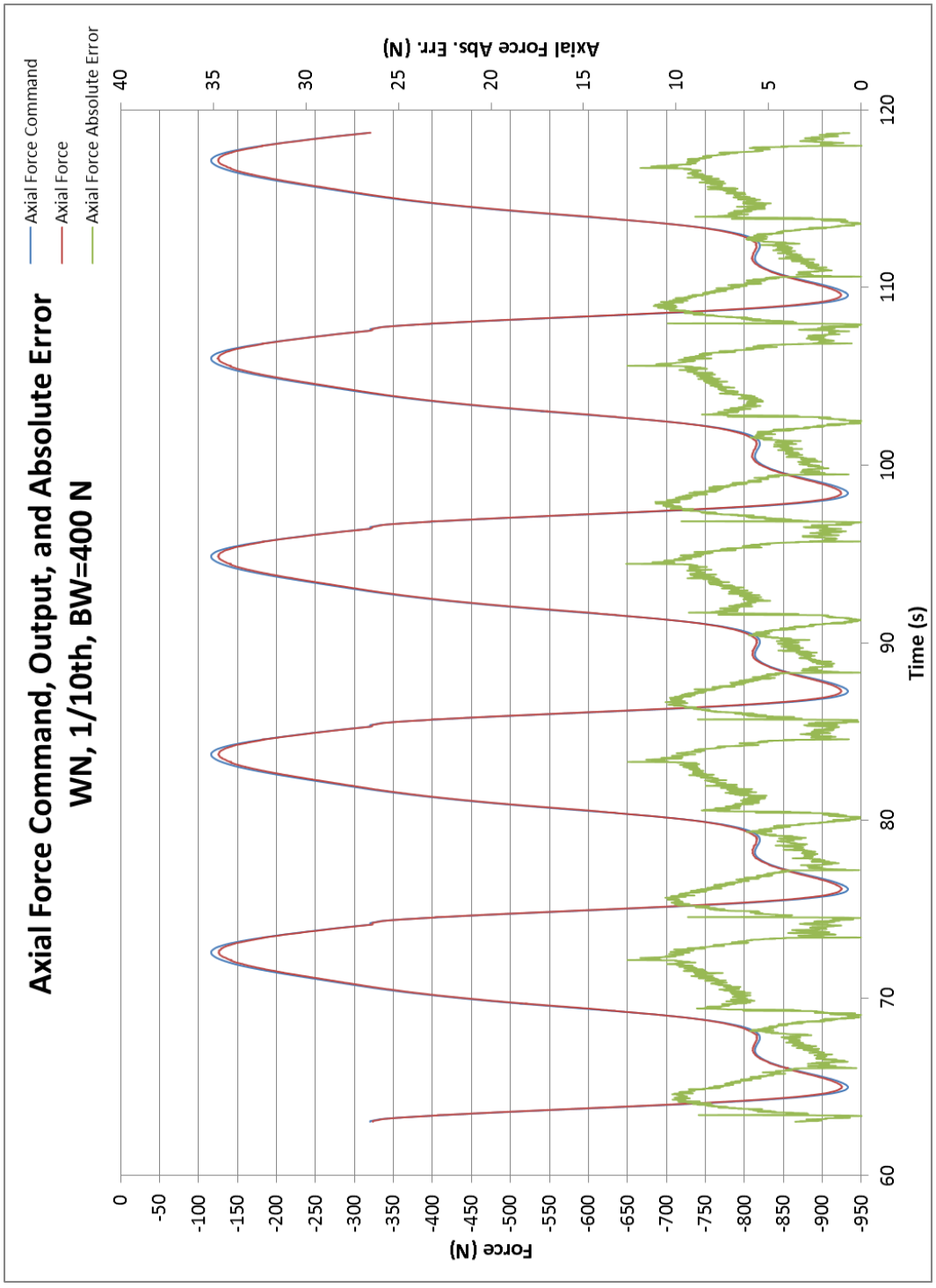

Figure 23. **Axial force command, output, and Abs Err for WN at 1/10th physiological speed with BW=400 N.**

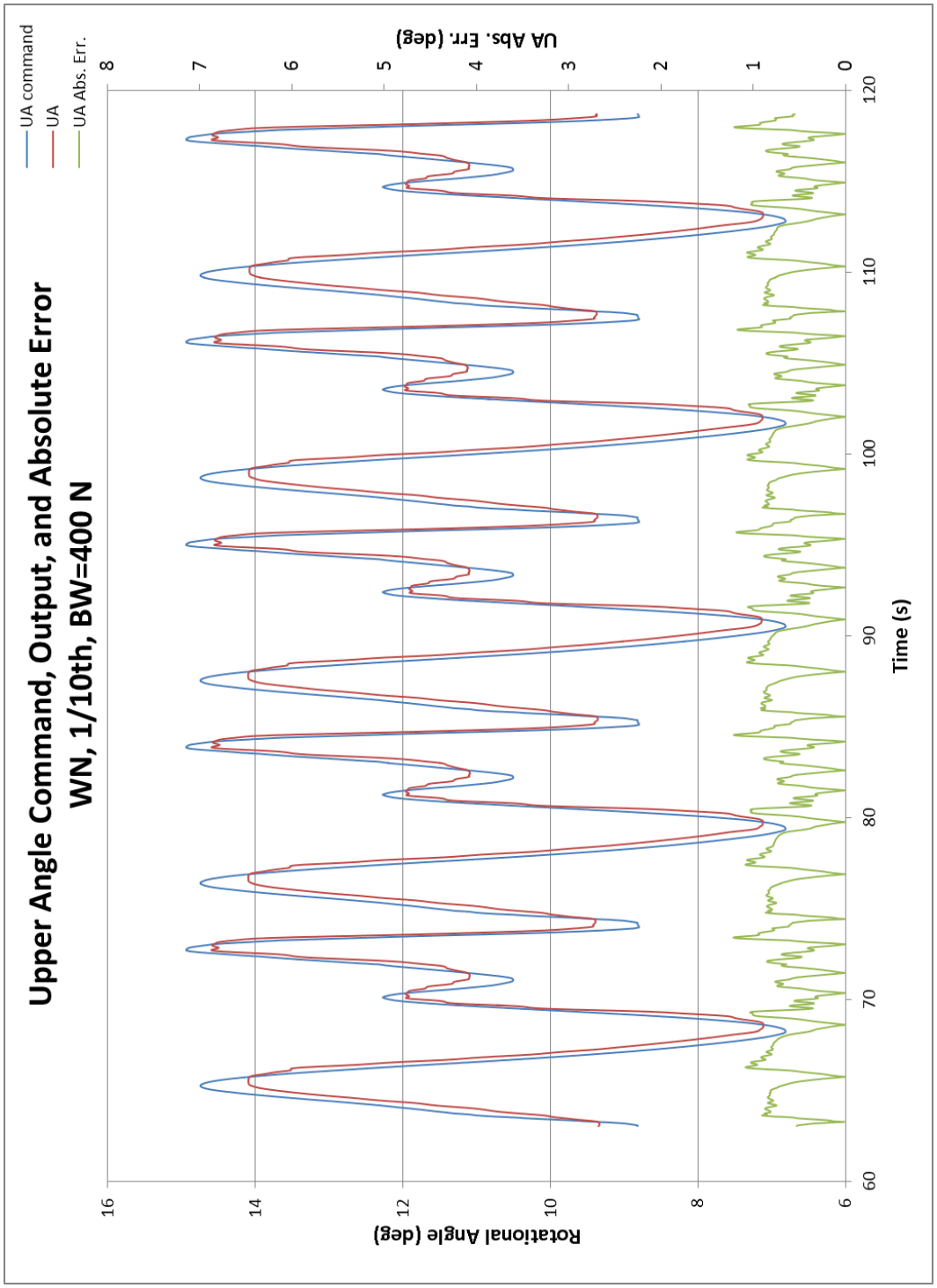

Figure 24. **UA command, output, and Abs Err for WN at 1/10th physiological speed with BW=400 N.**

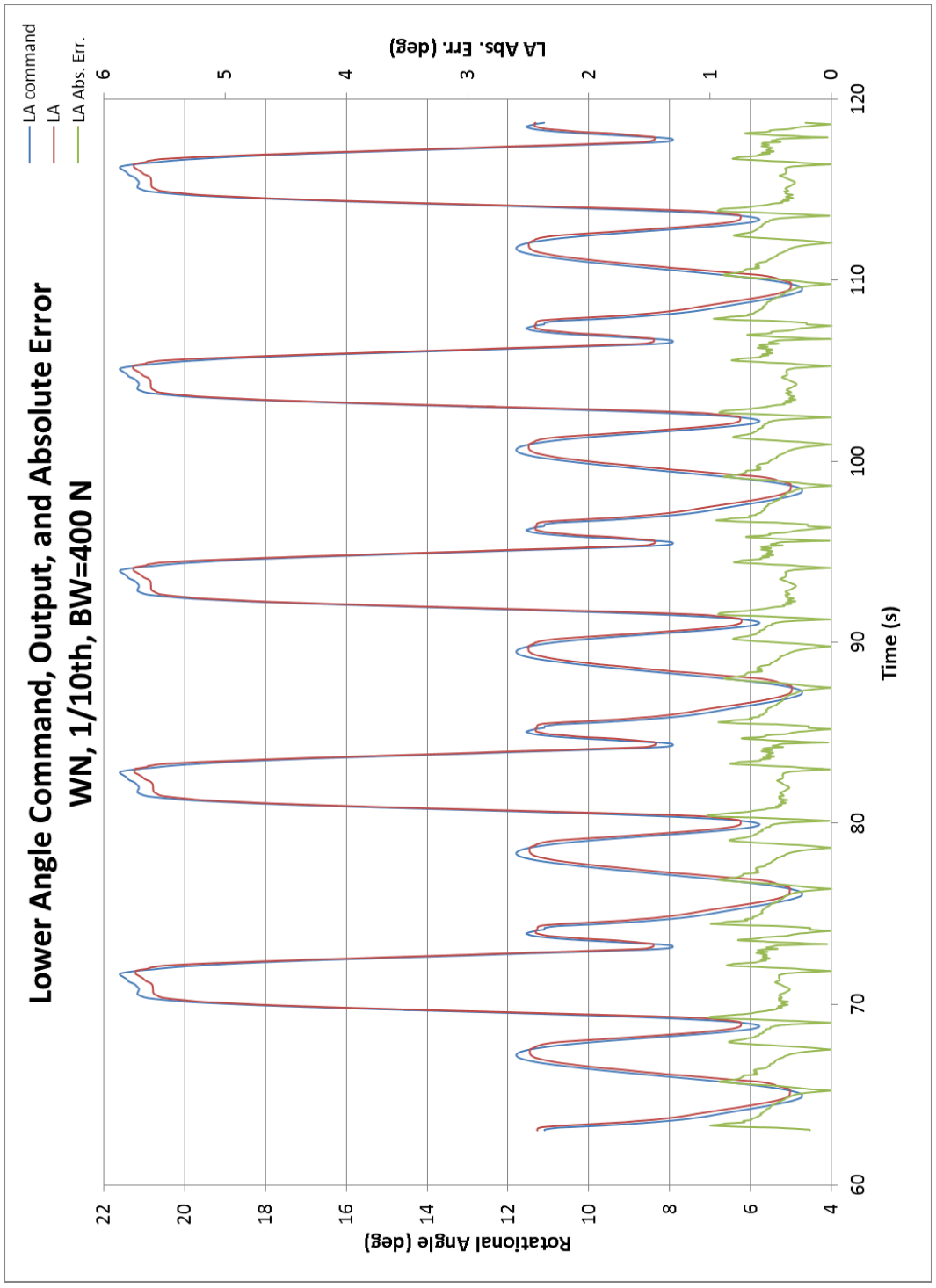

Figure 25. LA command, output, and Abs Err for WN at 1/10th physiological speed with BW=400 N.

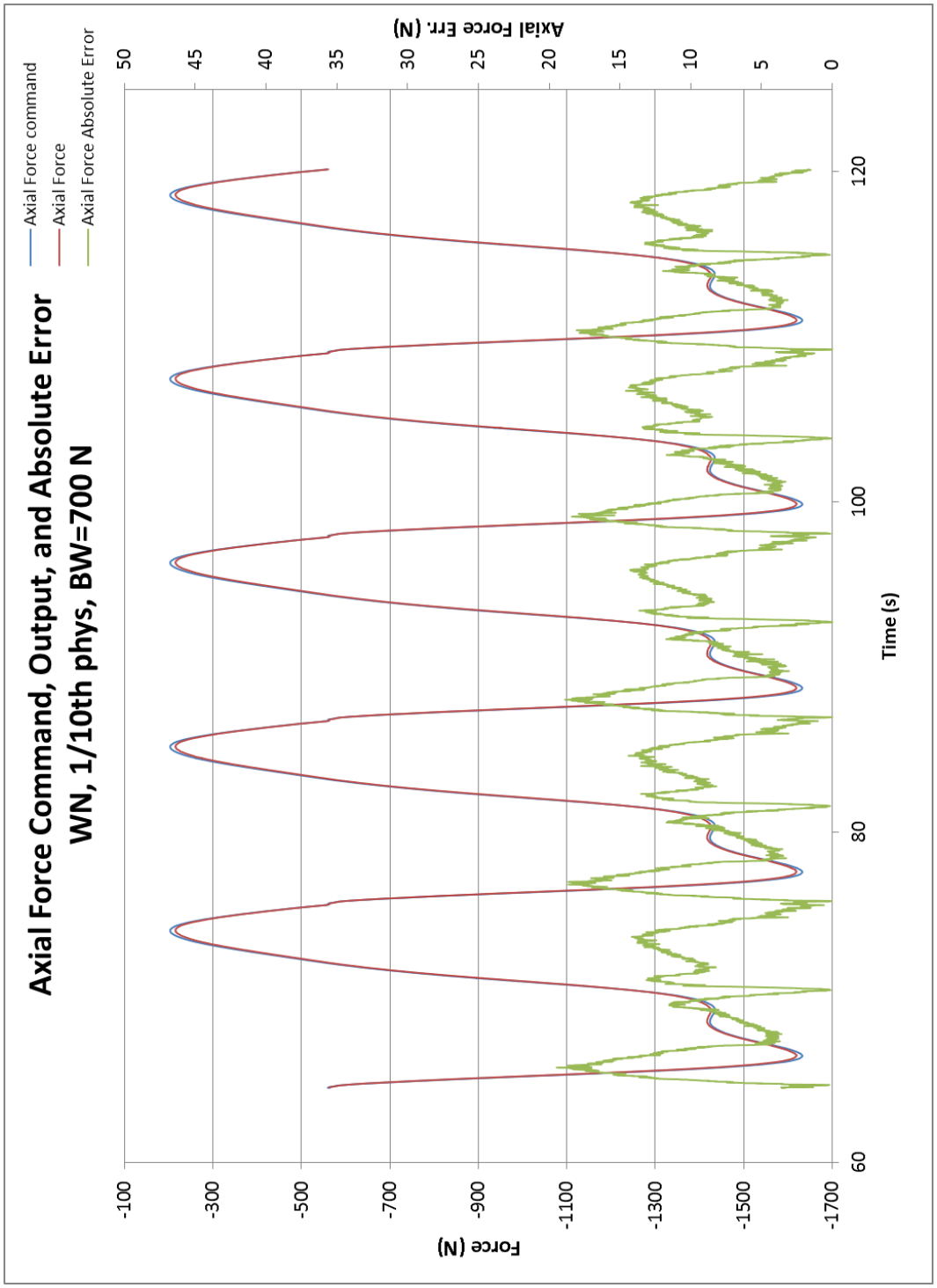

Figure 26. Axial force command, output, and Abs Err for WN at 1/10th physiological speed with BW=700 N.

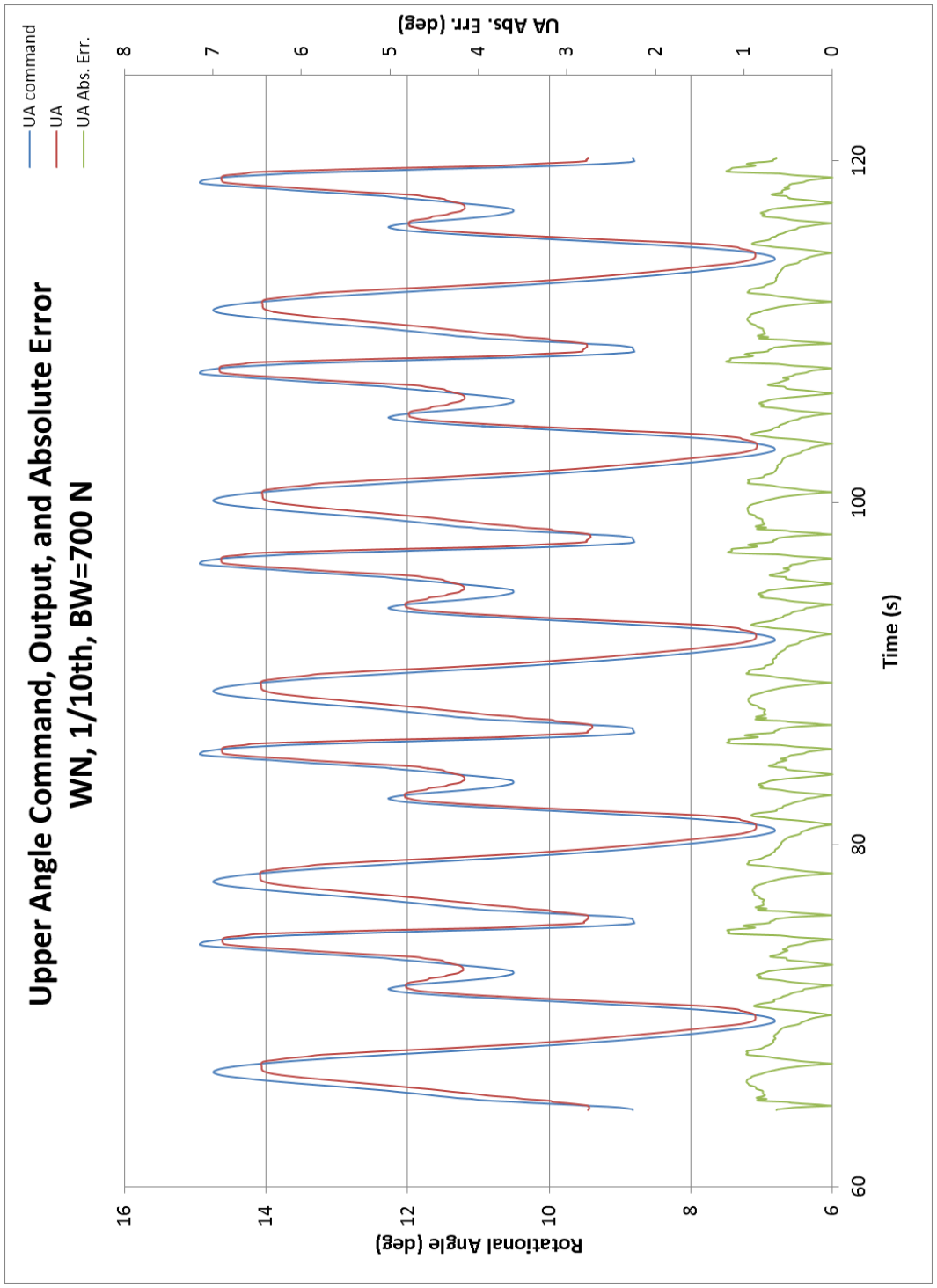

Figure 27. UA command, output, and Abs Err for WN at 1/10th physiological speed with BW=700 N.

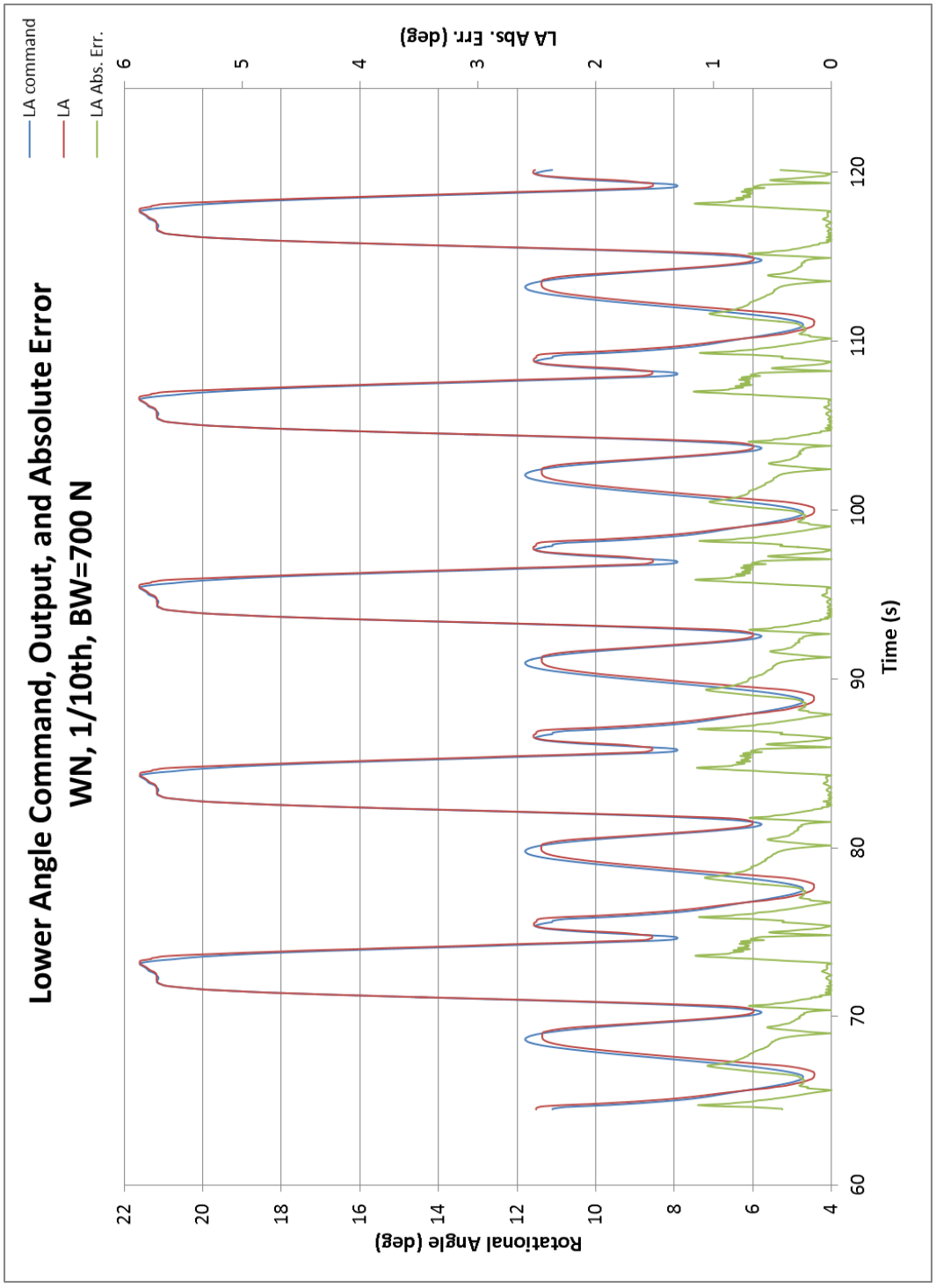

Figure 28. **LA command, output, and Abs Err for WN at 1/10th physiological speed with BW=700 N.**

4.7 Tuning Parameters

Tuning parameter values were experimentally obtained for each channel of the DBSJFS. The exact parameter settings were derived after extensive testing, focusing on parameters that provided the most stability to the system, allowed the smoothest pendulum movement, and limited the amount of error produced (see Table 1). The axial channel was controlled through force commands through the actual gait cycle; however, at the beginning and end of each procedure, the axial channel was controlled with point-to-point displacement. This gave the system more stability and limited the risk of inadvertently breaking a specimen. Both the upper and lower channels were controlled using point-to-point displacement for each procedure.

Table 1. Tuning Parameter Values.

		Channel			
		Axial (Force)	Axial (Displacement)	Upper	Lower
Tuning Parameters	P	40.0000	15.2500	0.38590	0.60000
	I	1.8220	1.5000	0.02300	0.06000
	D	0.0019	0.0000	0.03678	0.00359
	F	0.0000	0.0000	0.09923	0.07241
	F2	0.0000	0.0000	0.00307	0.00000
	FL Filter	1044.6 Hz	2048 Hz	2048 Hz	2048 Hz

Chapter 5 DISCUSSION

Chapter 5 DISCUSSION

5.1 Analysis of Performance

The decrease in the average force error for walking normally at a body load of 600N may be caused by optimizing the tuning parameters (**Error! Reference source ot found.**). The values used were the same for all the tests but may have been better for that particular loading pattern. Ideally, the DBSJFS should be tuned separately for each loading pattern to achieve the lowest error. This may also be the cause of the reduced error in GU and DS average force error at body loads of 400 and 600 N (Figure F 1). Further testing and tuning optimization may show errors in the other tests can be reduced if proper adjustments are made to the PID, F, F2, and FL filter settings.

Maximum errors in the hydraulic rotary actuators also correlated with peak loads being applied to the femoral head because, as the load applied through the head of the femur increases, the friction force between the linear actuator and the femoral head also increases. This resulted in more femoral deflection away from the intersection of the X' and Y' axes. Thus, because of these two affects, the rotary actuators must operate under sufficient force to oppose their motion. The center of the femoral head tended to deviate from the rotational center point of the rotary actuators when maximal errors were produced by the force applied by the linear actuator. The linear actuator had to adapt to a larger vertical adjustment as the center of rotation for the femur changed, causing the femur to displace along the Z axis. These effects are

minimal at low loads and frequencies, but they amplify each other as demands no the DBSJFS increase.

Repeatability of the gait cycles in the DBSJFS was high. The absolute error produced by each channel throughout the gait cycles was nearly the same in every test for a given load and frequency as can be seen in the error repeatability charts. However, the repeatability of the maximum force and upper angle error for walking normally for the test run at 600 N and at $1/10^{th}$ physiological speed was not as high as the other tests (Figure 20). The reason remains unknown; however, an increase in maximum error in either channel may have contributed to increased maximum error in the other. Note, however, the average force and upper angle error for walking normal in this same test was reliable and consistent.

The direction of the error for each channel was the same; all the actuators tended to under-shoot maximum and minimum values. Because of this high level of repeatability, the error charts can accurately estimate the error that will occur during a given test with specified loads and frequencies. This valuable information can determine if the DBSJFS functions at a required level of accuracy.

The maximum error produced by the both the linear actuator and the hydraulic rotary actuators tends to occur at points in each gait cycle where the actuators must reach the highest velocities. Again, the exact cause remains unknown; it is most likely a multi-factorial issue. However, lag in the system may contribute to maximum error because the slope of the command positional values is nearly the same as the slope of the actual positional data recorded. Thus, the speed at which the actuators can operate

was most likely not exceeded. However, this cannot be confirmed because torque values during the gait cycles were not recorded. Therefore, we do not know if the actuators were ever commanded to operate beyond their physical limitations.

Finally, the average and maximum error occurring during SU and SD at a load of 400 N at both recorded frequencies was due to abnormally large amount of vibration in the DBSJFS. These particular tests were repeated several times, and the vibrations occurred each time. Why the DBSJFS vibrated to the extent that it did during this test we do not know; however, the vibrations appear to be load dependent and may have been caused by singularities in the MTS control algorithm.

5.2 Limitations

The DBSJFS is limited by several factors. The range of motion of the rotary actuators is only +/- 60 degrees, and while it was not a limiting factor for reproducing the gait cycles of WN, GU and DS, and SU and SD, in a study of the extremes of human range of motion it could be an issue. The columns of the MTS machine also pose a significant limitation to the range of motion that the pendulum could swing though, requiring a careful review of the motion envelope before testing to prevent broken or damaged equipment. Another limitation of the system is the ability of the actuators to respond quickly. To increase responsiveness, the pressure of the hydraulic fluid can be increased and/or the size of the valves can be increased to allow more flow of fluid and thus increase responsiveness. New hydraulic rotary actuators could improve the design and are discussed in the following section. The

tuning parameters are significant to how the system responds. The system could achieve low error in all three channels throughout most of the testing but could still be improved. The current PID algorithm in the MTS software does not adaptive to a dynamic system; therefore, any deviation from the particular setting will cause an increase in error. Moreover, deflection of the femur began to cause errors at loads surpassing 700 N. This was minimized by shortening the length of the femur so that less deflection would occur at any given load. Lastly, although the resultant force applied through the head of the femur is accurately reproduced when compared to in vivo forces, the shear stresses experienced by the femoral component are not the same because the DBSJFS does not replicate the forces produced by the muscles surrounding the hip joint. The deviation caused by this is unknown and was not analyzed.

5.3 Suggested Design Improvements

Many aspects of the DBSJFS could be improved. First, the pendulum could be made out of a lighter and stronger material like carbon fiber or titanium. This would reduce the inertia of the pendulum, enabling the hydraulic rotary motors to move it more quickly. Second, the rotary motors could be upgraded. Currently, the hydraulic motors are model number SS.2A 1V made by Flow Products Company. They are single vane, weigh 1.6 lbs, have a max torque of 510 in-lbs @ 3000 psi, and can reach an angular velocity of 11.02 rad/sec. Two different models are being reviewed to improve the DBSJFS performance.

The first is model number SS.5A 1V, a single vane unit weighing 3.0 lbs and producing 760 in-lbs of torque at 2000 psi. However, it can only reach an angular velocity of 4.30 rad/sec. It also has a high range of motion because it can rotate +/- 140 degrees. The second model, SS.5A 2V, is a double vane unit weighing 3.2 lbs and producing 1620 in-lbs at 2000 psi. However, the SS.5A 2V can only rotate +/-50 degrees and has an angular velocity of only 2.15 rad/sec. The disadvantage of the reduced angular velocity could be significantly improved by doubling the ports and/or enlarging the port area, which would increase flow rate and speed.

An additional improvement would be to redesign the swing arms of the pendulum so that shoulder bolts are used for the vertical adjustment connections. This would strengthen the design by taking force off the bolt threads.

5.4 Testing in Future Studies

The DBSJFS could be used to study implant micromotion for both hip and shoulder prosthetics or any other ball and socket joint. Initial design of these studies should use differential variable reluctance transducers (DVRT) to record the micromotion at the bone-implant interface. These devices are sensitive enough to detect motion as small as 6 μm. Additionally, the gait cycles developed for the DBSJFS validation can also be used. However, preliminary work must be done to ensure the proper performance of the devices.

5.4.1 Specimen Desciption

Parameters that need to be recorded on specimens used in future studies are age, sex, fresh frozen tissue or embalmed, cause of death, height, weight, and bone density.

5.4.2 Preparation of Specimens

After being harvested in the procedure room within the orthopedic research laboratory at the University of Kansas Medical Center, the femurs used should be prepared in the following way. Each specimen must bagged, sealed, and placed in a freezer kept at -31°F. When the femurs are needed, the thighs can be removed from the freezer and allowed to thaw overnight. The following day, the soft tissue can be excised, and the stem implanted according to the manufacturer specifications. The surgical procedure should follow the Mayo Design femoral component instructions, given in Appendix E. Placement of each stem must be checked after implantation using a Flouroscan to assure correct positioning.

5.4.3 Potting Process

Once all the soft tissue from the femur is excised and the stem implanted, the distal end of the femur should be potted in the aluminum cup of the pendulum described in section 2 of Chapter 3.

5.4.4 Micromotion Measurements

The movement between the implant and the bone can be measured at the bone-implant interface with DVRTs. This motion can be captured by fixing the casing of the DVRTs to the outside of the bone with the stainless steel probe tip passing through prepared holes and placed in direct contact with the surface of the implant. These instruments would be placed in different planes around the femur to collect data on motion in the X, Y, and Z axes.

5.4.5 Loading Profiles

The procedures for WN, GU and DS, and SU and SD may be used for both right and left hips. These procedures can be run at a known maximum of 900 N at 1/3rd physiological speed. The number of cycles completed and the order of the profiles can be adjusted to mimic actual use. To help determine these parameters, the following pedometric studies can be reviewed:

1. Atkinson, J., R.B. Goody, and C.A. Walker, *Walking at Work, A Pedometric Study Assessing The Activity Levels of Doctors*. Scottish Medical Journal, 2005. **50**(2): p. 73-74.
2. Miller, R. and W. Brown, *Steps and Sitting in a Working Population*, International Journal of Behavioral Medicine, 2004. **11**(4): p. 219-224.
3. Morlock, M., E. Schneider, A. Bluhm, M. Vollmer, G. Bergmann, V. Müller, and M. Honl, *Duration and frequency of every day activities in total hip patients*. Journal of Biomechanics, 2001: p. 873-881.
4. Schmalzried, T.P., E.S. Szuszczewicz, M.R. Northfield, K.H. Akizuki, R.E. Frankel, G. Belcher, and H.C. Amstutz, *Quantitative Assessment of Walking Activity after Total Hip or Knee Replacement*. The Journal of Bone and Joint Surgery, 1998: p. 54-59.

5.4.6 PID Tuning

The PID setting for future studying should be slightly adjusted because the stiffness of real bone differs from the 3rd generation saw bone used in this validation of the DBSJFS. However, the values should to be similar because the saw bone was made to mimic real tissue.

References

1. Dutton, M., *Orthopedic Examination, Evaluation, & Intervention*. 2004: McGraw Hill. 1459.
2. Sanfilippo, J.A. and M.S. Austin, *Implants for total hip arthroplasty.* Expert Rev Med Devices, 2006. **3**(6): p. 769-76.
3. Morrey, B.F., R.A. Adams, and M. Kessler, *A conservative femoral replacement for total hip arthroplasty. A prospective study.* J Bone Joint Surg Br, 2000. **82**(7): p. 952-8.
4. Kurtz, S., et al., *Trend shows growing orthopedic surgery case load. Will surgeons be able to keep up?* Mater Manag Health Care, 2006. **15**(7): p. 61-2.
5. Kurtz, S., et al., *Projections of primary and revision hip and knee arthroplasty in the United States from 2005 to 2030.* J Bone Joint Surg Am, 2007. **89**(4): p. 780-5.
6. Hailer, N.P., G. Garellick, and J. Karrholm, *Uncemented and cemented primary total hip arthroplasty in the Swedish Hip Arthroplasty Register.* Acta Orthop. **81**(1): p. 34-41.
7. Omlor, G.W., et al., *A stature-specific concept for uncemented, primary total hip arthroplasty.* Acta Orthop. **81**(1): p. 126-33.
8. Cutts, S. and P.B. Carter, *Hip resurfacing: a technology reborn.* Postgrad Med J, 2006. **82**(974): p. 802-5.

9. Effenberger, H., et al., *A model for assessing the rotational stability of uncemented femoral implants.* Arch Orthop Trauma Surg, 2001. **121**(1-2): p. 60-4.

10. Hirakawa, K., et al., *Mechanisms of failure of total hip replacements: lessons learned from retrieval studies.* Clin Orthop Relat Res, 2004(420): p. 10-7.

11. Mont, M.A. and D.S. Hungerford, *Proximally coated ingrowth prostheses. A review.* Clin Orthop Relat Res, 1997(344): p. 139-49.

12. Dobzyniak, M., T.K. Fehring, and S. Odum, *Early failure in total hip arthroplasty.* Clin Orthop Relat Res, 2006. **447**: p. 76-8.

13. Callaghan, J.J., et al., *The effect of femoral stem geometry on interface motion in uncemented porous-coated total hip prostheses. Comparison of straight-stem and curved-stem designs.* J Bone Joint Surg Am, 1992. **74**(6): p. 839-48.

14. Dujovne, A.R., et al., *Mechanical compatibility of noncemented hip prostheses with the human femur.* J Arthroplasty, 1993. **8**(1): p. 7-22.

15. Ratner, B.D., *Biomaterials Science: An Introduction to Materials in Medicine*. 2nd Edition ed. 2004, San Diego: Elsevier Academic Press.

16. Oonishi, H., et al., *The effect of hydroxyapatite coating on bone growth into porous titanium alloy implants.* J Bone Joint Surg Br, 1989. **71**(2): p. 213-6.

17. Cohen, R., *A porous tantalum trabecular metal: basic science.* Am J Orthop, 2002. **31**(4): p. 216-7.

18. Stiehl, J.B., *Trabecular metal in hip reconstructive surgery.* Orthopedics, 2005. **28**(7): p. 662-70.

19. Monti, L., L. Cristofolini, and M. Viceconti, *Methods for quantitative analysis of the primary stability in uncemented hip prostheses.* Artif Organs, 1999. **23**(9): p. 851-9.

20. Harman, M.K., et al., *Initial stability of uncemented hip stems: an in-vitro protocol to measure torsional interface motion.* Med Eng Phys, 1995. **17**(3): p. 163-71.

21. Incavo, S.J., R. Schneider, and J. Elting, *The effect of surface coating of femoral prostheses implanted without cement: a 2- to 4-year follow-up study.* Am J Orthop, 1998. **27**(5): p. 355-61.

22. Kuiper, J.H. and R. Huiskes, *Friction and stem stiffness affect dynamic interface motion in total hip replacement.* J Orthop Res, 1996. **14**(1): p. 36-43.

23. Hua, J. and P.S. Walker, *Relative motion of hip stems under load. An in vitro study of symmetrical, asymmetrical, and custom asymmetrical designs.* J Bone Joint Surg Am, 1994. **76**(1): p. 95-103.

24. Baleani, M., L. Cristofolini, and A. Toni, *Initial stability of a new hybrid fixation hip stem: experimental measurement of implant-bone micromotion under torsional load in comparison with cemented and cementless stems.* J Biomed Mater Res, 2000. **50**(4): p. 605-15.

25. Viceconti, M., et al., *Discussion on the design of a hip joint simulator.* Med Eng Phys, 1996. **18**(3): p. 234-40.

26. Goldsmith, A.A. and D. Dowson, *Development of a ten-station, multi-axis hip joint simulator.* Proc Inst Mech Eng [H], 1999. **213**(4): p. 311-6.

27. Dowson, D. and B. Jobbins, *Design and development of a versatile hip joint simulator and a preliminary assessment of wear and creep in Charnley total replacement hip joints.* Eng Med, 1988. **17**(3): p. 111-7.

28. Saikko, V.O., *A three-axis hip joint simulator for wear and friction studies on total hip prostheses.* Proc Inst Mech Eng [H], 1996. **210**(3): p. 175-85.

29. Saikko, V., *A 12-station anatomic hip joint simulator.* Proc Inst Mech Eng [H], 2005. **219**(6): p. 437-48.

30. Saikko, V., *A hip wear simulator with 100 test stations.* Proc Inst Mech Eng [H], 2005. **219**(5): p. 309-18.

31. Bragdon, C.R., et al., *The importance of multidirectional motion on the wear of polyethylene.* Proc Inst Mech Eng [H], 1996. **210**(3): p. 157-65.

32. Medley, J.B., et al., *Kinematics of the MATCO hip simulator and issues related to wear testing of metal-metal implants.* Proc Inst Mech Eng [H], 1997. **211**(1): p. 89-99.

33. Mejia, L.C. and T.J. Brierley, *A hip wear simulator for the evaluation of biomaterials in hip arthroplasty components.* Biomed Mater Eng, 1994. **4**(4): p. 259-71.

34. Green, A.S., et al., *The design and development of a triaxial wear-testing joint simulator.* Biomed Sci Instrum, 1999. **35**: p. 379-84.

35. Stamatakis, M., et al., *Clinical, radiographic, and scintigraphic comparison of the mechanical stability of Mueller and Zweymueller total hip prostheses.* Orthopedics, 1999. **22**(11): p. 1037-43.

36. Sugiyama, H., L.A. Whiteside, and A.D. Kaiser, *Examination of rotational fixation of the femoral component in total hip arthroplasty. A mechanical study of micromovement and acoustic emission.* Clin Orthop Relat Res, 1989(249): p. 122-8.

37. Gortz, W., et al., *Spatial micromovements of uncemented femoral components after torsional loads.* J Biomech Eng, 2002. **124**(6): p. 706-13.

38. Naidu, S.H., et al., *Initial stability of a modular uncemented, porous-coated femoral stem: a mechanical study.* Am J Orthop, 1996. **25**(12): p. 829-34.

39. Engh, C.A., et al., *Quantification of implant micromotion, strain shielding, and bone resorption with porous-coated anatomic medullary locking femoral prostheses.* Clin Orthop Relat Res, 1992(285): p. 13-29.

40. Kligman, M., A. Rotem, and M. Roffman, *Cancellous and cortical morselized allograft in revision total hip replacement: A biomechanical study of implant stability*. J Biomech, 2003. **36**(6): p. 797-802.

41. Schneider, E., et al., *A comparative study of the initial stability of cementless hip prostheses.* Clin Orthop Relat Res, 1989(248): p. 200-9.

42. Bergmann, G., et al., *HIP98*. 2001, Berlin.

43. Hallab, N.J., *Biomaterials Science: An Introduction to Materials in Medicine*. 2nd ed. `, ed. B.D. Ratner. 2004, San Diego: Elsevier Academic Press. 851.

APPENDICES

APPENDIX A

Implant Photos and Experimental Setup Diagrams

A.1. Implants

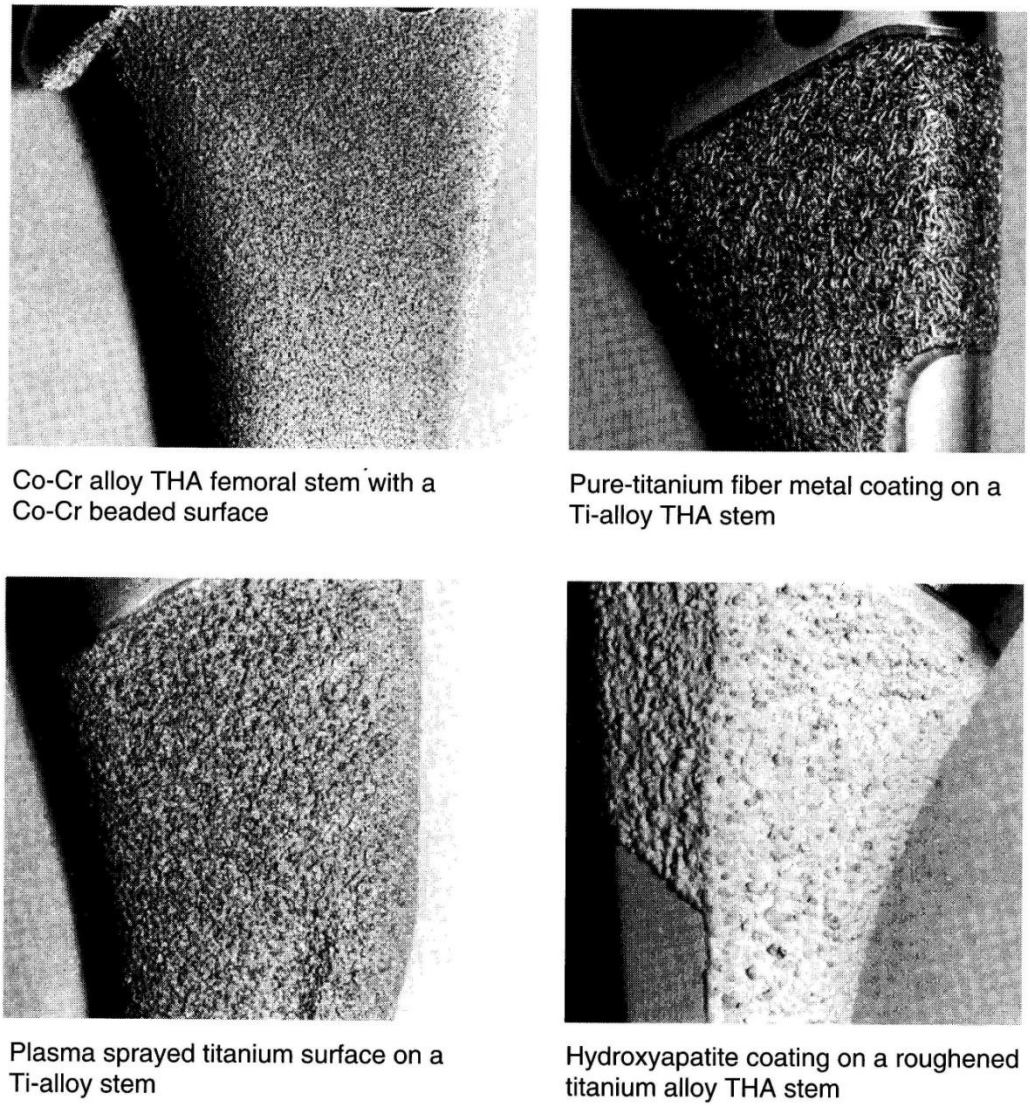

Figure A 1. Implant surface coatings [43].

A.2. Hip Wear Simulators

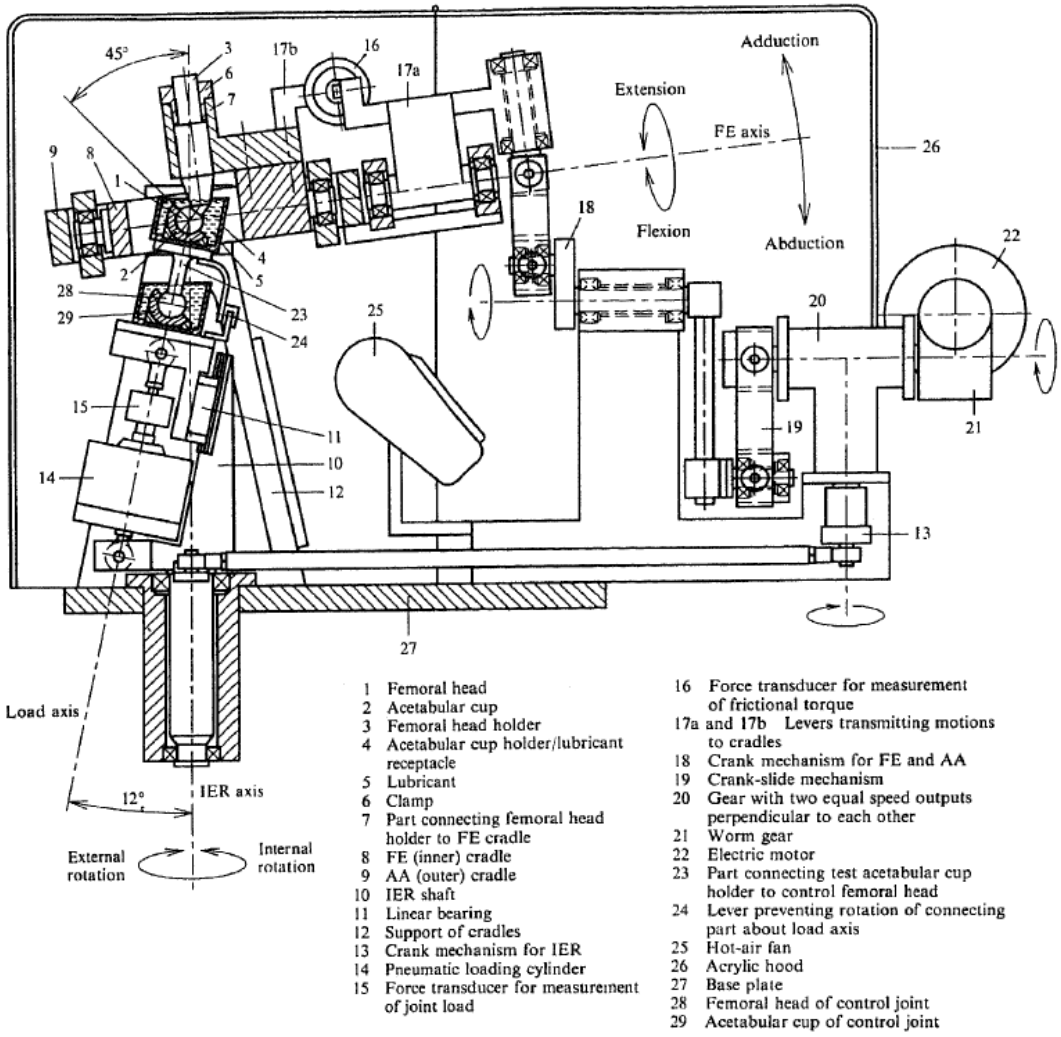

Figure A 2. Schematic of the HUT-3 hip joint simulator [28].

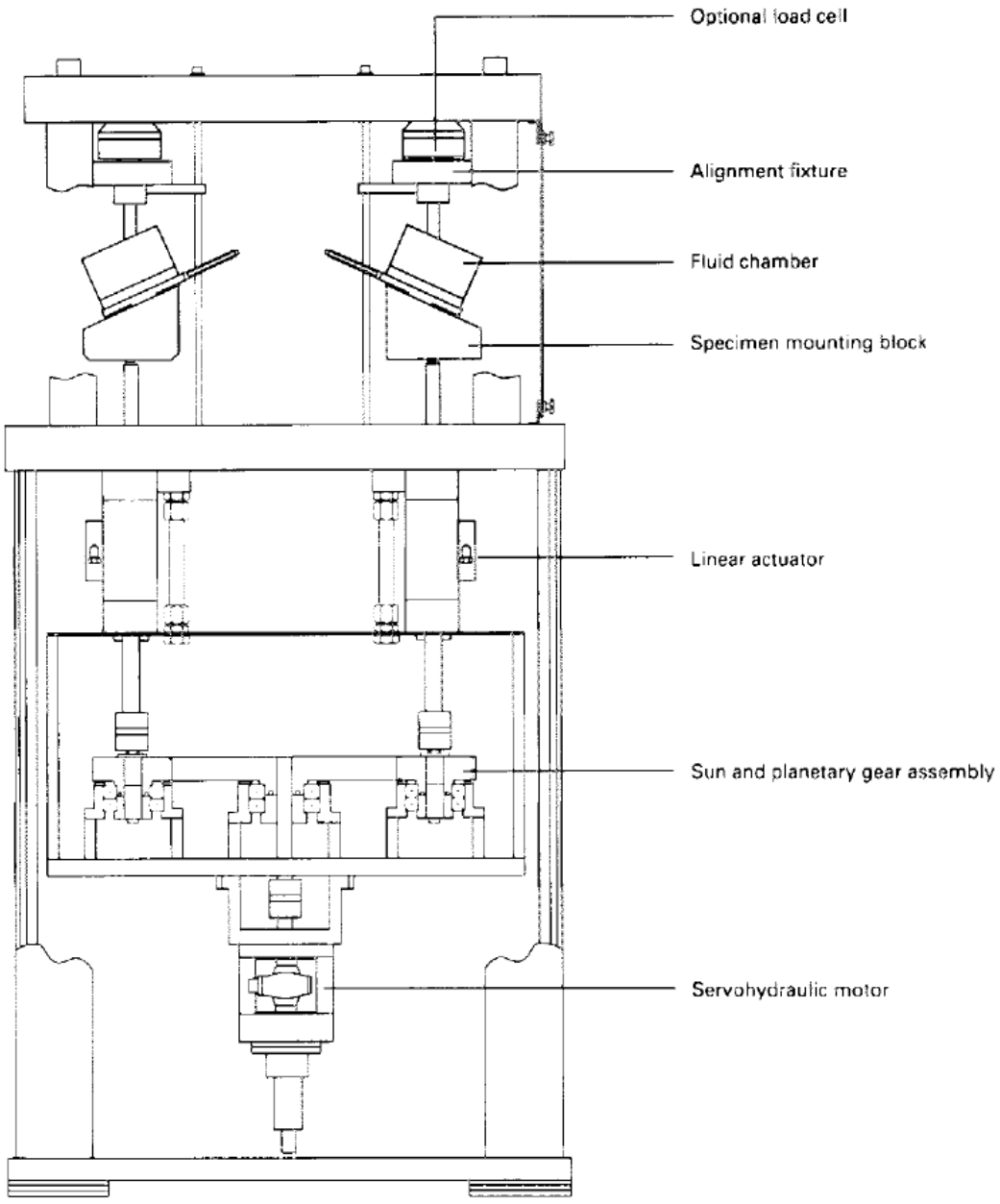

Figure A 3. Hip simulator loading configuration from Mejia [33].

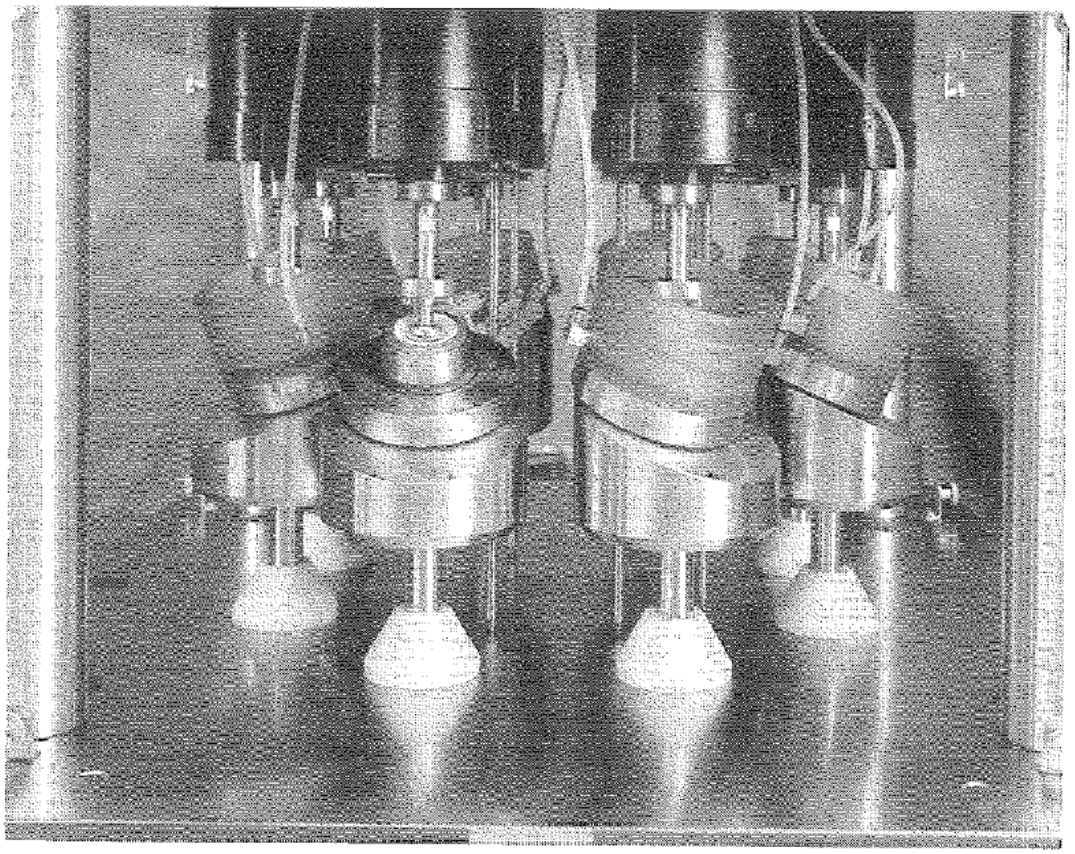

Figure A 4. Photo of hip simulator from Mejia [33].

A.3. Joint Force Simulators

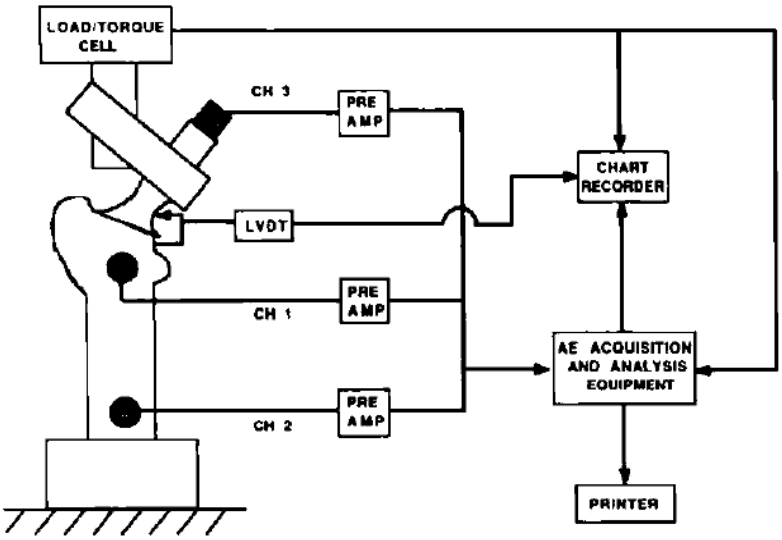

Figure A 5. Experimental setup used by Sugiyama [36].

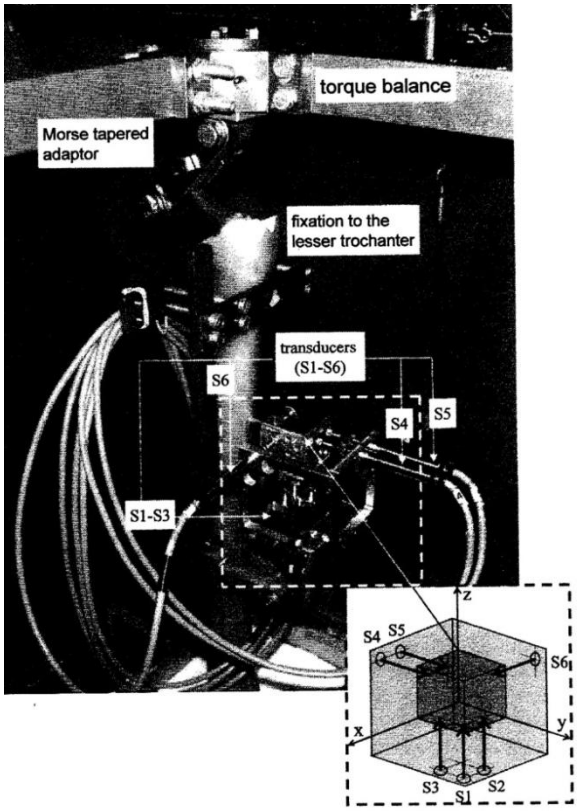

Figure A 6. Fixture used by Gortz for his experimental setup [37].

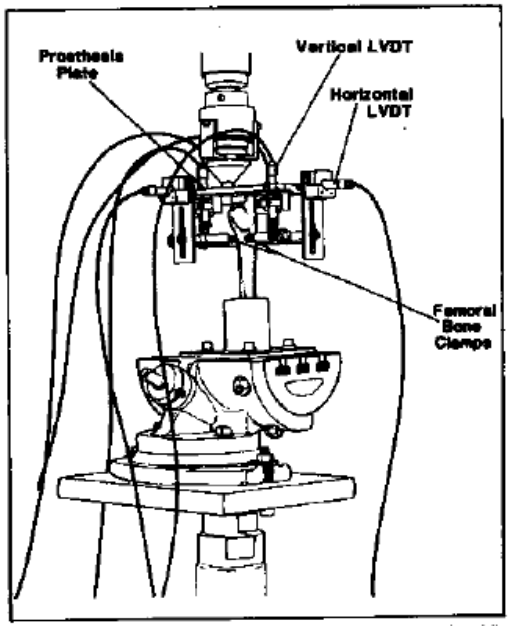

Figure A 7. Fixure used by Naidu for his experiment in evaluating initial stability of cementless femoral stems [38].

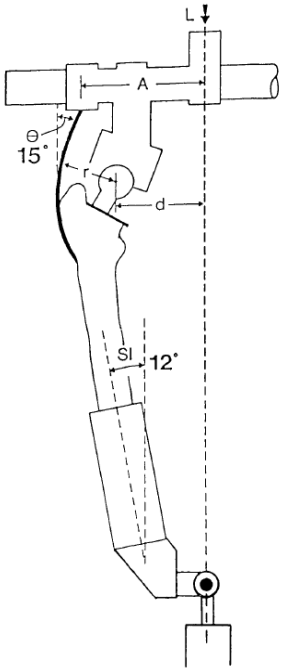

Figure A 8. Schematic of loading conditions used by Engh [39].

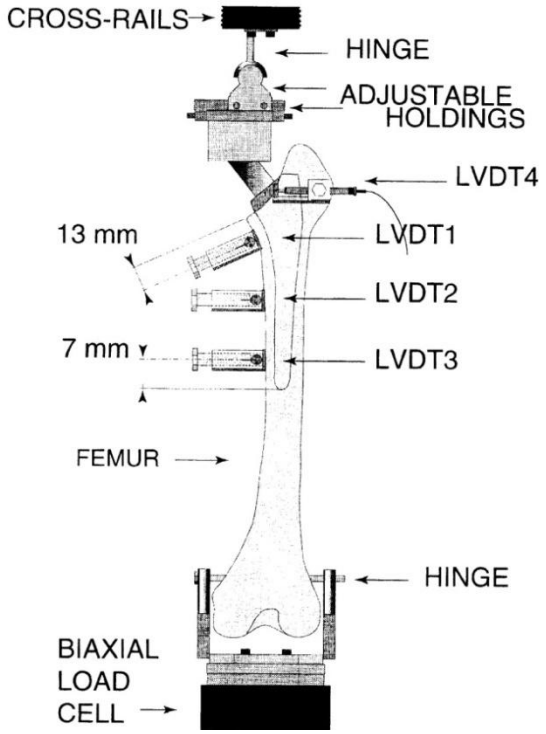

Figure A 9. Experimental setup used by Monti in testing femoral stem primary stability [19].

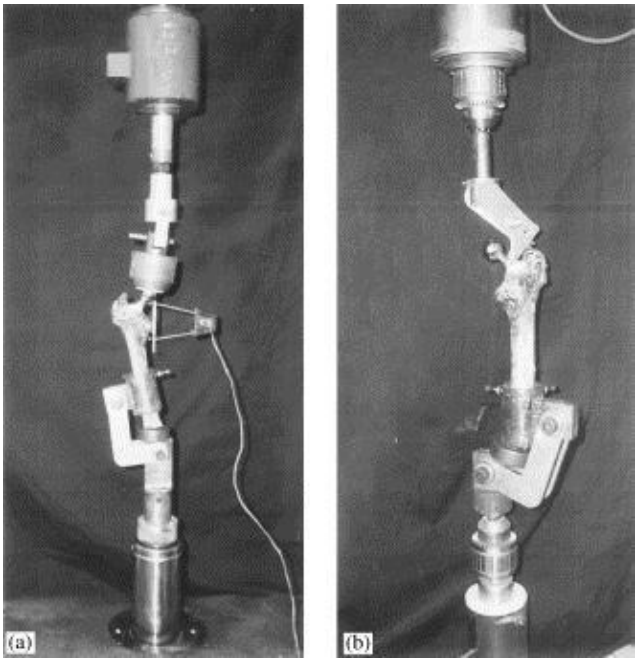

Figure A 10. Fixture used by Kligman implant stability study [40].

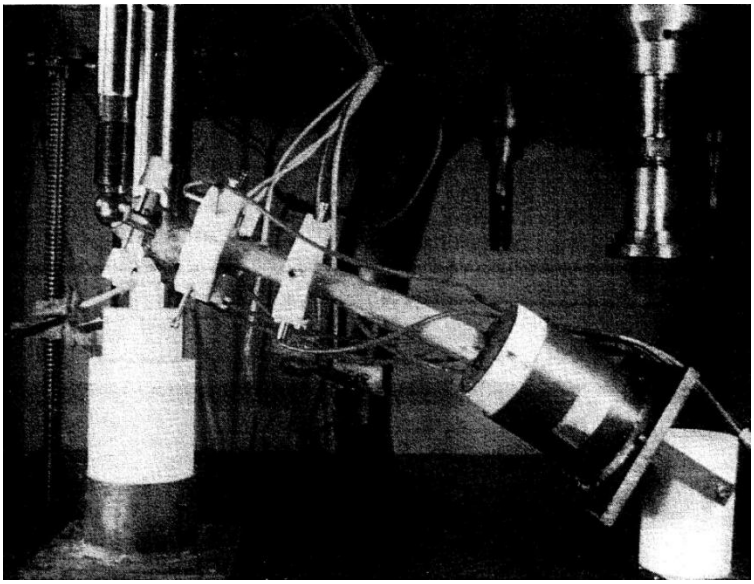

Figure A 11. Fixture used for torsional loading by Hua [23].

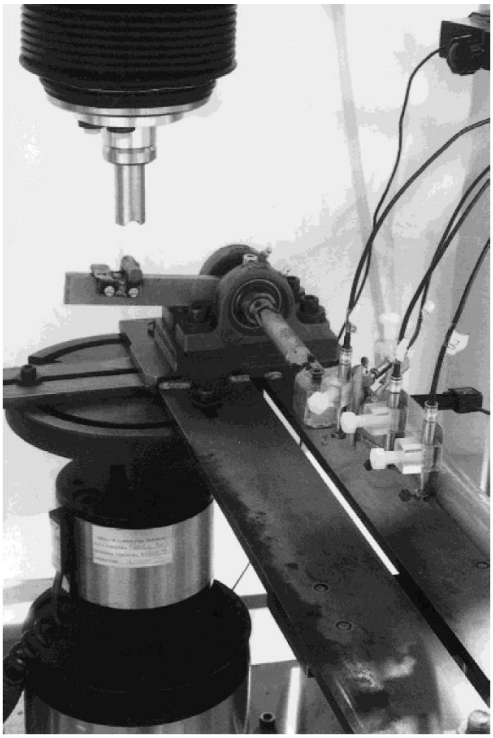

Figure A 12. Torsional stability test setup by Baleani [24].

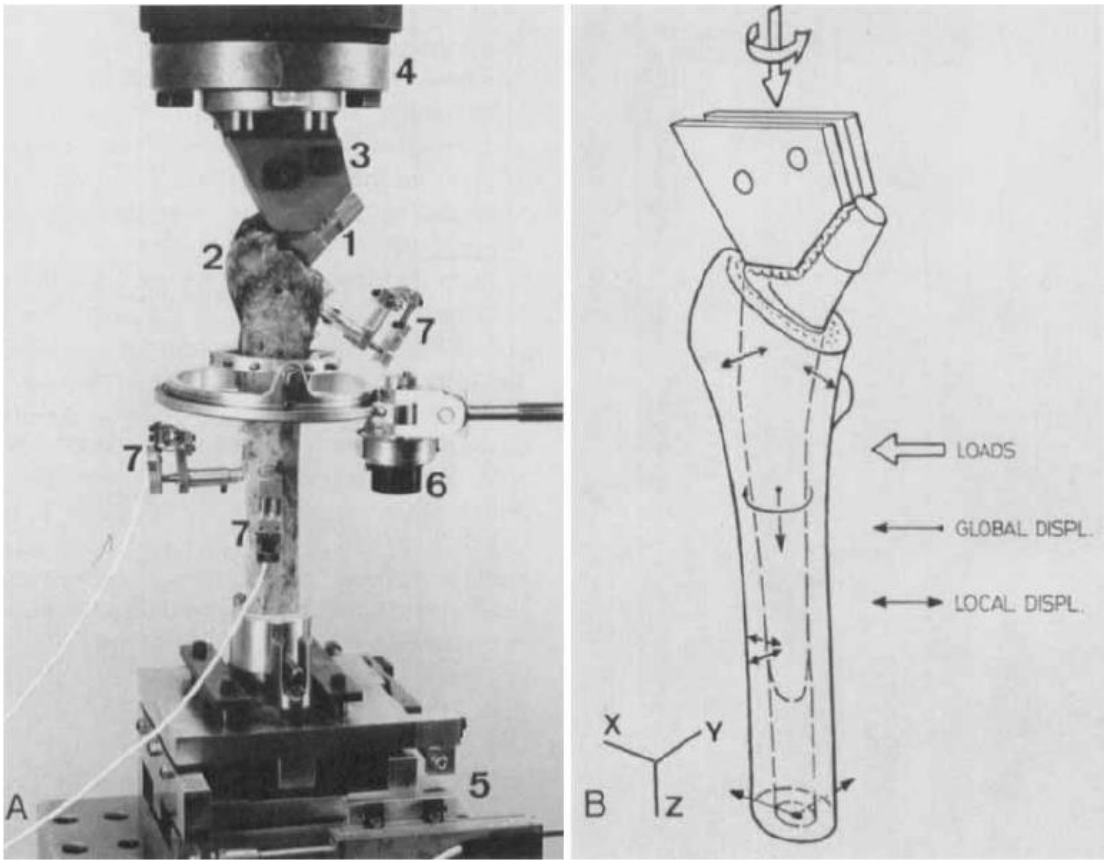

Figure A 13. Experimental fixture used by Schnieder for testing the initials stability of a hip prosthesis [41].

APPENDIX B

Hip Simulator Images

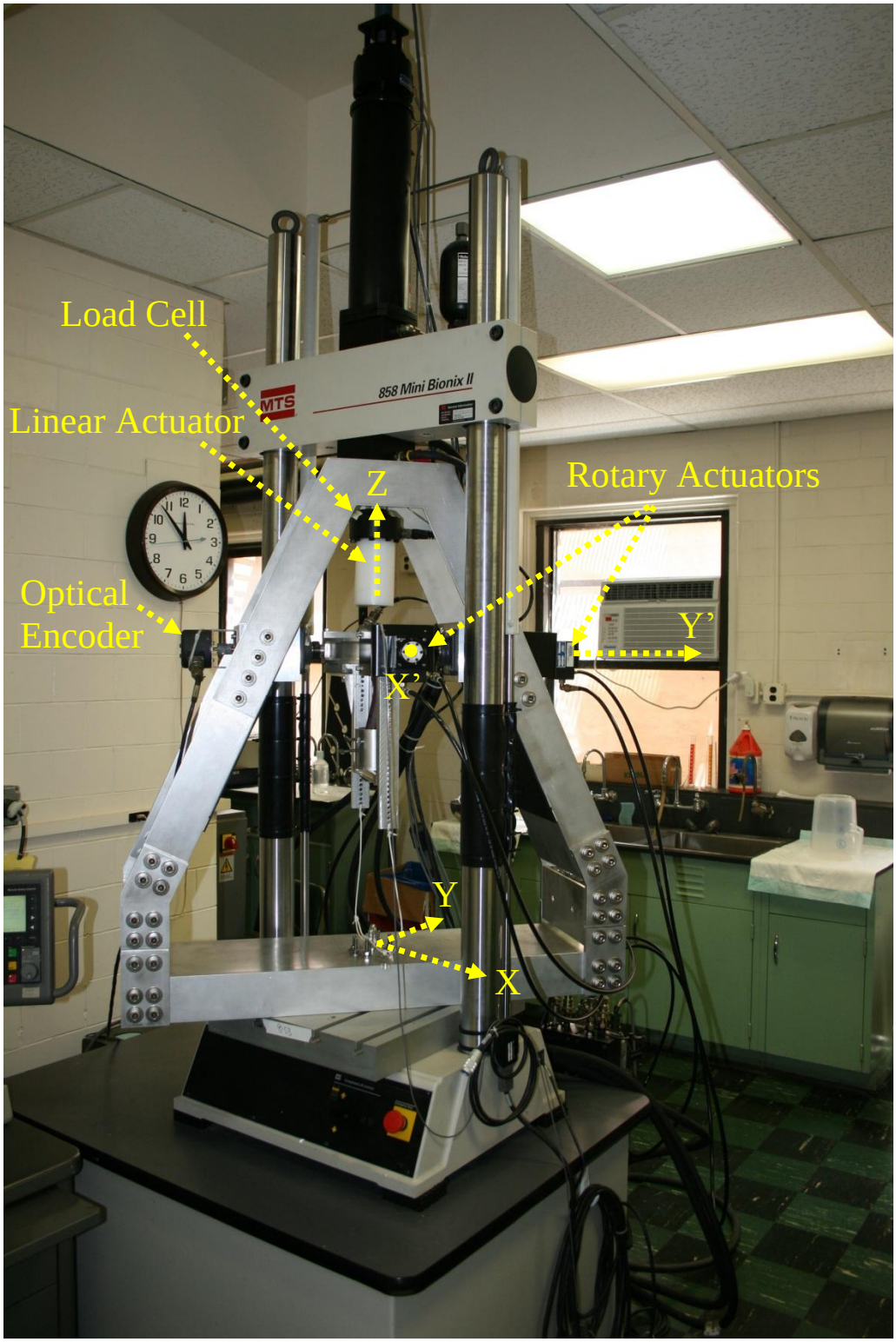

Figure B 1. Hip Simulator mounted in MTS machine.

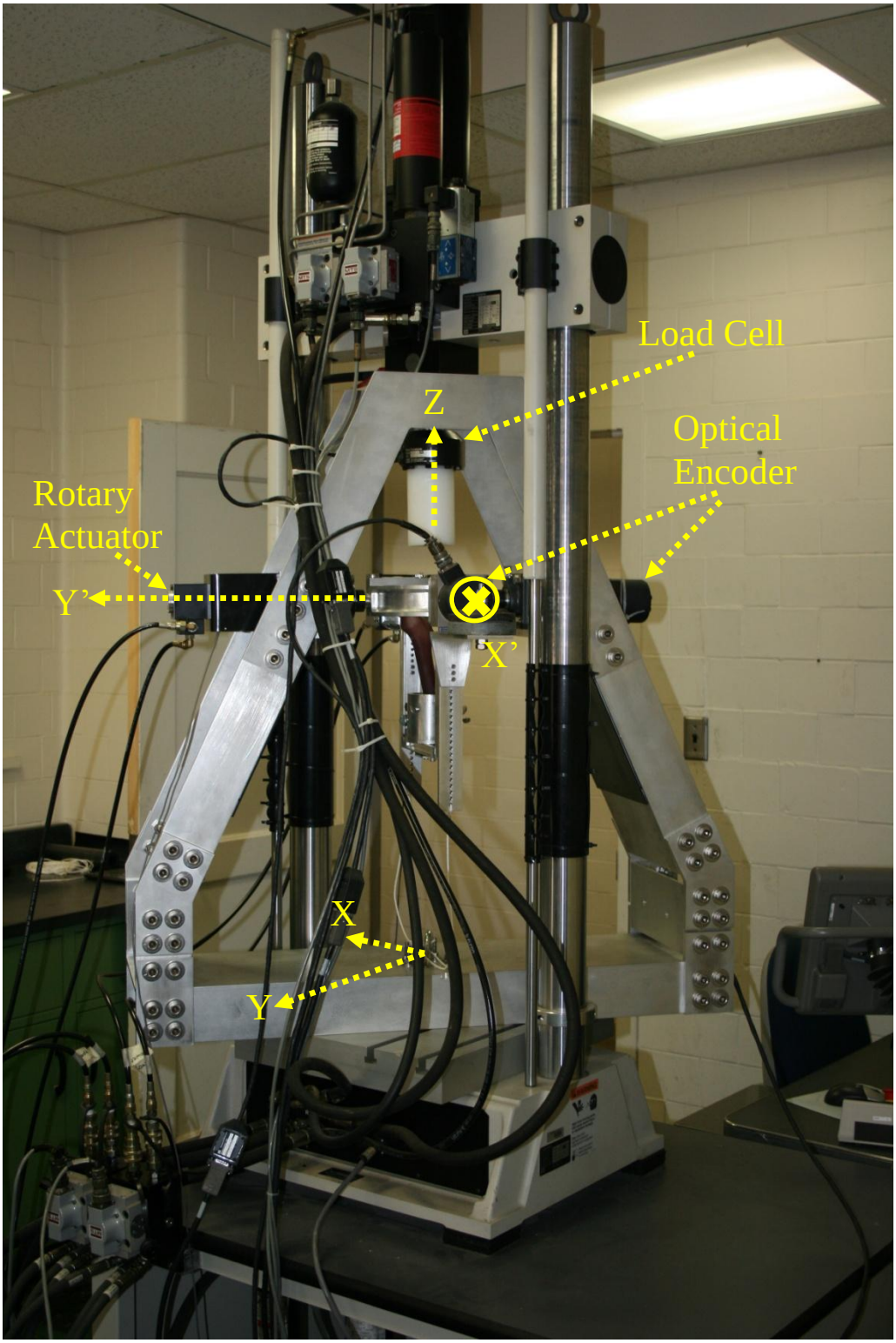

Figure B 2. Hip Simulator mounted in MTS machine.

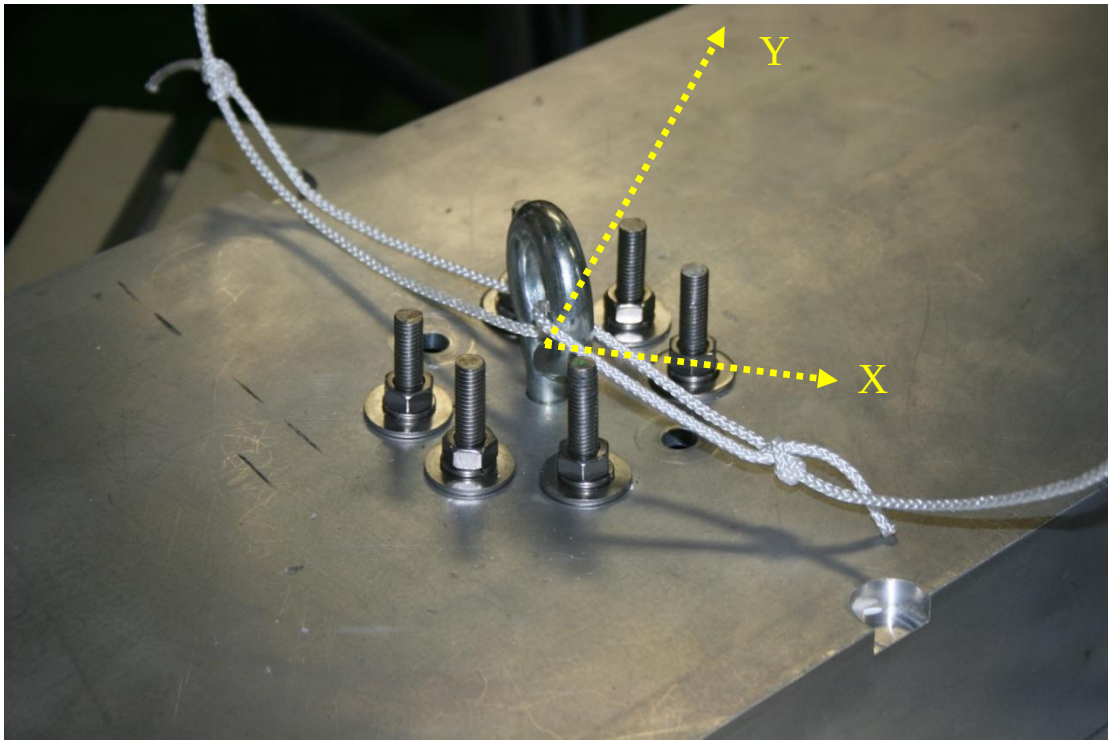

Figure B 3. **View of the DBSJFS showing the hole pattern used to connect the DBSJFS to the MTS machine and the eye bolt used during testing to tether the pendulum as a safety precaution.**

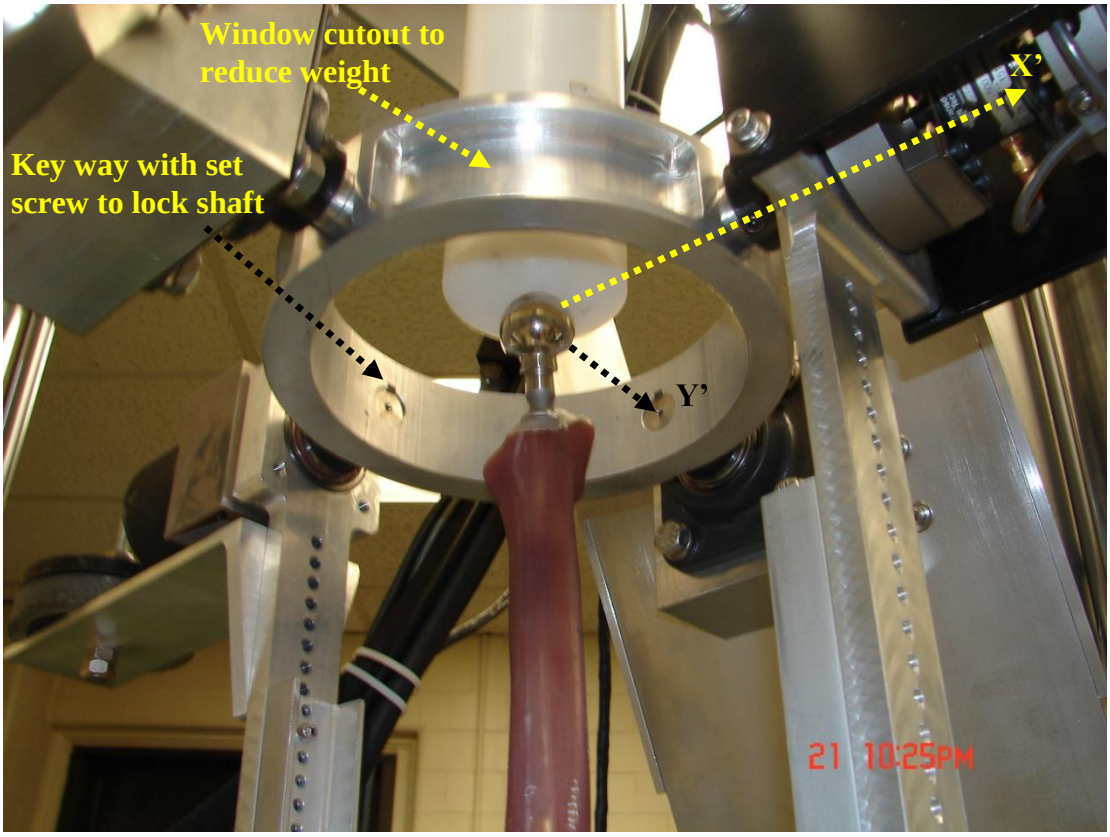

Figure B 4. View of the ring assembly.

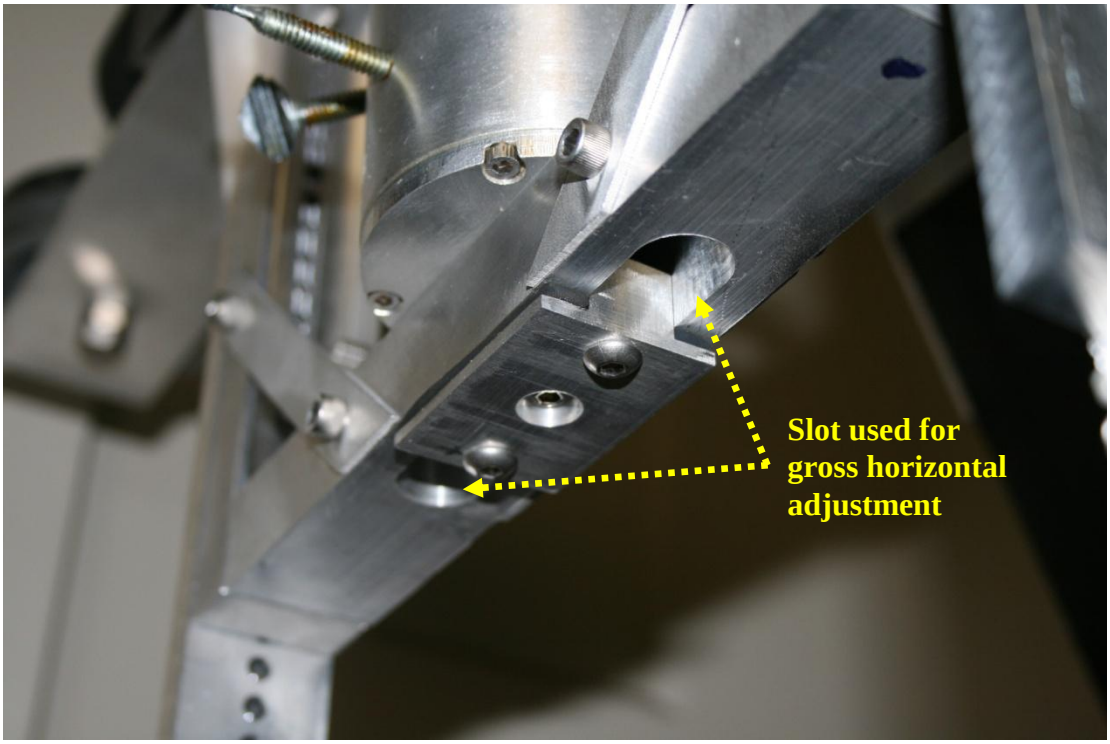

Figure B 5. Bottom view of the pendulum assembly.

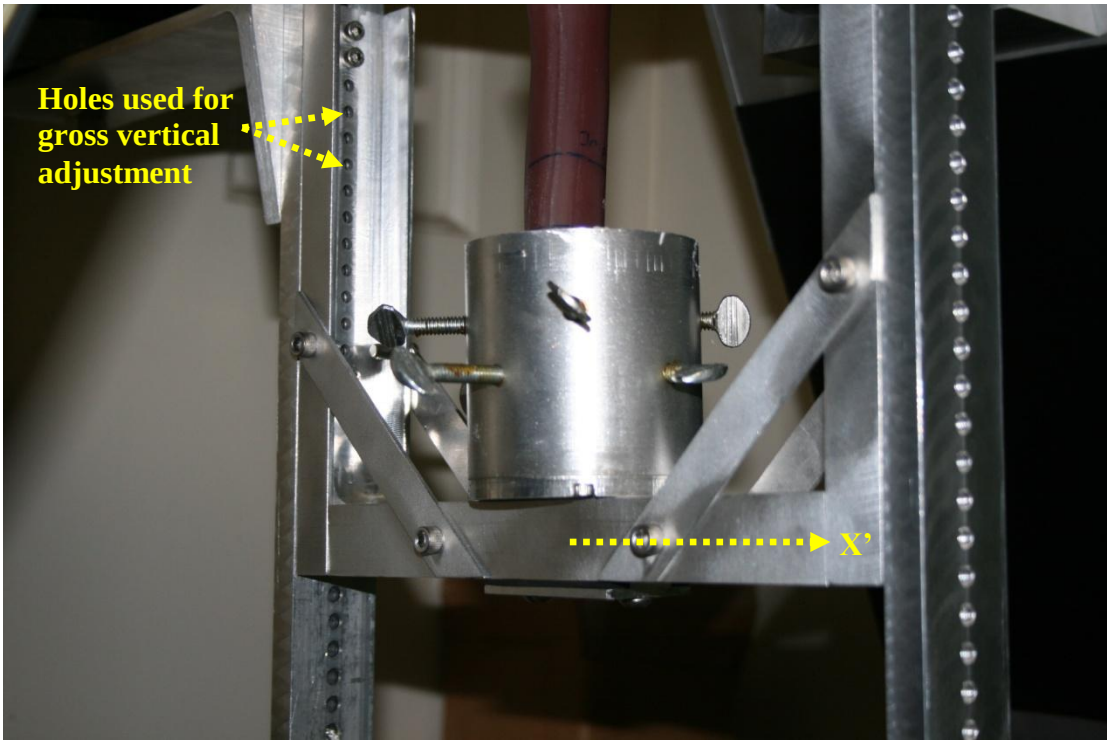

Figure B 6. Photos of the assembled pendulum with the potted femur.

APPENDIX C

Sample Calculations

C.1. Frame Deflection

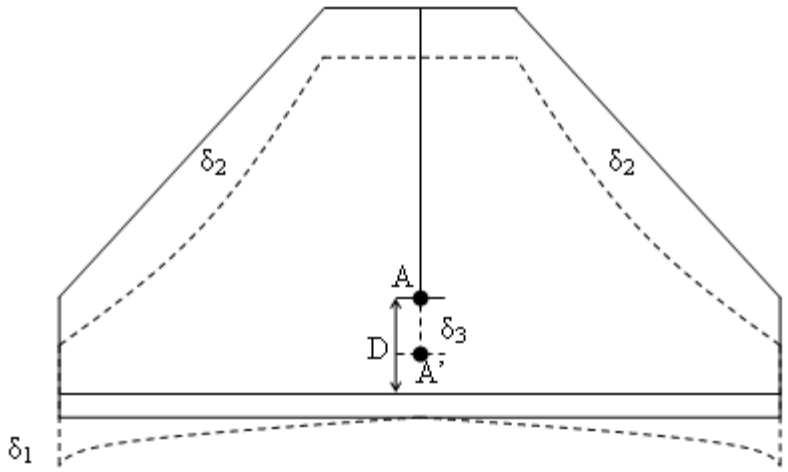

Figure C 1. Drawing of hip simulator showing exaggerated induced deflection under loading.

Total Induced Displacement at Point (A)

Eq. 1 $D = FS * \delta_{Total} = 2*0.0336 \text{ in} = 0.0672 \text{ in}$

D = displacement at point A in Figure C 1

FS = factor of safety = 2

Eq. 2 $\delta_{Total} = \delta_1 + \delta_2 + \delta_3 = 0.0299 \text{ in} + 0.0004 \text{ in} + 0.0033 \text{ in} = 0.0336 \text{ in}$

δ_1 = Flexural Deflection of the Beam (Eq. 3)

δ_2 = Axial Compressive Deflection of the Frame (Eq. 5)

δ_3 = Elongation of the pendulum (Eq. 6)

Flexural Deflection of the Beam, δ_1

Eq. 3 $$\delta_{1-\max} = \frac{P_{\max} L^3}{48 E_{Al} I} = \frac{(1{,}000\ \text{lbs})(40\ \text{in})^3}{(48)(10{,}000{,}000\ \text{psi})(4.46\text{in}^2)} = 0.0299\text{in}$$

P_{max} = maximum load = 1,000 lbs

L = length of aluminum channel = 40 in

E = elastic modulus of aluminum = 10,000,000 psi

I = moment of inertia for the aluminum beam = 4.46 in^2

Moment of Inertia Calculation, I

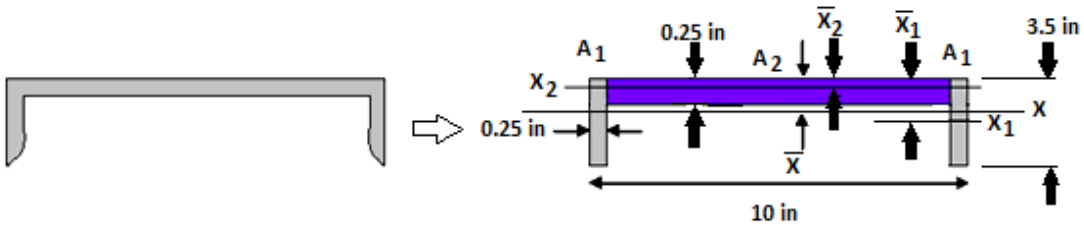

Figure C 2. Cross section of aluminum channel showing the centroid axis x. Note figure is not to scale.

Eq. 4 $$I = I_{1-x} + I_{2-x} = 4.46in^4$$

$$I_{1-x} = 2\left(I_1 + A_1(\bar{x} - \bar{x}_1)^2\right)$$

$$I_1 = \frac{1}{12} b_1 h_1^3$$

b_1 = base of A_1 = 0.25 in (Figure C 2)

h_1 = height of A_1 = 3.5 in (Figure C 2)

$$\bar{x} = \frac{2A_1\bar{x}_1 + A_2\bar{x}_2}{2A_1 + A_2} = \frac{(2)(0.875in^2)(1.75in) + (2.375in^2)(0.125in)}{(2)(0.875in^2) + 2.375in}$$

$$\bar{x} = 0.8144in$$

$$\bar{x}_1 = 1.75in$$

$$\bar{x}_2 = 0.125in$$

Area 1 (A_1) = (3.5 in)(0.25 in) = 0.875 in

Area 2 (A_2) = (9.5 in)(0.25) = 2.375 in

$$I_{2-x} = I_2 + A_2(\bar{x} - \bar{x}_2)^2$$

$$I_2 = \frac{1}{12}b_2h_2^3$$

b_2 = base of A_2 = 9.5 in (Figure C 2)

h_2 = height of A_2 = 0.25 in (Figure C 2)

$$I = 2\left(I_1 + A_1(\bar{x} - \bar{x}_1)^2\right) + I_2 + A_2(\bar{x} - \bar{x}_2)^2$$

$$I = 2\left(\frac{1}{12}b_1h_1^3 + A_1(\bar{x} - \bar{x}_1)^2\right) + \frac{1}{12}b_2h_2^3 + A_2(\bar{x} - \bar{x}_2)^2$$

$$I = 2\left(\frac{1}{12}(0.25in)(3.5in)^3 + (0.875in^2)(0.8144in - 1.75in)^2\right) + \frac{1}{12}(9.5in)(0.25in)^3 + (2.375in^2)(0.8144in - 0.125in)^2$$

$$I = 4.46in^4$$

Axial Compressive Deflection of the Frame, δ_2

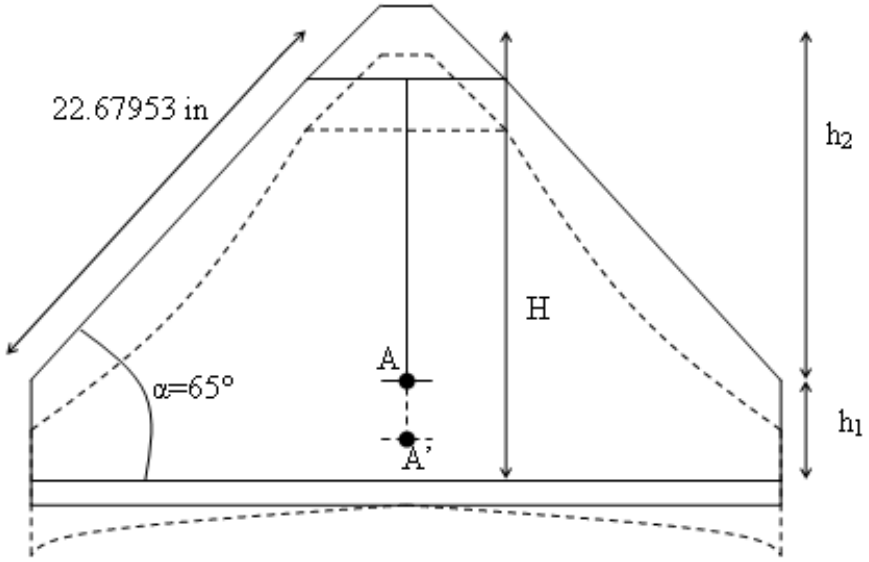

Figure C 3. Drawing of hip simulator showing exaggerated induced deflection under loading and lengths of members in axial compression.

Eq. 5 $$\delta_{2-\max} = \frac{P_{\max} L}{A E_{Al}} = \frac{PH}{2(2A_1 + A_2)E} = 0.0004 \text{ in}$$

P_{max} = maximum applied load = 1,000 lbs

L = H = $h_1 + h_2$ = 5.44 + (22.67)*sin (65°) = 26.00 in → 30 in

A = cross sectional area of both frame members angled at 65°

E = modulus of elasticity of aluminum = 10,000,000 psi

$$\delta_{2-\max} = \frac{(1{,}000 \text{ lbs})(30 \text{ in})}{(2)(2 * 0.875 in + 2.375 \text{ in}^2)(10{,}000{,}000 \text{ psi})} = 0.0004 \text{ in}$$

Elongation of the Swing, δ_3

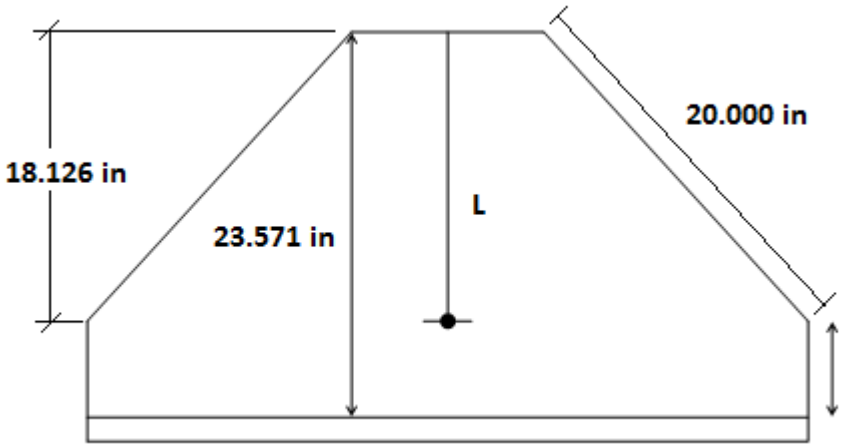

Figure C 4. Drawing of hip simulator showing the maximum distance from the base mount to the X' and Y' rotational axes.

Eq. 6 $$\delta_{3-\max} = \frac{P_{\max} L}{A_p E_{Al}} = \frac{(1{,}000\,\text{lbs})(23\,\text{in})}{(0.701\,\text{in}^2)(10{,}000{,}000\,\text{psi})} = 0.0033\,\text{in}$$

P_{max} = maximum applied load = 1,000 lbs

L = maximum length of swing arms = 23in

A_p = cross sectional area of both pendulum arms = 0.701 in^2

C.2. Derivation of $\Phi_{x'}$ and $\Phi_{y'}$

The rotation of $\Phi_{x'}$ about the X' axis of the gimbal (Figure B 4) is defined as:

$$r_{x'} = \begin{pmatrix} 1 & 0 & 0 \\ 0 & \cos(\Phi_{x'}) & -\sin(\Phi_{x'}) \\ 0 & \sin(\Phi_{x'}) & \cos(\Phi_{x'}) \end{pmatrix}$$

The rotation of $\Phi_{y'}$ about the Y' axis of the gimbal (Figure B 4) is defined as:

$$r_{y'} = \begin{pmatrix} \cos(\Phi_{y'}) & 0 & \sin(\Phi_{y'}) \\ 0 & 1 & 0 \\ -\sin(\Phi_{y'}) & 0 & \cos(\Phi_{y'}) \end{pmatrix}$$

The rotation of Φ_z about the Z axis (Figure B 1) is defined as:

$$r_z = \begin{pmatrix} \cos(\Phi_z) & -\sin(\Phi_z) & 0 \\ \sin(\Phi_z) & \cos(\Phi_z) & 0 \\ 0 & 0 & 1 \end{pmatrix}$$

The rotational matrix, R, is the product of $r_{x'}$, $r_{y'}$, and r_z. However, matrix multiplication does not commute; therefore, the order by which the axes are rotated does affect the result. The matrices should be multiplied in the opposite order of rotation. For the DBSJFS, $R = r_{x'} r_{y'} r_z$.

To find $\Phi_{x'}$ and $\Phi_{y'}$, Eq. 7 was set up. R, the rotational matrix, was multiplied by F_1, a matrix comprising of the in vivo force data from one time segment of a given activity out from the HIP98 study. The product of these two matrices produces F_2. The x_2 and y_2 components of F_2 always have a value of zero, and the z_2

component is always equal to the result force of (x_1, y_1, z_1). This is true because the actuator can only load the femoral head along the Z axis of the MTS machine. Eq. 7 was solved for each data point for each activity so that input profiles could be produced. The full derivation of $\Phi_{x'}$ and $\Phi_{y'}$ is given below:

Eq. 7 $F_2 = RF_1$

$$\begin{pmatrix} x_2 \\ y_2 \\ z_2 \end{pmatrix} = r_{x'} r_{y'} r_z \begin{pmatrix} x_1 \\ y_1 \\ z_1 \end{pmatrix}$$

$$r_{x'} r_{y'} r_z \begin{pmatrix} x_1 \\ y_1 \\ z_1 \end{pmatrix} = \begin{pmatrix} 0 \\ 0 \\ -z_2 \end{pmatrix}$$

The transpose of $r_{x'}$, $r_{x'}^T$, multiplied by $r_{x'}$ equals the identity matrix: $r_{x'}^T r_{x'} = I$

$$r_{x'}^T r_{x'} r_{y'} r_z \begin{pmatrix} x_1 \\ y_1 \\ z_1 \end{pmatrix} = r_{x'}^T \begin{pmatrix} 0 \\ 0 \\ -z_2 \end{pmatrix}$$

$$r_{y'} r_z \begin{pmatrix} x_1 \\ y_1 \\ z_1 \end{pmatrix} = r_{x'}^T \begin{pmatrix} 0 \\ 0 \\ -z_2 \end{pmatrix}$$

$$r_{y'} r_z \begin{pmatrix} x_1 \\ y_1 \\ z_1 \end{pmatrix} = \begin{pmatrix} 1 & 0 & 0 \\ 0 & \cos(\Phi_{x'}) & \sin(\Phi_{x'}) \\ 0 & -\sin(\Phi_{x'}) & \cos(\Phi_{x'}) \end{pmatrix} \begin{pmatrix} 0 \\ 0 \\ -z_2 \end{pmatrix}$$

$$r_{y'} r_z \begin{pmatrix} x_1 \\ y_1 \\ z_1 \end{pmatrix} = \begin{pmatrix} 0 \\ -z_2 \sin(\Phi_{x'}) \\ -z_2 \cos(\Phi_{x'}) \end{pmatrix}$$

$$\begin{cases} \cos(\Phi_{y'})[x_1\cos(\Phi_z) - y_1\sin(\Phi_z)] + z_1\sin(\Phi_{y'}) = 0 \\ y_1\cos(\Phi_z) + x_1\sin(\Phi_z) = z_2\sin(\Phi_{x'}) \\ z_1\cos(\Phi_{y'}) + \sin(\Phi_{y'})[y_1\sin(\Phi_z) - x_1\cos(\Phi_z)] = z_2\cos(\Phi_{x'}) \end{cases}$$

$$\cos(\Phi_{y'})[x_1\cos(\Phi_z) - y_1\sin(\Phi_z)] = -z_1\sin(\Phi_{y'})$$

$$\frac{x_1\cos(\Phi_z) - y_1\sin(\Phi_z)}{-z_1} = \tan(\Phi_{y'})$$

$$\Phi_{y'} = \tan^{-1}\left(\frac{x_1\cos(\Phi_z) - y_1\sin(\Phi_z)}{-z_1}\right) \text{***y rotation***}$$

$$y_1\cos(\Phi_z) + x_1\sin(\Phi_z) = z_2\sin(\Phi_{x'})$$

$$\Phi_{x'} = \sin^{-1}\left(\frac{y_1\cos(\Phi_z) + x_1\sin(\Phi_z)}{z_2}\right) \text{***x rotation***}$$

C.3. Transformation Derivation to graph pendulum motion in relation to MTS coordinate system

The coordinate system of the DBSJFS is rotated 40° in the clockwise direction to the coordinate system of the MTS machine. To graph the points on the pendulum throughout the various gait cycles, the position data for each path must be transformed to be in relation to the X and Y axes of the MTS machine. Figure C 5 is a drawing with a view looking down on the MTS machine showing the relationship between these two coordinate systems. The circles represent the columns of the MTS machine.

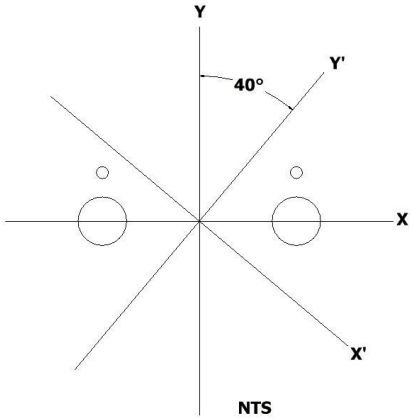

Figure C 5. Drawing showing the coordinate systems of the MTS machine (X and Y) and the DBSJFS gimbal (X' and Y').

The following diagrams in Figure C 6 and Figure C 7 help to show how the positions of P_1, P_2, P_3, and P_4 are derived.

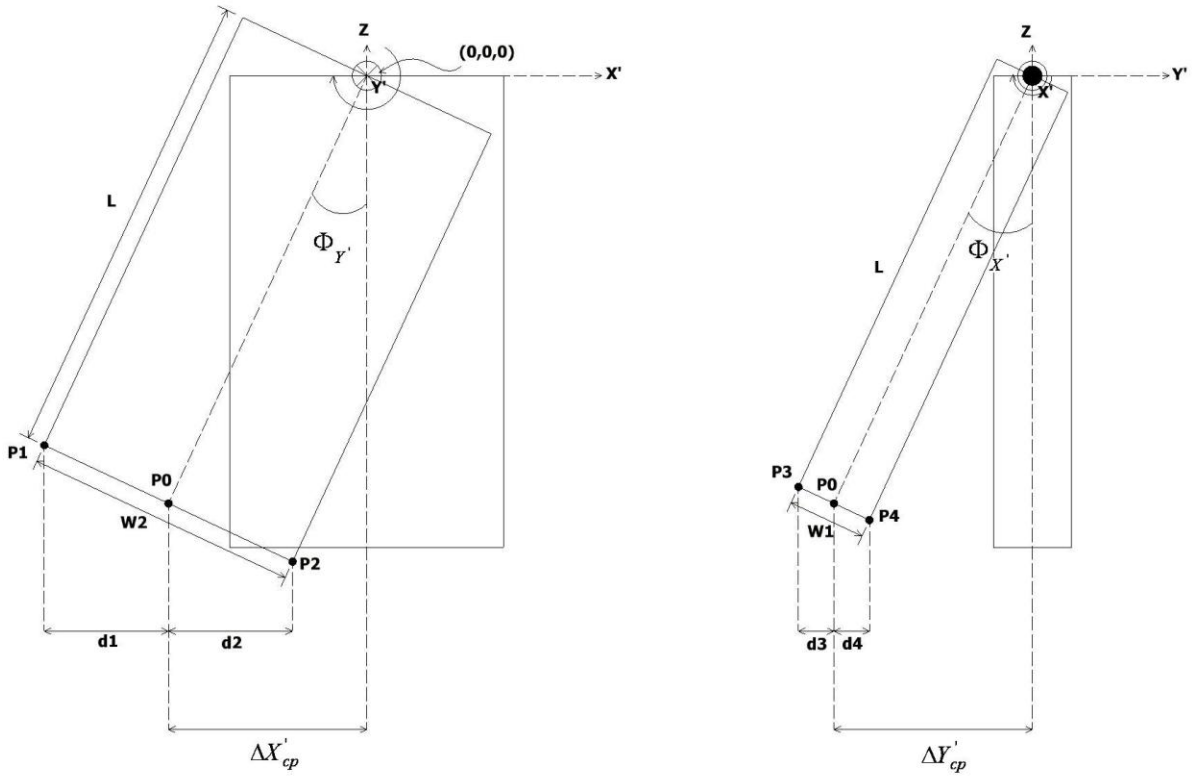

Figure C 6. Side views of the pendulum showing the points graphed in the figures of Appendix B.

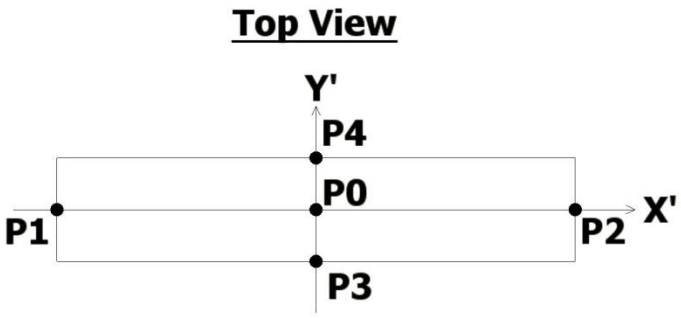

Figure C 7. Top view of pendulum depicting the points graphed in the figures of Appendix B.

$$\Delta X'_{cp} = L\sin\left(\Phi_{Y'}\right)$$
$$\Delta Y'_{cp} = L\sin\left(\Phi_{X'}\right)$$
$$\Delta Z_{X'_{cp}} = L - L\sin\left(\Phi_{X'}\right) = L\left(1-\cos\left(\Phi_{x'}\right)\right)$$
$$\Delta Z_{Y'_{cp}} = L - L\sin\left(\Phi_{Y'}\right) = L\left(1-\cos\left(\Phi_{Y'}\right)\right)$$
$$\Delta Z_{Total} = \Delta Z_{X'_{cp}} + \Delta Z_{Y'_{cp}} = L\left(2-\cos\left(\Phi_{x'}\right)-\cos\left(\Phi_{Y'}\right)\right)$$
$$d_1 = d_2 = \tfrac{1}{2} w_2 \cos\left(\Phi_{Y'}\right)$$
$$d_3 = d_4 = \tfrac{1}{2} w_1 \cos\left(\Phi_{X'}\right)$$

CoordinateEquations

$X' - coordinates$

$$P_0 = -L\sin\left(\Phi_{Y'}\right) = P_3 = P_4$$
$$P_1 = -L\sin\left(\Phi_{Y'}\right) - \tfrac{1}{2} w_2 \cos\left(\Phi_{Y'}\right)$$
$$P_2 = -L\sin\left(\Phi_{Y'}\right) + \tfrac{1}{2} w_2 \cos\left(\Phi_{Y'}\right)$$

$Y' - coordinates$

$$P_0 = L\sin\left(\Phi_{X'}\right) = P_1 = P_2$$
$$P_3 = L\sin\left(\Phi_{X'}\right) - \tfrac{1}{2} w_1 \cos\left(\Phi_{X'}\right)$$
$$P_4 = L\sin\left(\Phi_{X'}\right) + \tfrac{1}{2} w_1 \cos\left(\Phi_{X'}\right)$$

The following shows the transformation equation used to calculate the coordinates to a rotated X' and Y' axis in relation to the MTS machine X and Y coordinate system.

$$R_Z(\Phi)=\begin{pmatrix}\cos(\Phi_Z) & -\sin(\Phi_Z) & 0\\ \sin(\Phi_Z) & \cos(\Phi_Z) & 0\\ 0 & 0 & 1\end{pmatrix}$$

$$\begin{pmatrix}X_2\\ Y_2\\ Z_2\end{pmatrix}=\begin{pmatrix}\cos(\Phi_Z) & -\sin(\Phi_Z) & 0\\ \sin(\Phi_Z) & \cos(\Phi_Z) & 0\\ 0 & 0 & 1\end{pmatrix}\begin{pmatrix}X_1\\ Y_1\\ Z_1\end{pmatrix}$$

$$Z_1 = 0$$
$$Z_2 = 0$$
$$\Phi_Z = -40^\circ$$

$$\begin{pmatrix}X_2\\ Y_2\end{pmatrix}=\begin{pmatrix}\cos(\Phi_Z) & -\sin(\Phi_Z)\\ \sin(\Phi_Z) & \cos(\Phi_Z)\end{pmatrix}\begin{pmatrix}X_1\\ Y_1\end{pmatrix}$$
$$\begin{bmatrix}X_2 = X_1\cos(\Phi_Z)-Y_1\sin(\Phi_Z)\\ Y_2 = X_1\sin(\Phi_Z)+Y_1\cos(\Phi_Z)\end{bmatrix}$$

After the initial points were graphed, the columns of the MTS machine were found to interfere with parts of the desired movements in a few of the gait patterns. Therefore, the decision was made to pot right femurs at an angle of -20 degrees in relation to the X-axis and to pot left femurs at angle of +20 degree angle in relation to the Y-axis. The final step in obtaining the new projected displacements of points P_1, P_2, P_3, and P_4 on the pendulum was to manipulate X_2 and Y_2 from the equations above.

Shift down the Y - axis

$\Delta Y = L\sin(\Phi_X)$

$\Delta X = 0$

$X_3 = X_1$

$Y_3 = Y_2 + L\sin(\Phi_X)$

$+20^\circ$ for the left femur

-20° for the right femur

APPENDIX D

Average Hip Contact Forces, Pendulum Displacement, X' and Y' axes Rotations, and Gait Profiles

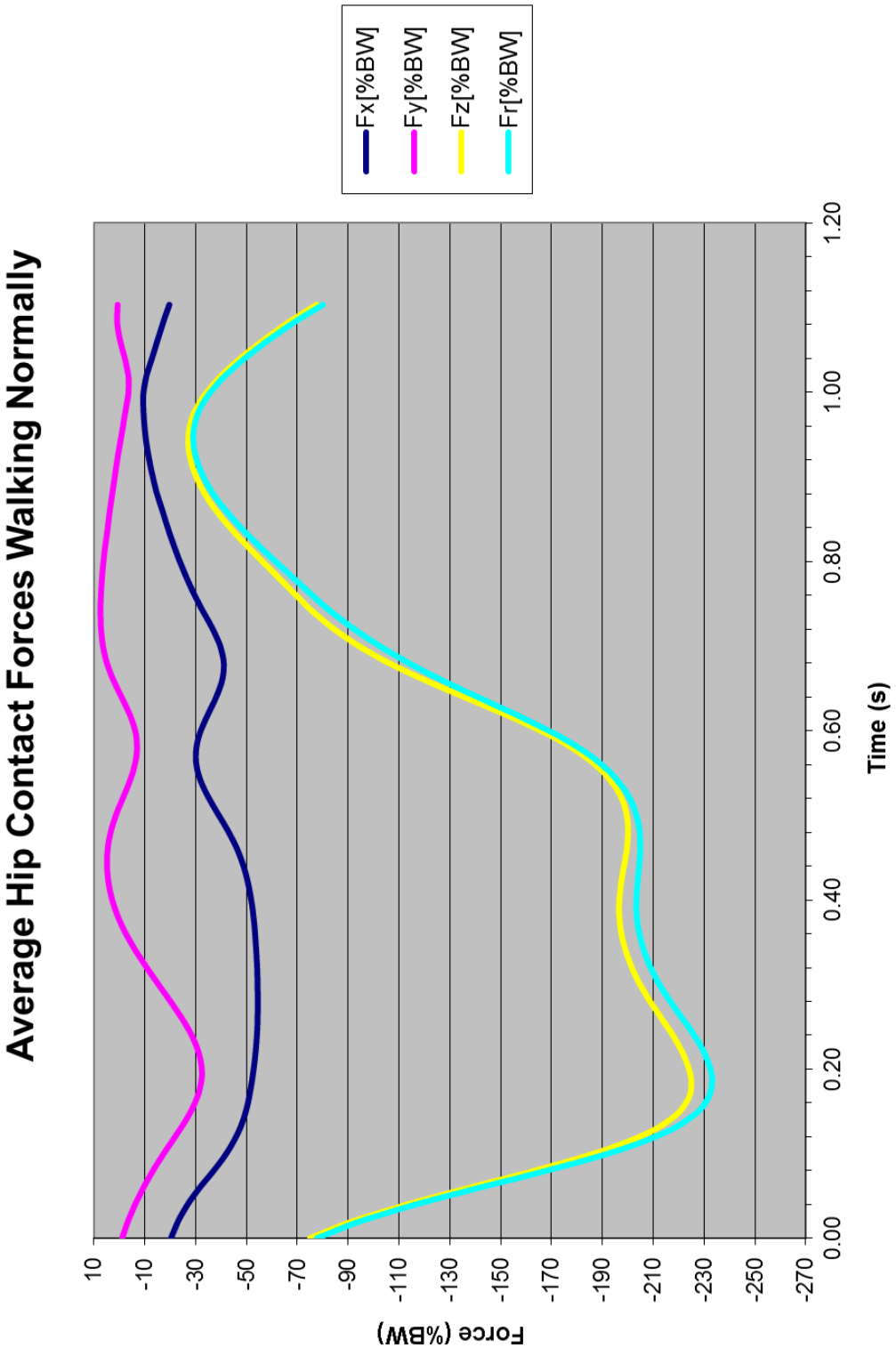

Figure D 1. Average hip contact forces walking normally.

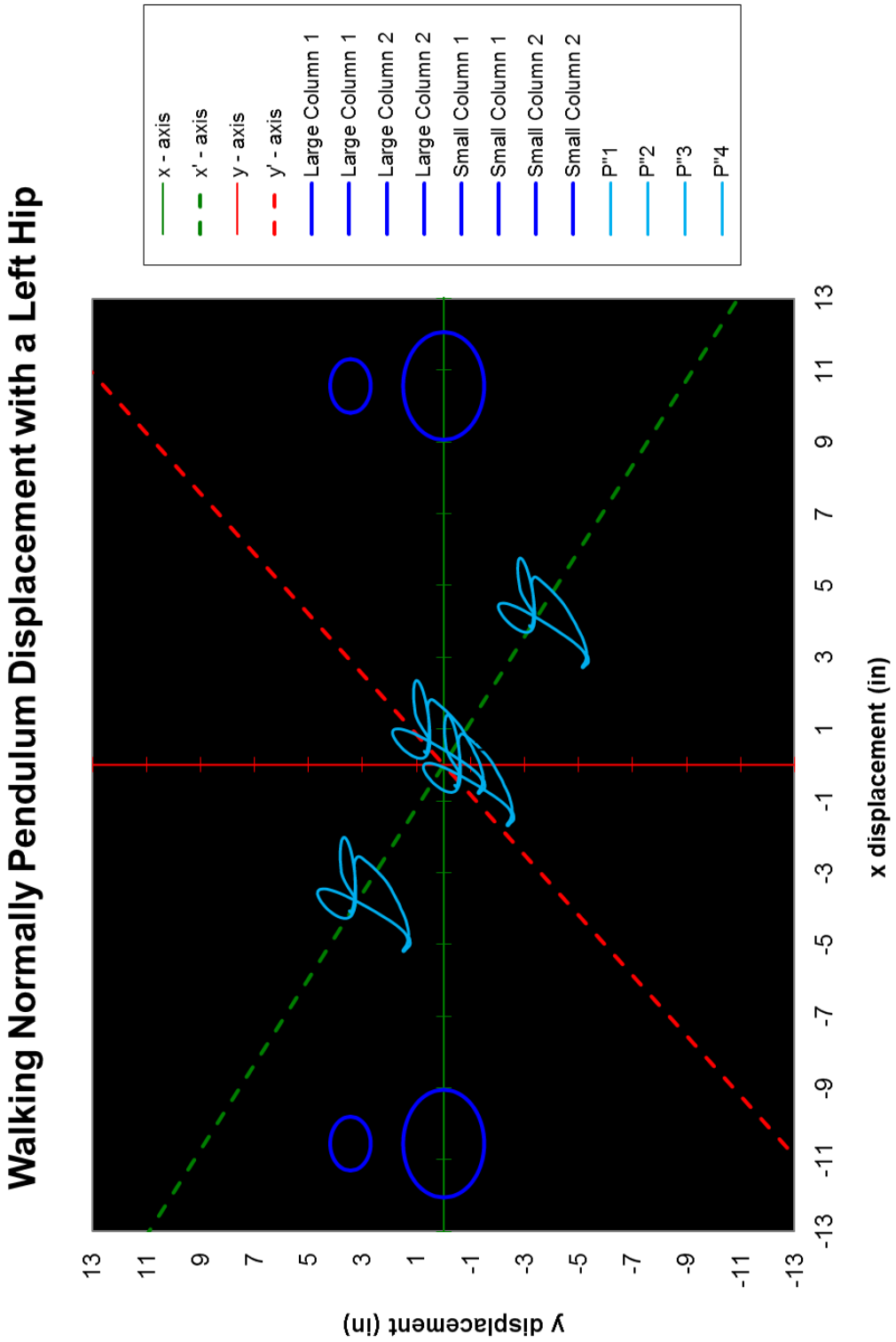

Figure D 2. Walking normally pendulum displacement with a left femur.

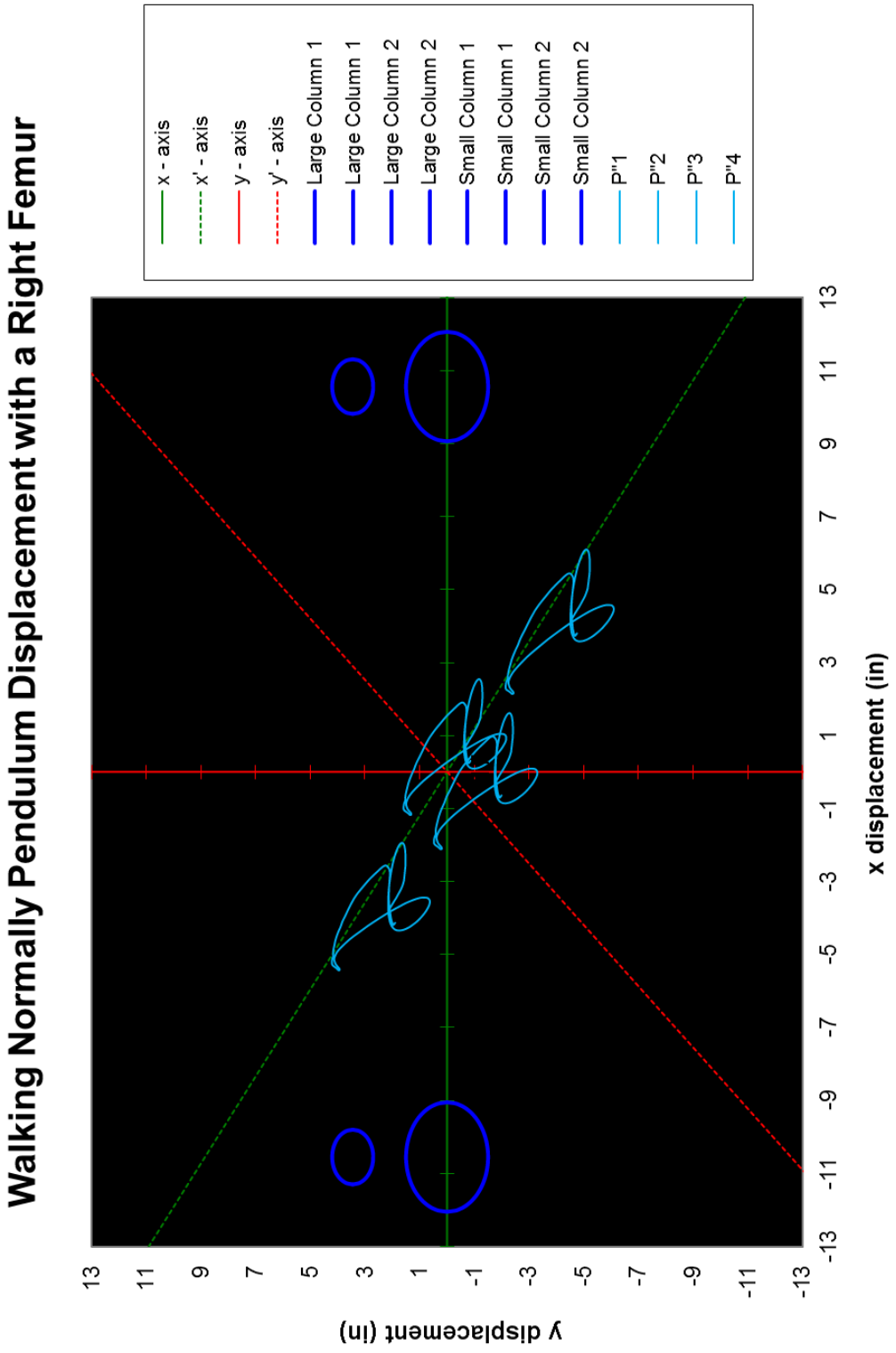

Figure D 3. Walking normally pendulum displacement with a right femur.

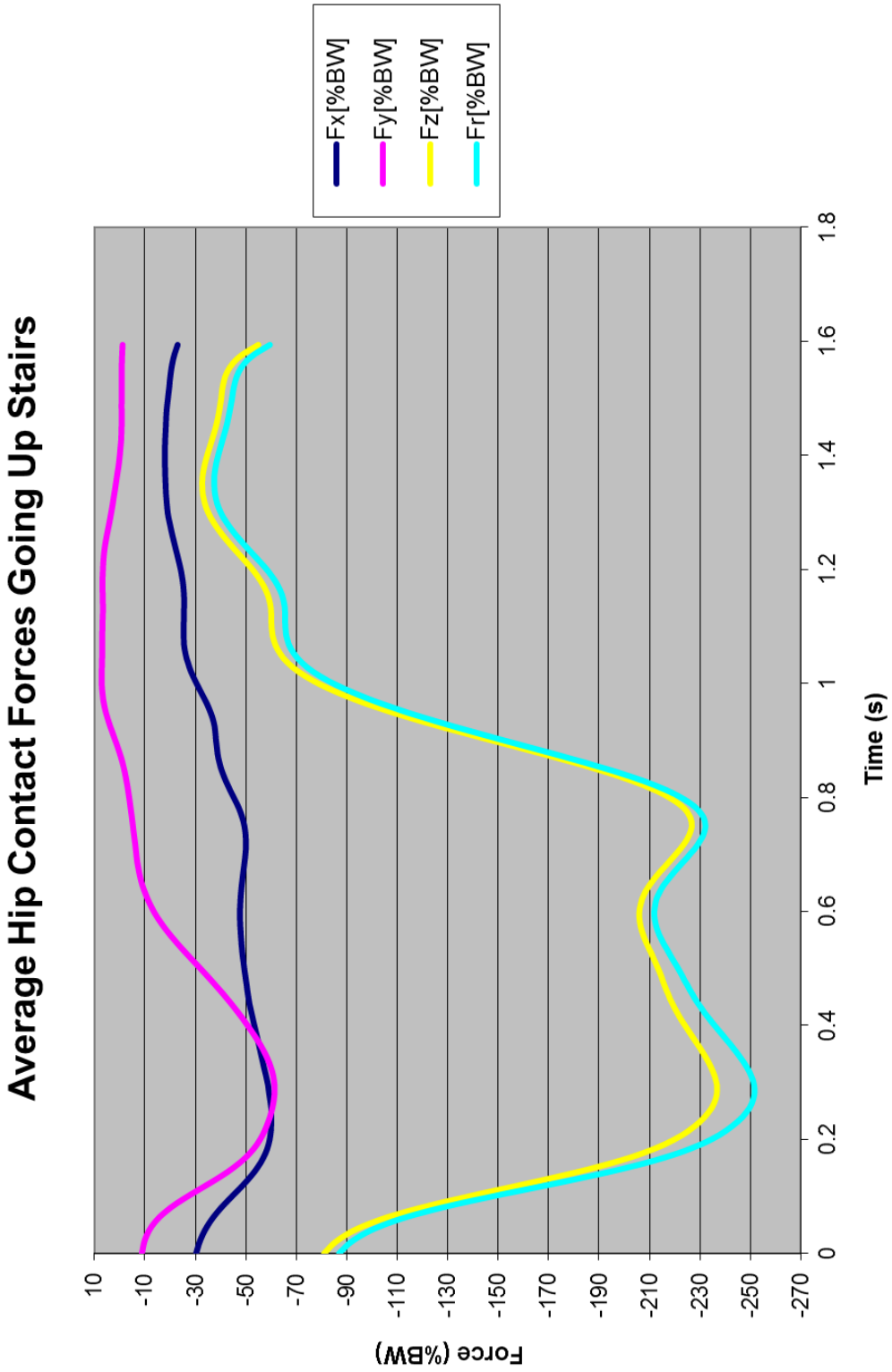

Figure D 4. Average hip contact forces going up stairs.

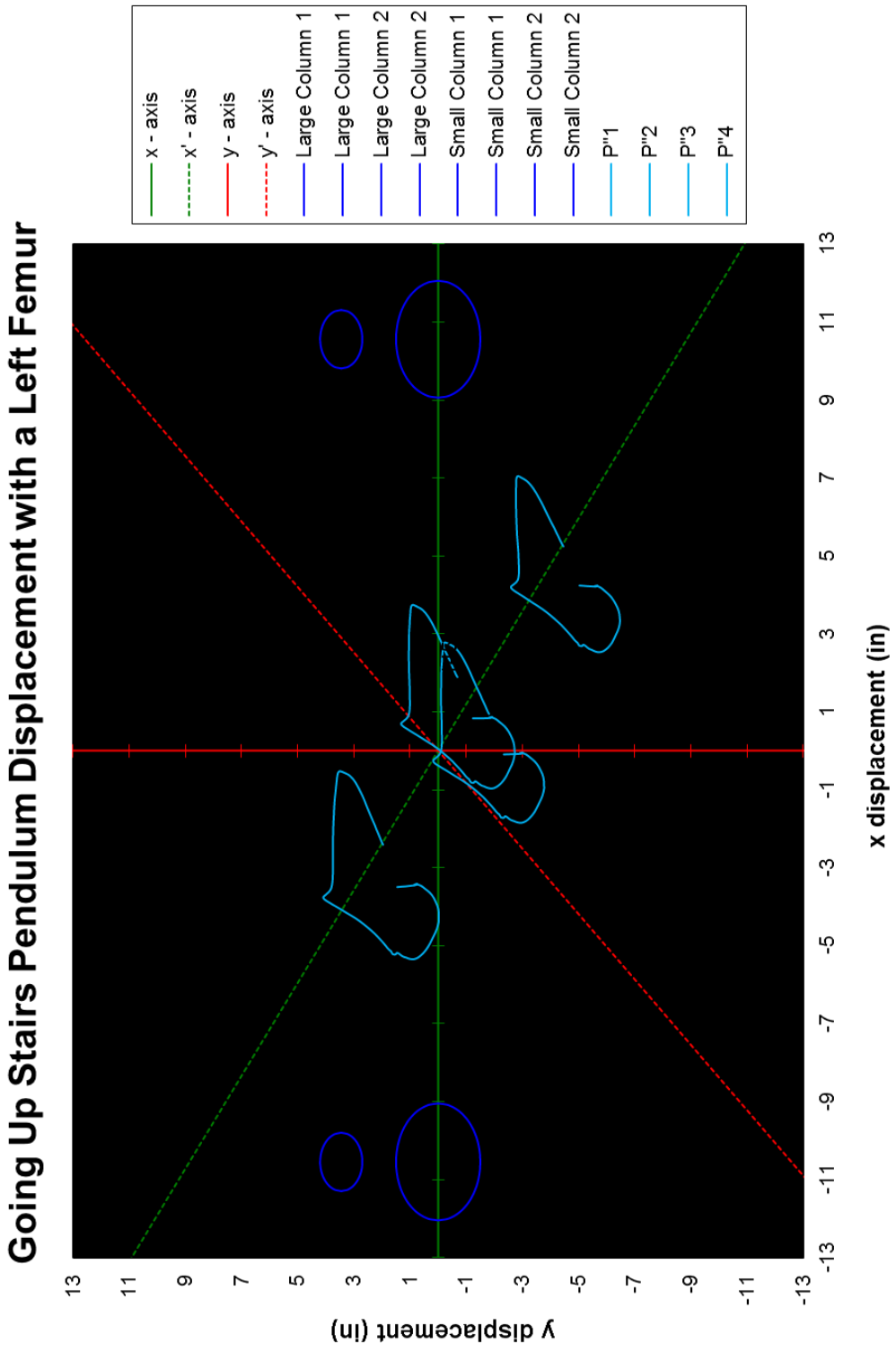

Figure D 5. Going up stairs pendulum displacement with a left femur.

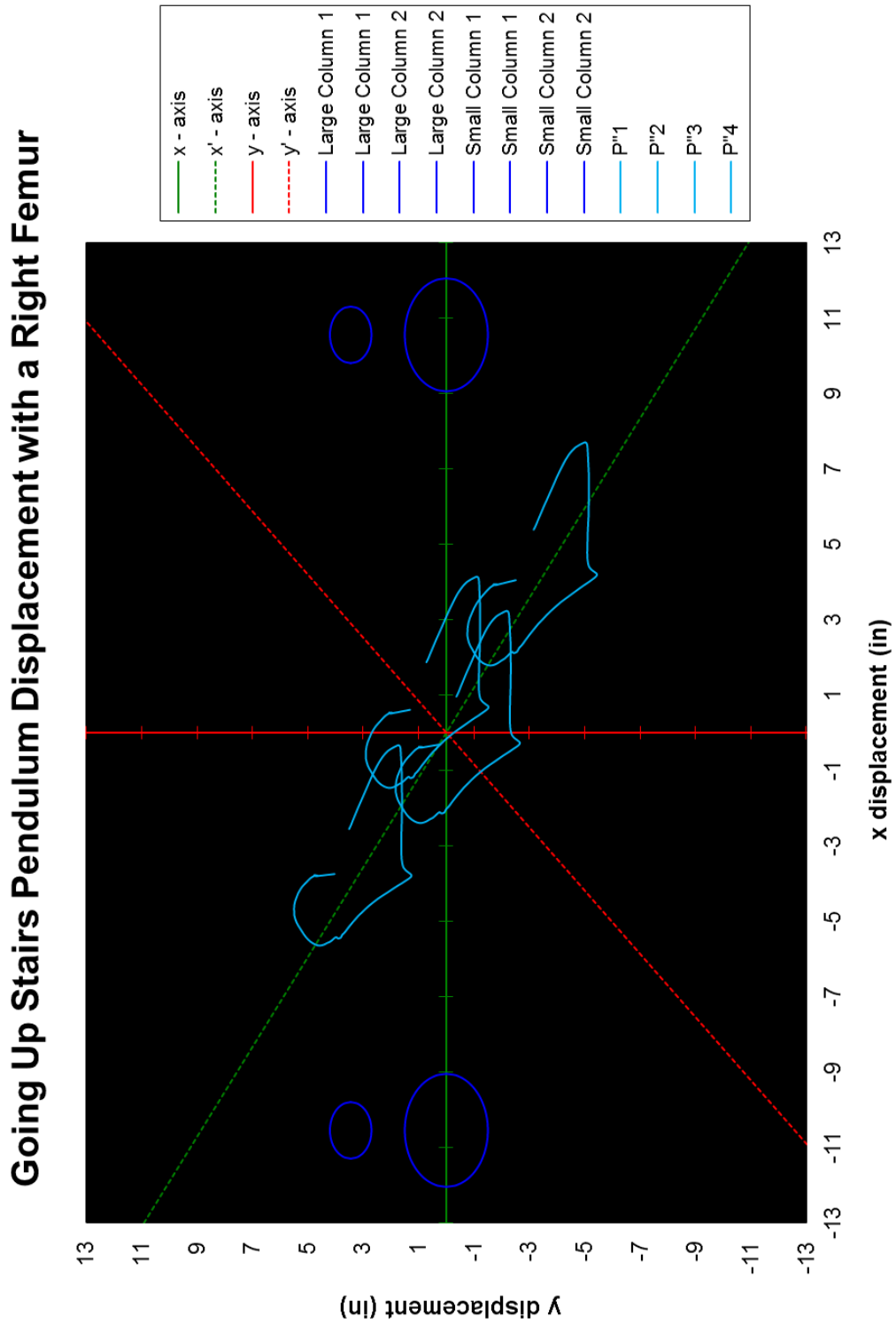

Figure D 6. Going up stairs pendulum displacement with a right femur.

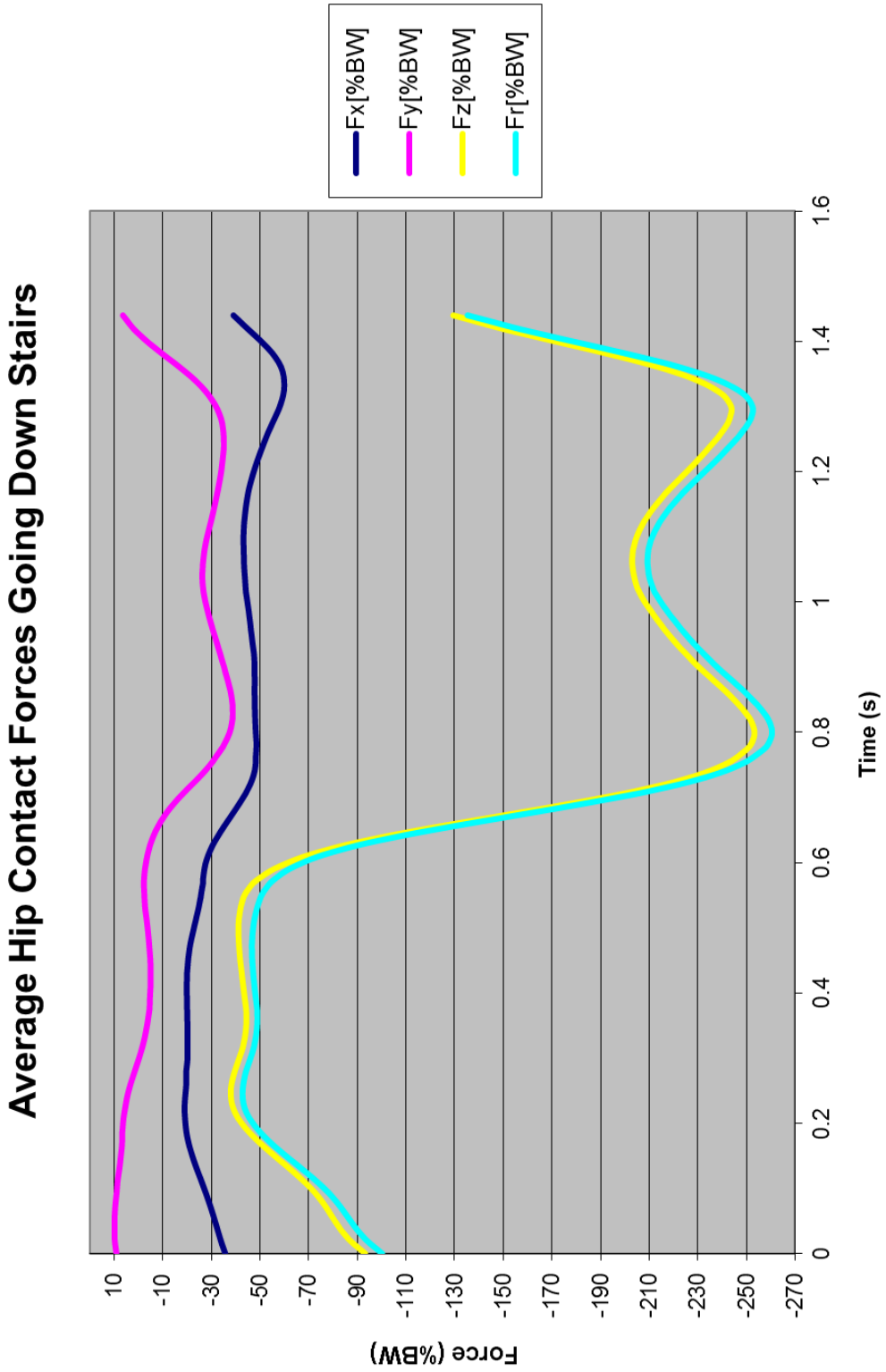

Figure D 7. Average hip contact forces going down stairs.

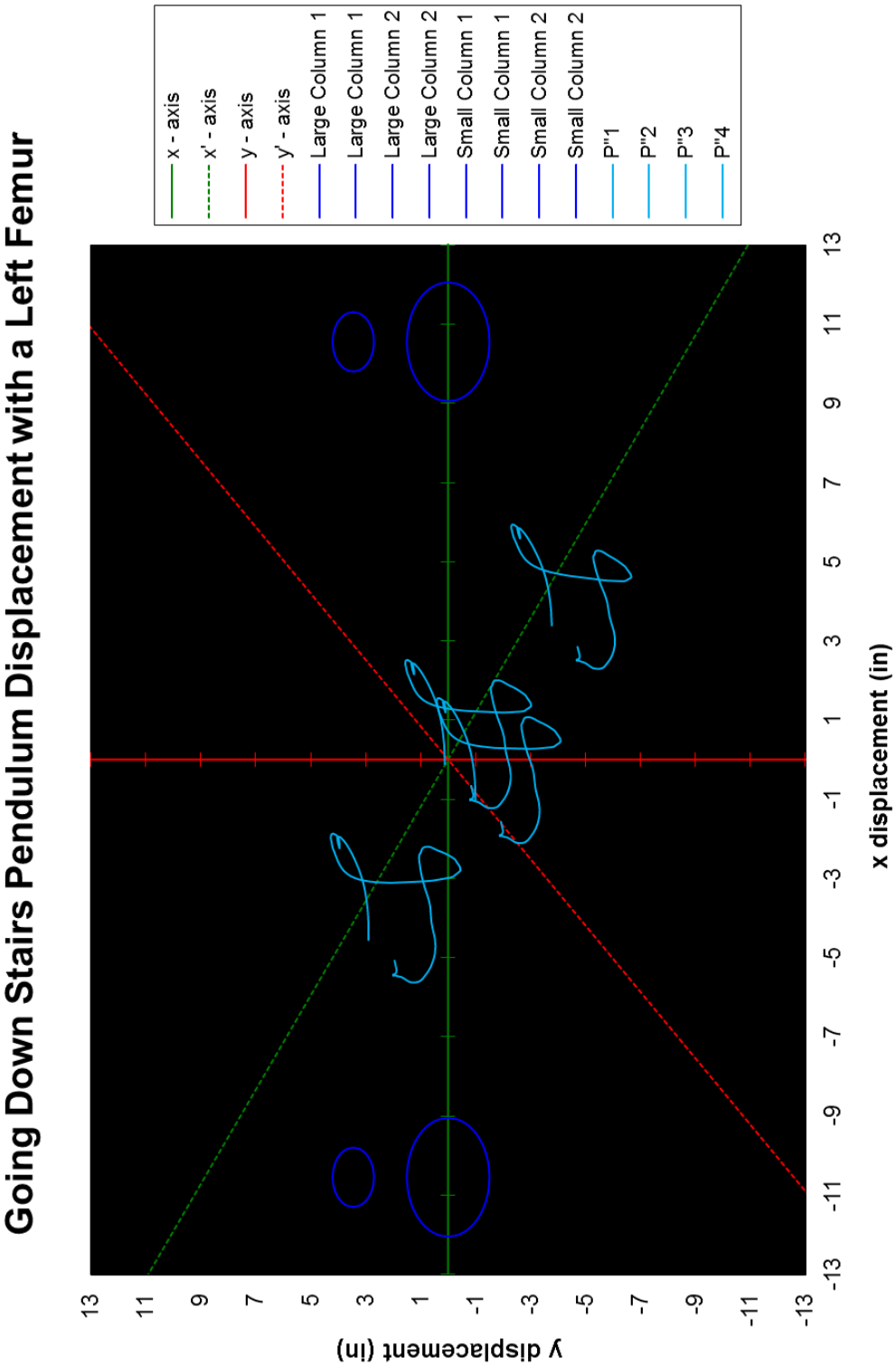

Figure D 8. Going down stairs pendulum displacement with a left femur.

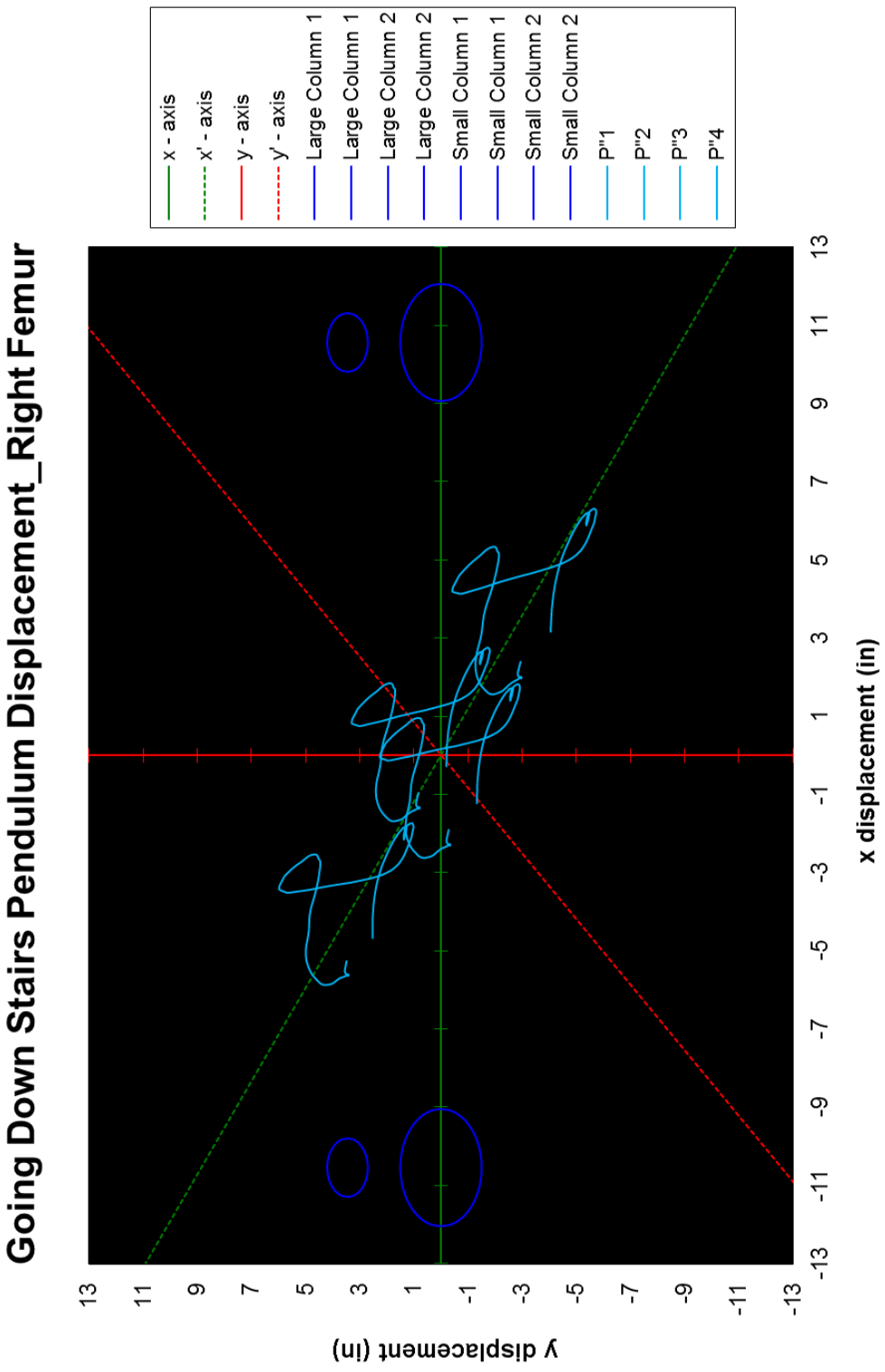

Figure D 9. Going down stairs pendulum displacement with a right femur.

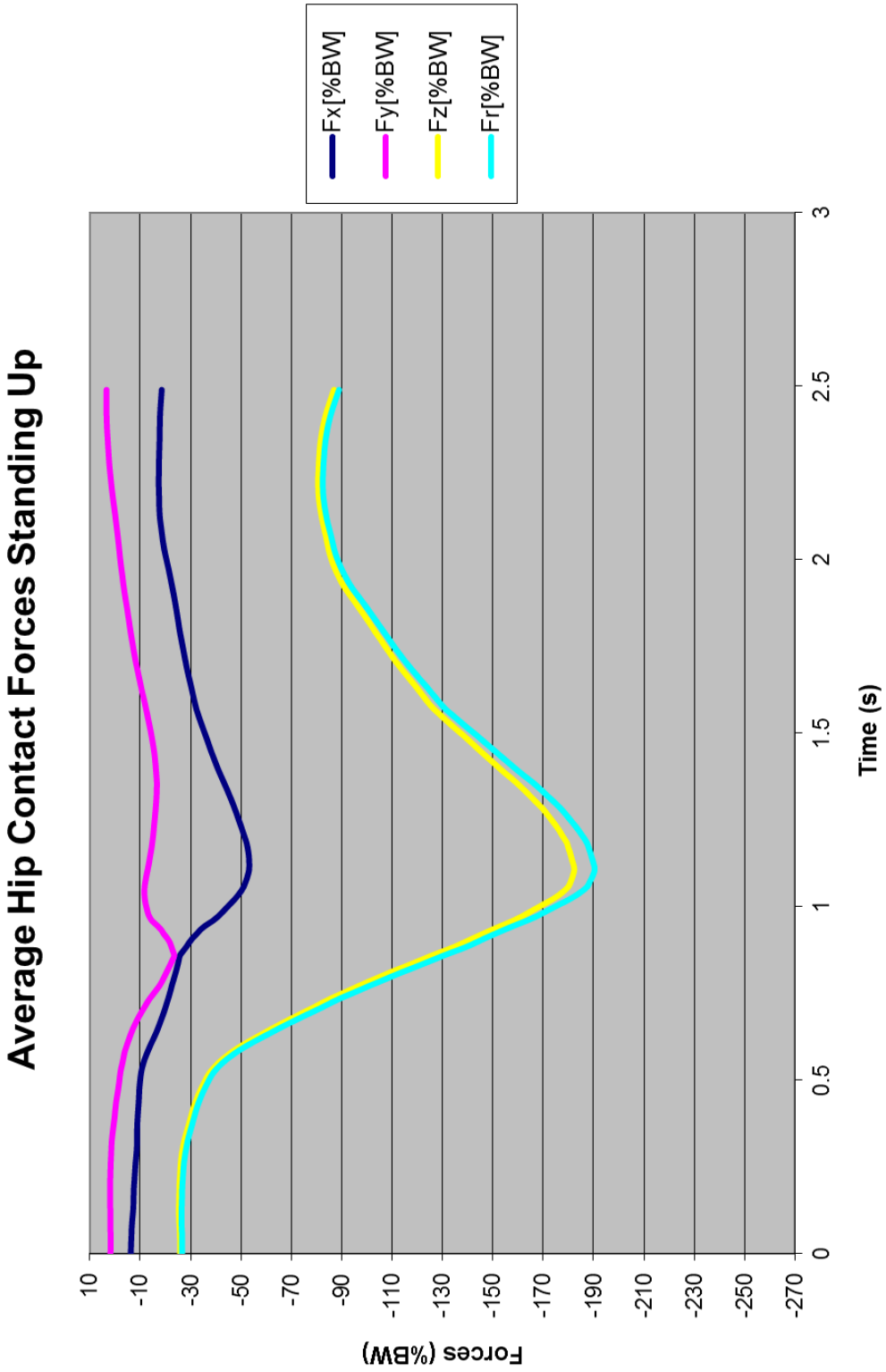

Figure D 10. Average contact forces standing up.

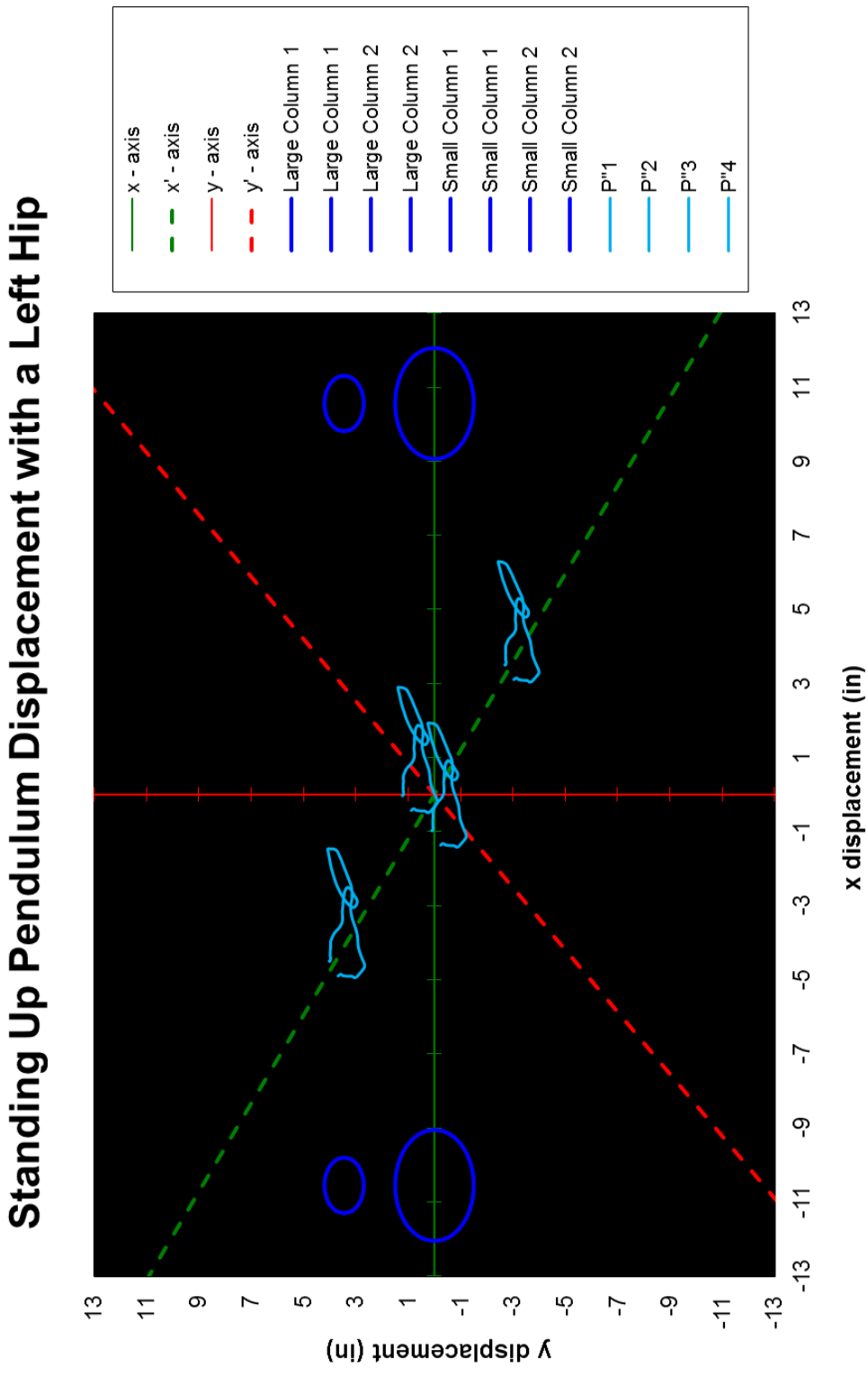

Figure D 11. Standing up Pendulum displacement with a left femur.

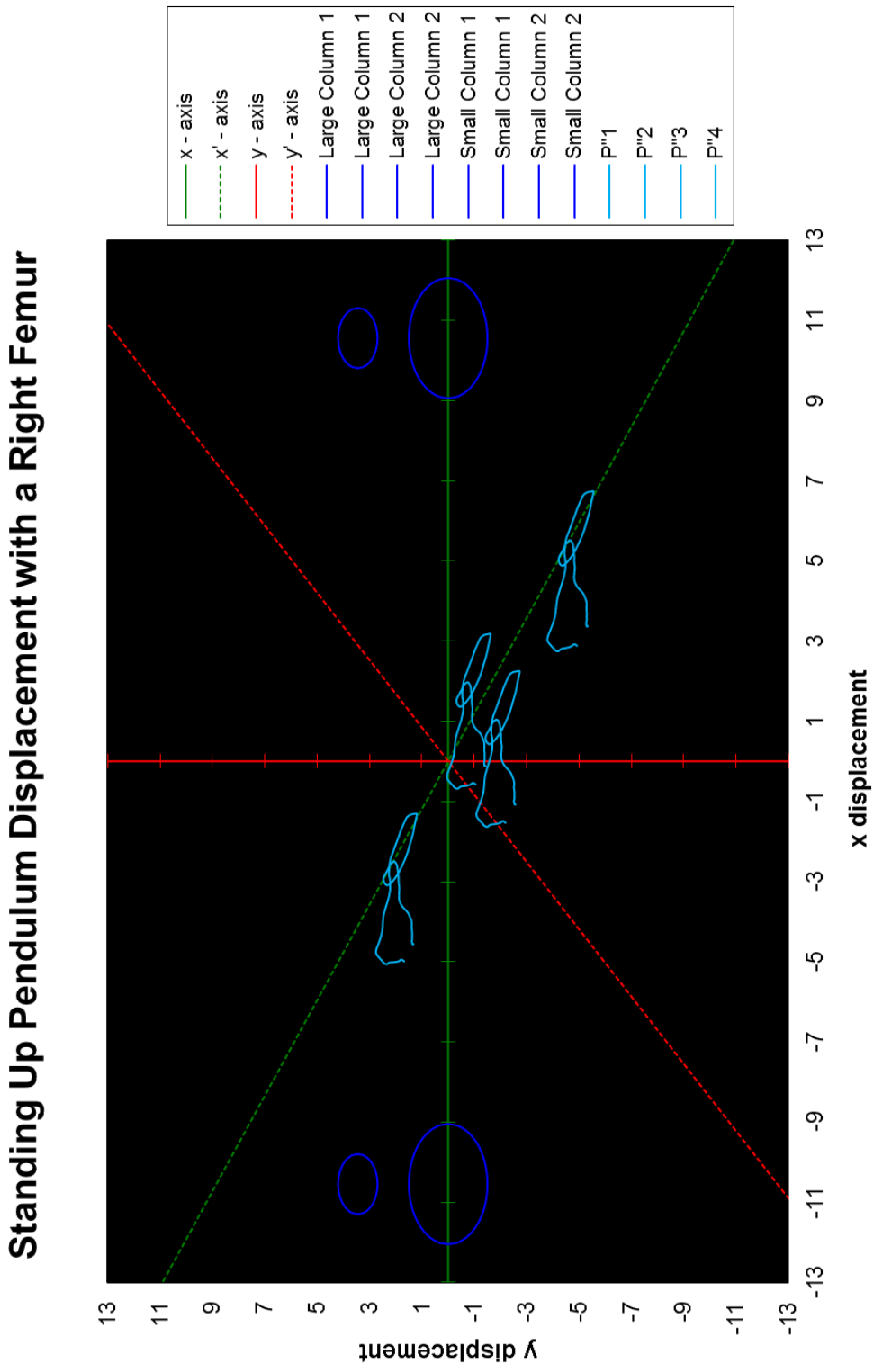

Figure D 12. Standing up pendulum displacement with a right femur.

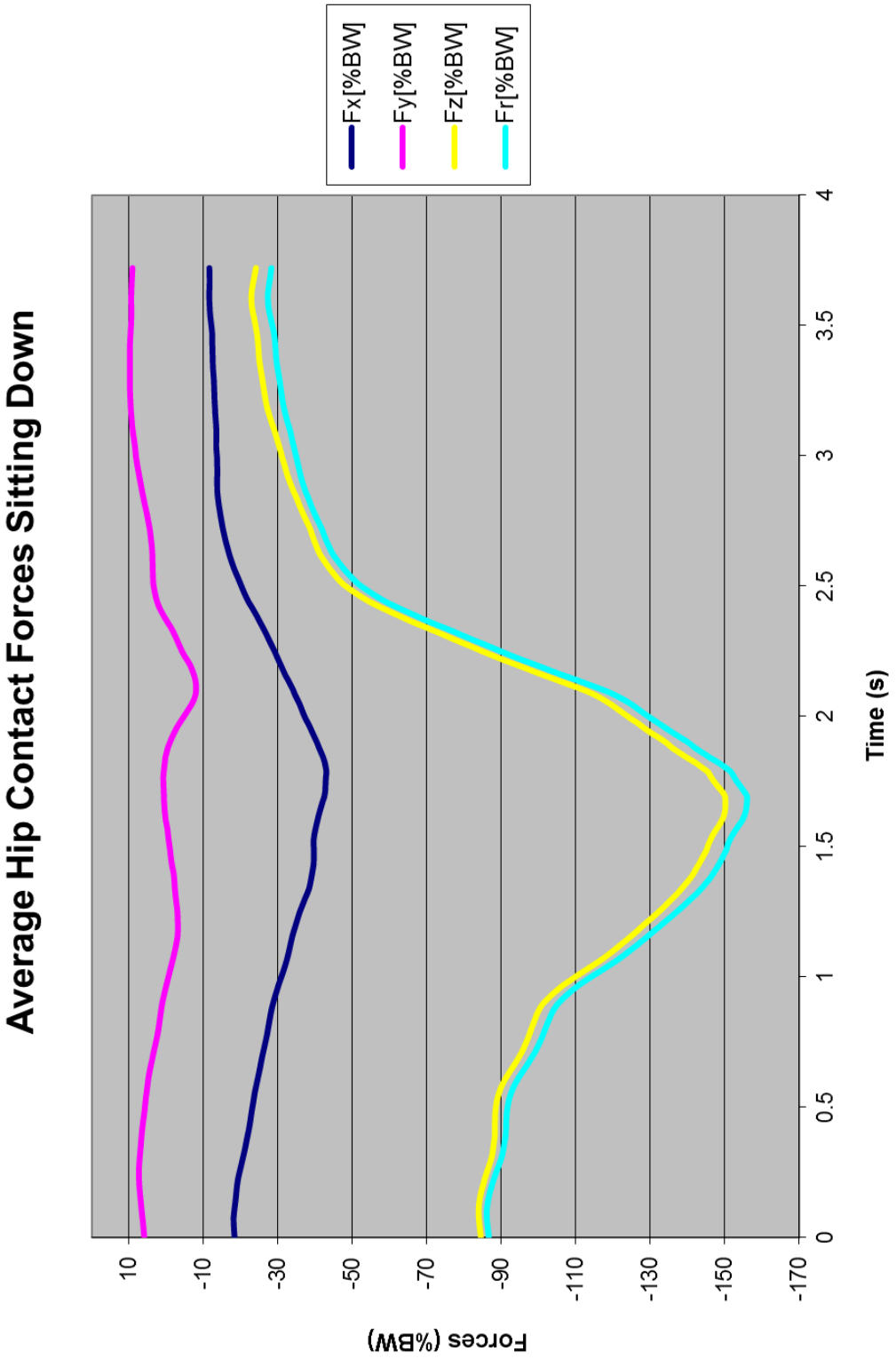

Figure D 13. Average hip contact forces sitting down.

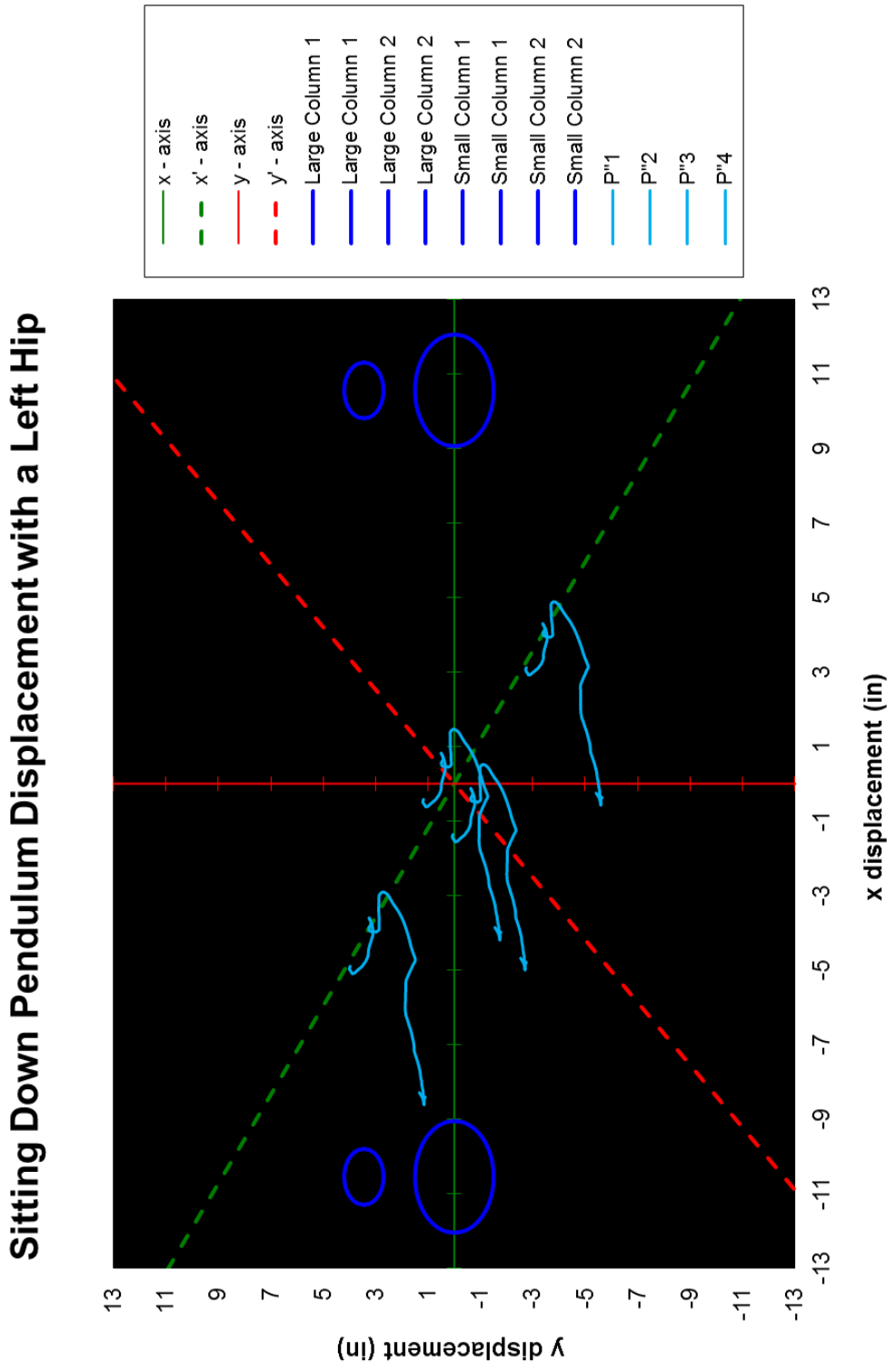

Figure D 14. Sitting down pendulum displacement with a left femur.

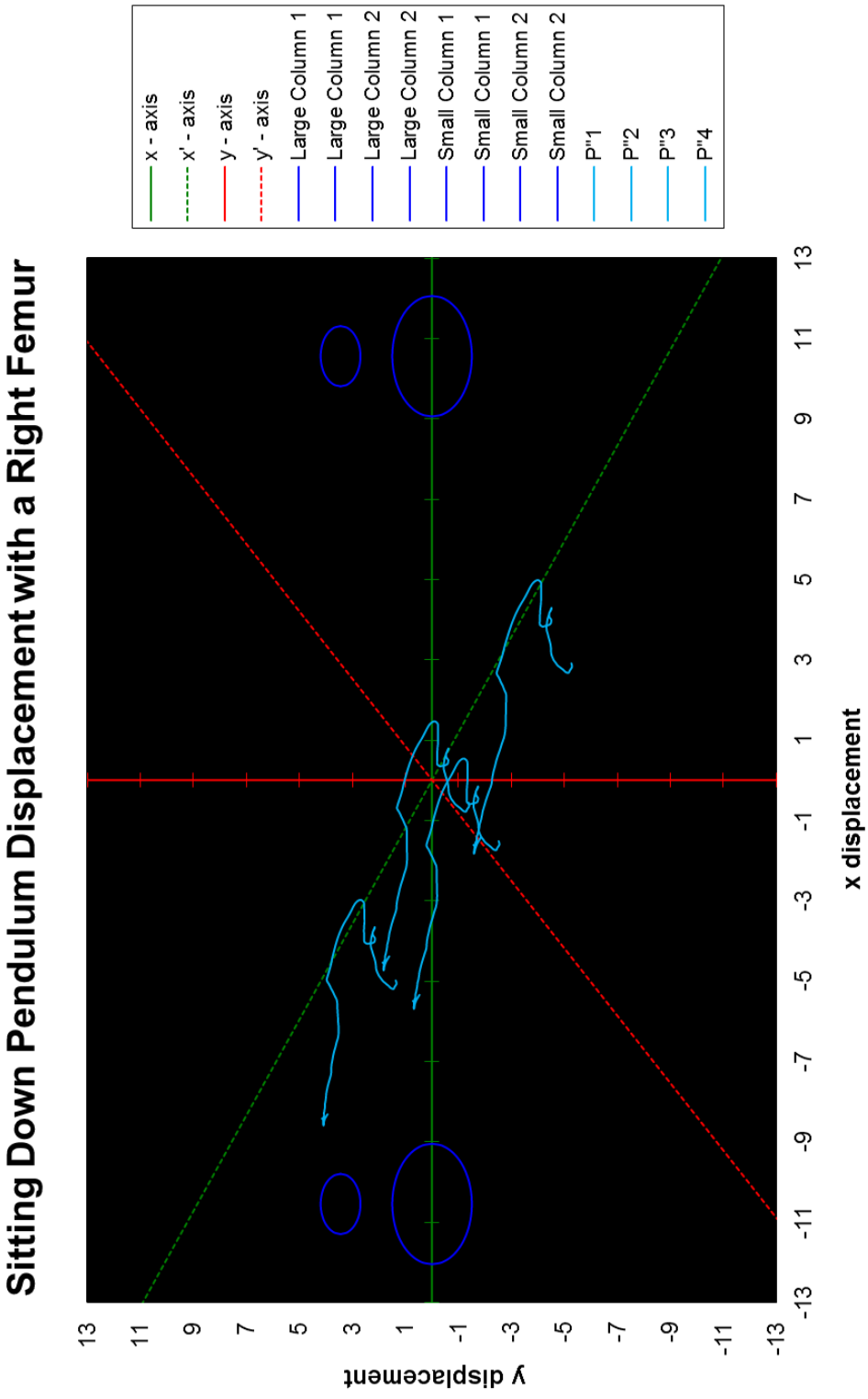

Figure D 15. Sitting down pendulum displacement with a right femur.

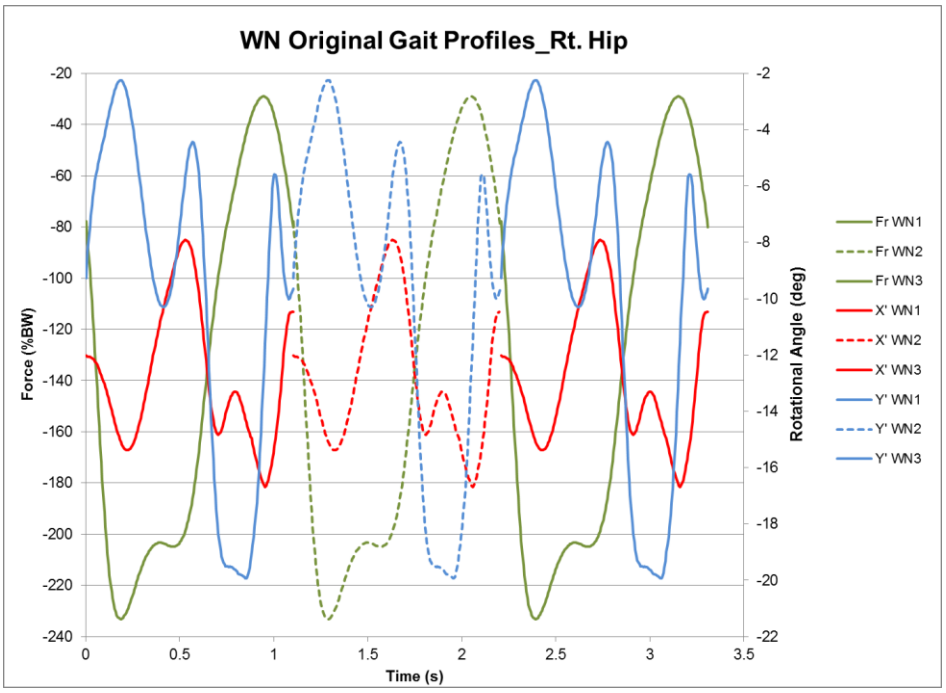

Figure D 16. Walking normally original gait profiles for the right hip.

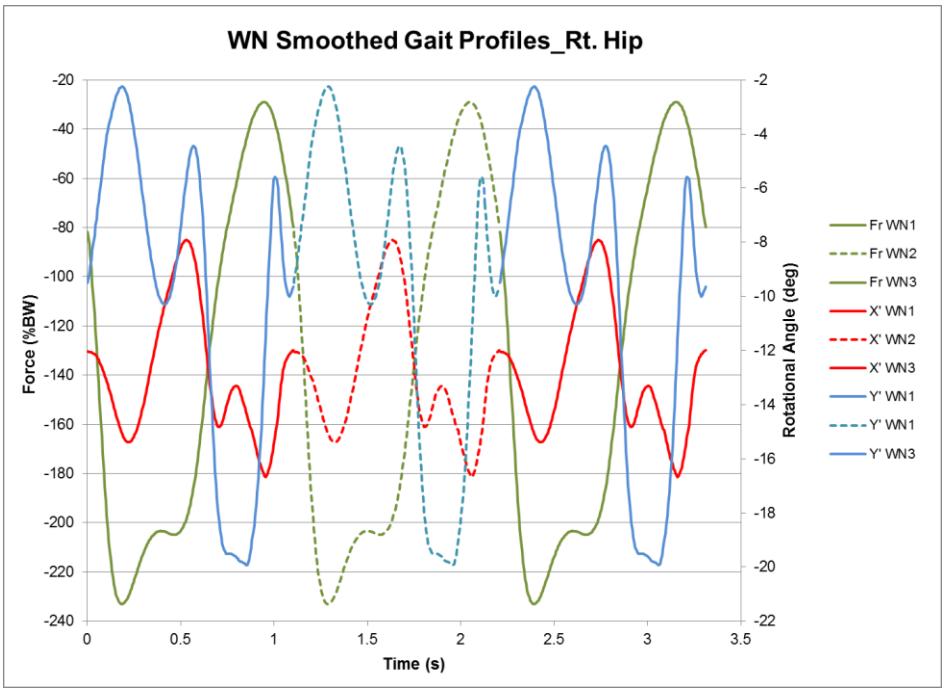

Figure D 17. Walking normally smoothed gait profiles for the right hip.

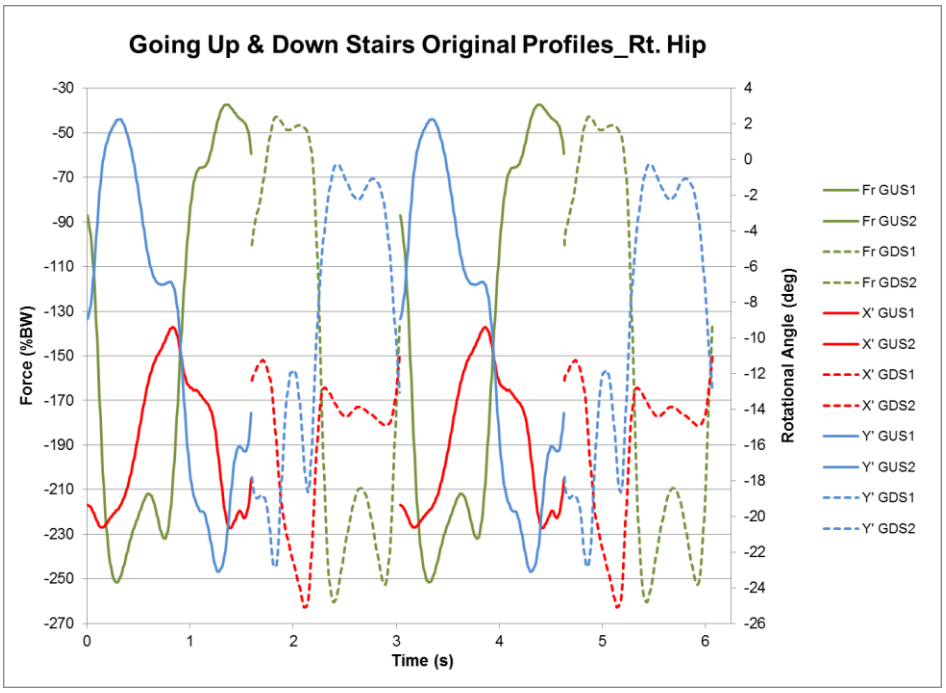

Figure D 18. Going up and down stairs original profile for the right hip.

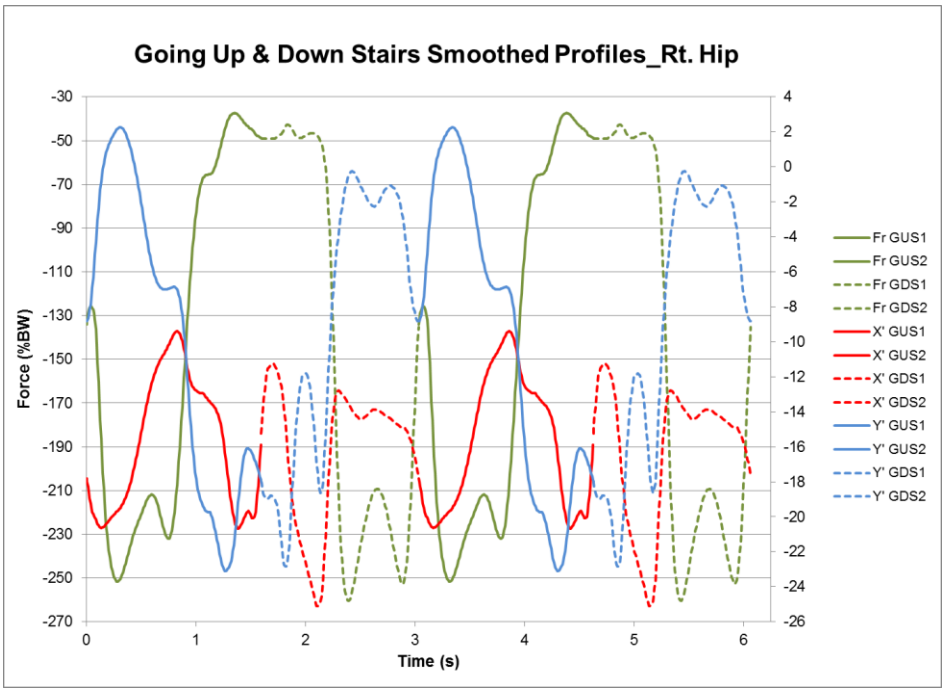

Figure D 19. Going up and down stairs smoothed profiles for the right hip.

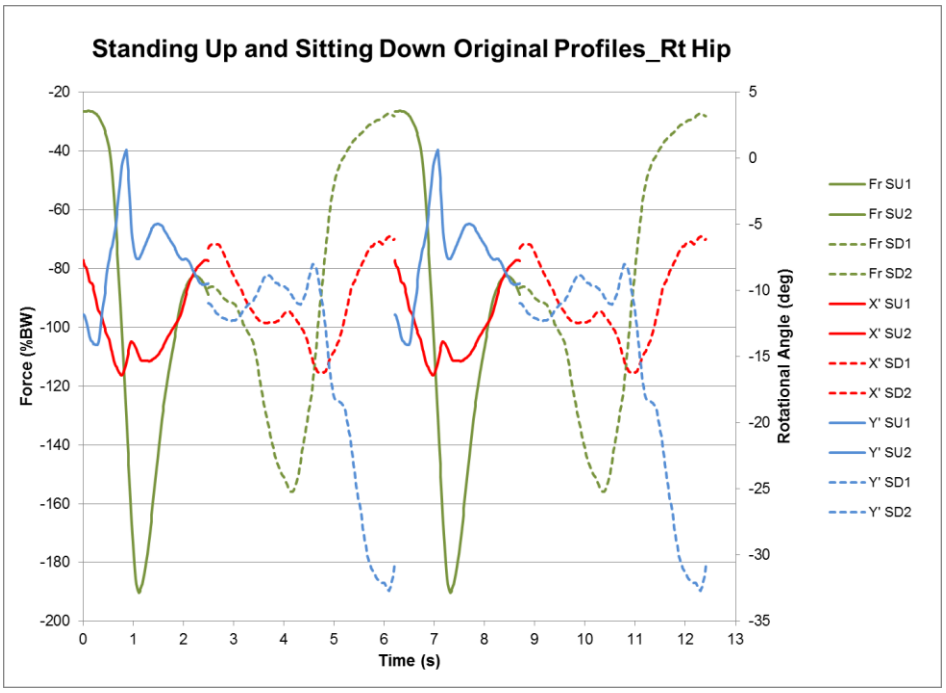

Figure D 20. Standing up and sitting down original profiles for the right hip.

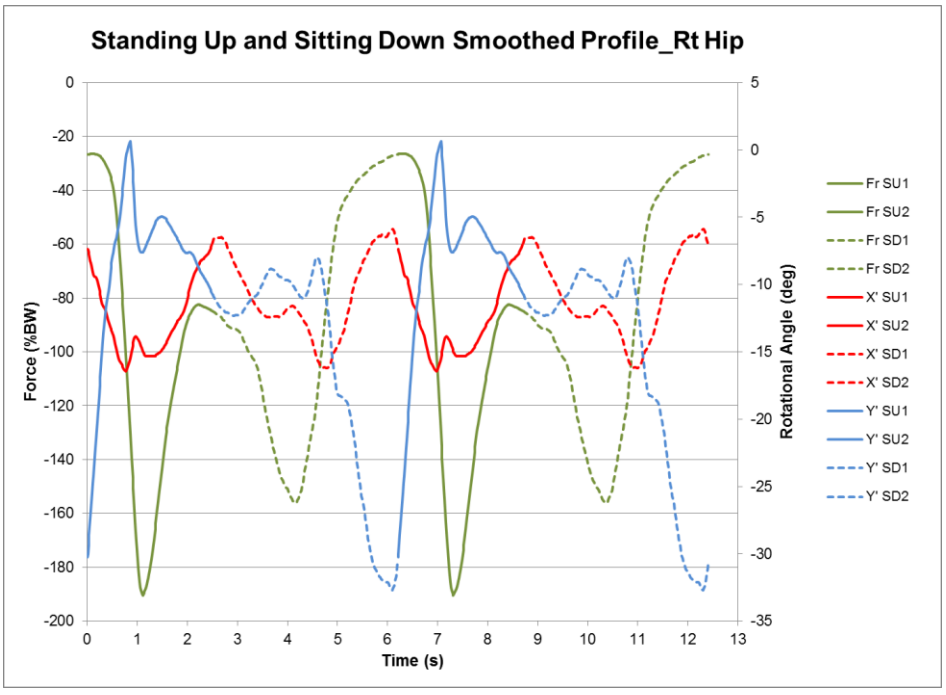

Figure D 21. Standing up and sitting down smoothed profiles for the right hip.

APPENDIX E

Surgical Technique for Mayo Stem

Step 1: Surgical Exposure

The lateral decubitus position is used, and the anterior approach is preferred.

Step 2: Femoral Neck Osteotomy

The system for femoral head resection by anatomic implant is used for this device. A guide is inserted down the femoral canal, and the resector template is used to determine proper level and orientation of femoral neck resection for the implant. The tip of the greater trochanter must be co-linear with the center of the femoral head to assure optimum abductor muscle tension (Figure E 1). This resection can be done with a single cut that does not violate the trochanter. If the line of osteotomy is correctly placed, the orientation of the femoral neck cut is used to guide the preparation of the proximal femur (Figure E 2).

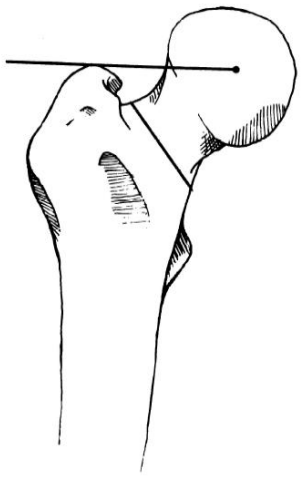

Figure E 1. **The femoral neck resection should balance the abductors, which typically occurs when a line from the superior aspect of the greater trochanter passes through the center of the femoral head.**

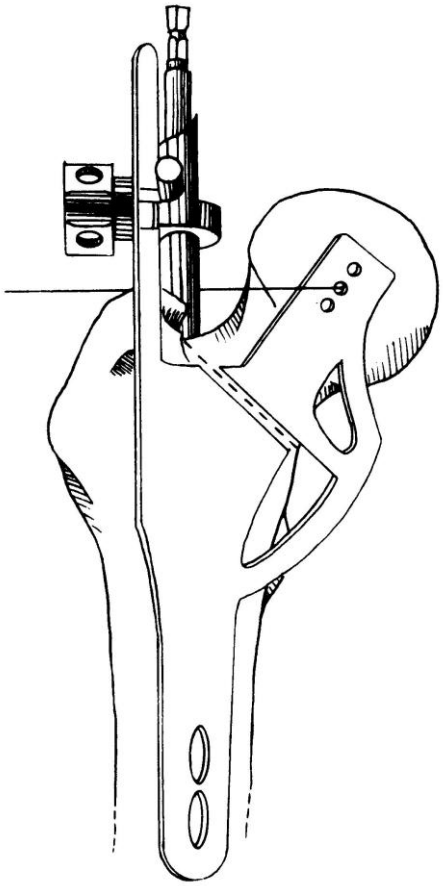

Figure E 2. **The anatomic femoral resection guide is used to resect the femoral neck using either the anterior or the posterior approach.**

Step 3: Femoral Preparation

A T-handle reamer is placed down the lateral aspect of the medullary canal to determine the orientation of the lateral aspect of the femur. This becomes the landmark for inserting the rasp.

The smallest femoral rasp is used first. Particular care should be taken to assure that the tail of the rasp is parallel with the lateral cortex by allowing the rasp to begin in a slight varus position. As the rasp is inserted down the canal, the rasp will

become more valgus in position because its tail is guided by the lateral femoral cortex (Figure E 3). Serial rasping occurs until the rasp can no longer be advanced down the canal. The rasp should be tapped cautiously so the top row of teeth are 1 to 2 mm below the level of resection.

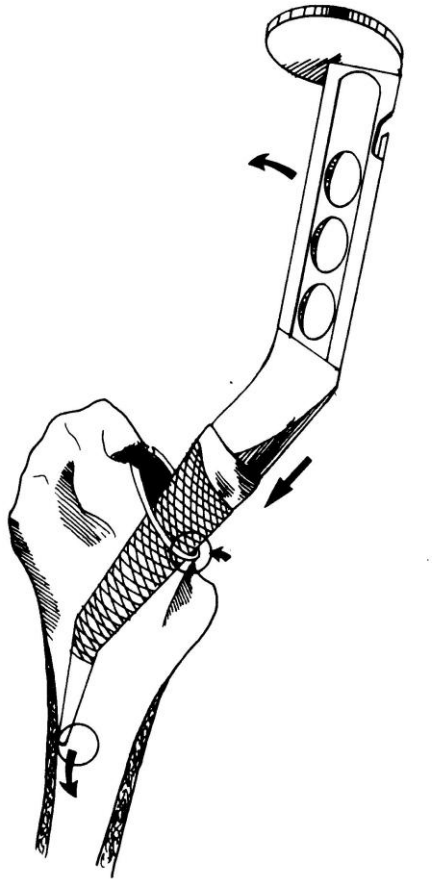

Figure E 3. **Rasping the proximal femur begins with the rasp in slight varus, ultimately going into valgus position.**

Step 4: Stability and Trial Reduction

With proper preparation, when the teeth of the rasp are even with or slightly countersunk distal to the level of neck resection, the rasp handle can be rotated and maneuvered in varus/valgus to evaluate the anticipated stability of the implant. The rasp handle is then removed, and the trial femoral head and neck is inserted (Figure E 4). The length dimensions are identical to those of the anatomic system. As with other designs, the usual resection, approximately a finger breadth above the lesser trochanter, is consistent with the standard-length femoral neck modular component. I prefer a 28-mm-diameter head for all cases with acetabular components of 50 mm or more in diameter. For acetabuli less than 50 mm in diameter, the 22-mm head is used.

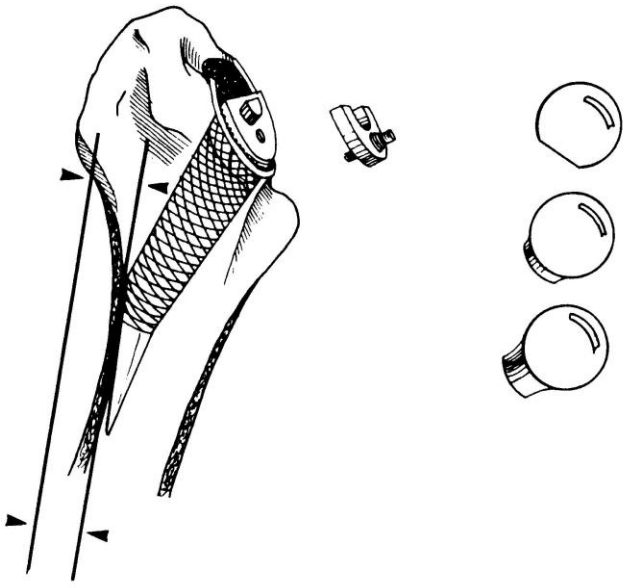

Figure E 4. **Optimum orientation occurs when the tail of the rasp parallels the lateral femoral cortex. The rasp is typically countersunk about one row of teeth below the level of resection. The trial of the femoral head and neck is important with this implant for optimum tension and stability.**

Step 5: Component Insertion

The implant is inserted so the dimple on the proximal portion of the device is at or just below the level of neck resection (Figure E 5). As noted, this level of implant position is safely obtained if the rasp has been inserted to or just past the row of teeth. Fractures from excessive hoop stresses are rare if these two technical considerations are followed. Impaction of the femoral component should not continue if no progress is made down the canal. If the implant remains proud, then trial reduction with the shorter neck implant is used.

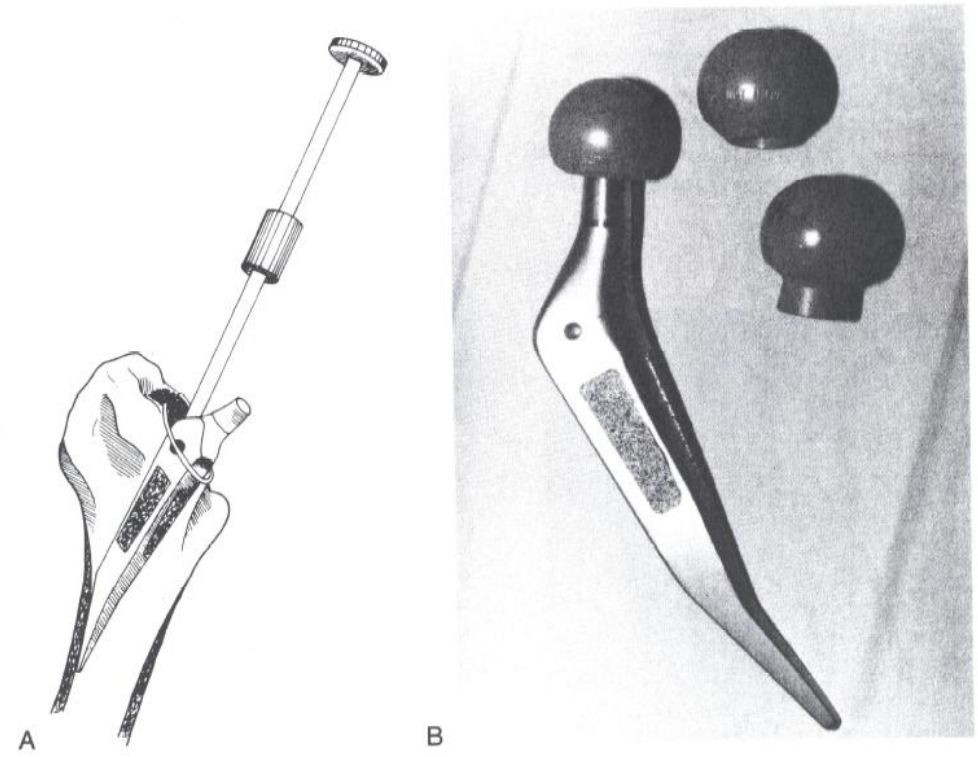

Figure E 5. **The implant is inserted to the point where the dimple coincides with the level of the resected femoral neck. (A) The short-stemmed implant with modular head and necks. (B) The location of the dimple in relation to the implant is shown, along with the trial femoral heads that may be used to confirm optimum length after inserting the implant.**

Femoral rasping does not require formal consideration of the femoral anteversion because the rasp can follow only one line down the canal. The femoral anteversion of the implant is dictated by the orientation of the femoral neck. The modular head is then tapped on the implant and reduction is routine. Stability is checked in all planes with extension-external rotation and flexion-internal rotation. Once the abductors have been secured with No. 5 nonabsorable sutures through bone, closing the incision is left to the surgeon's choice.

APPENDIX F

Results

F.1. Going Up and Down Stairs Average Error Frequency Charts

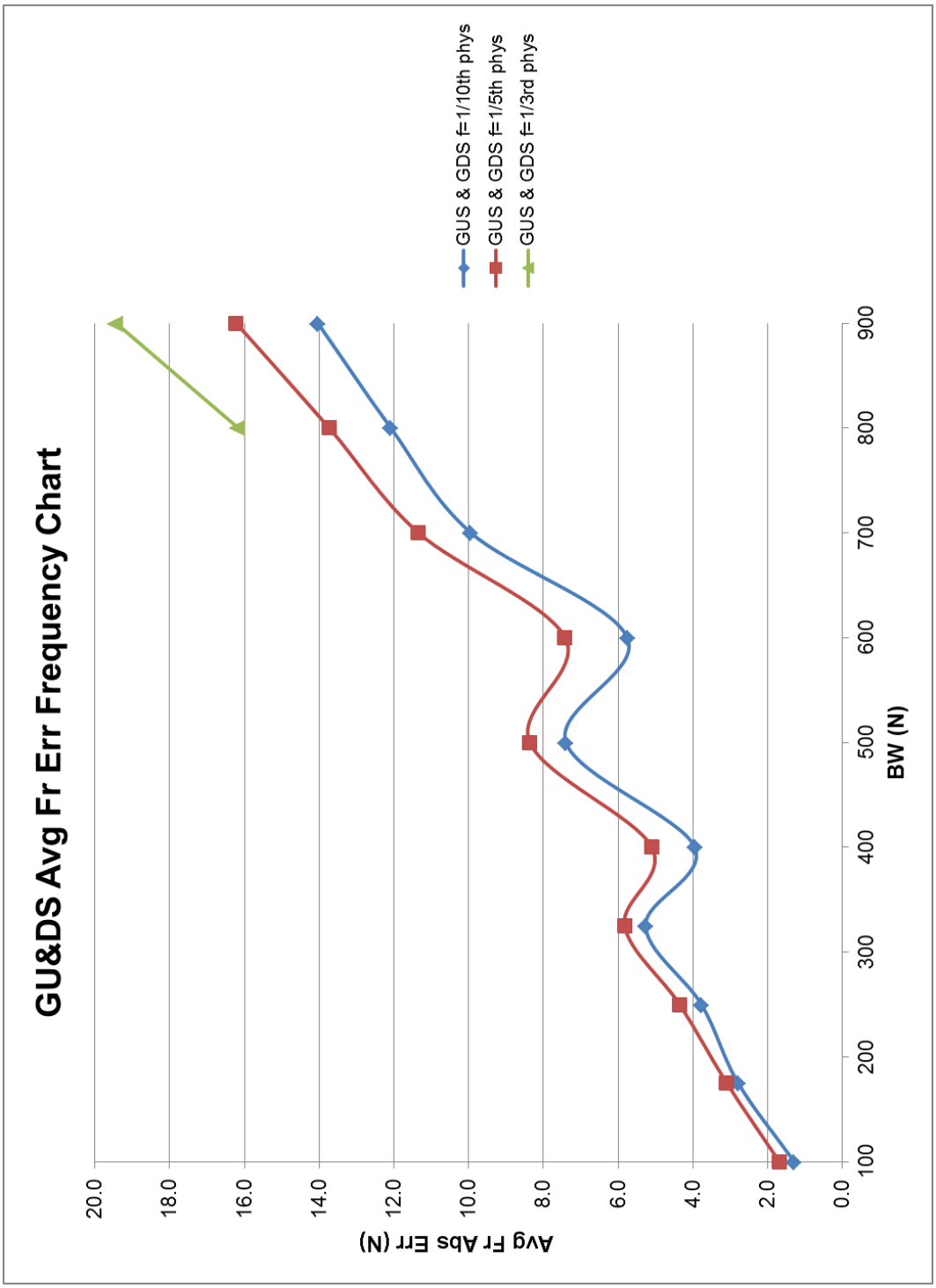

Figure F 1. GU&DS Avg F_R Err frequency chart.

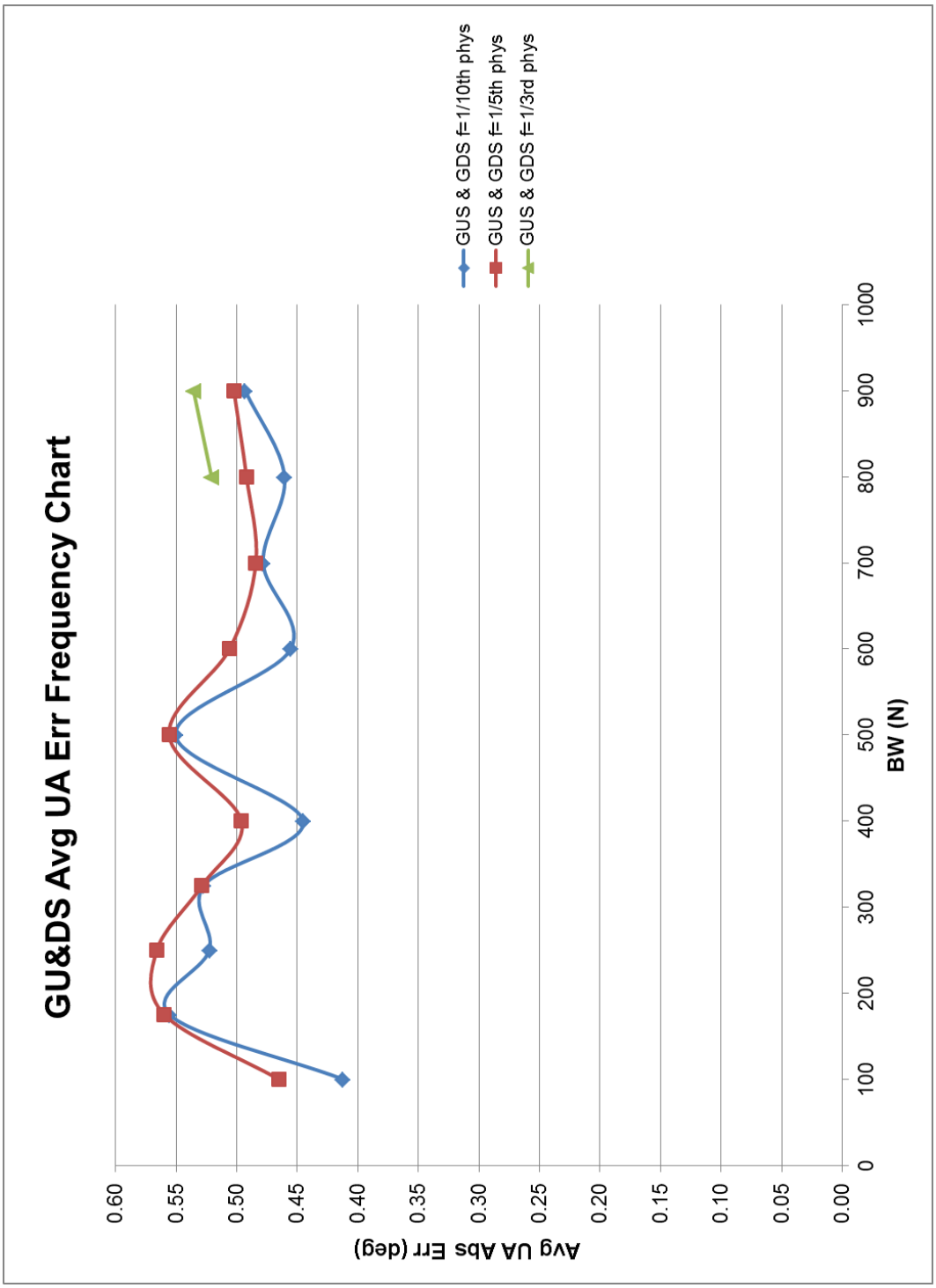

Figure F 2. GU&DS Avg UA Err frequency chart.

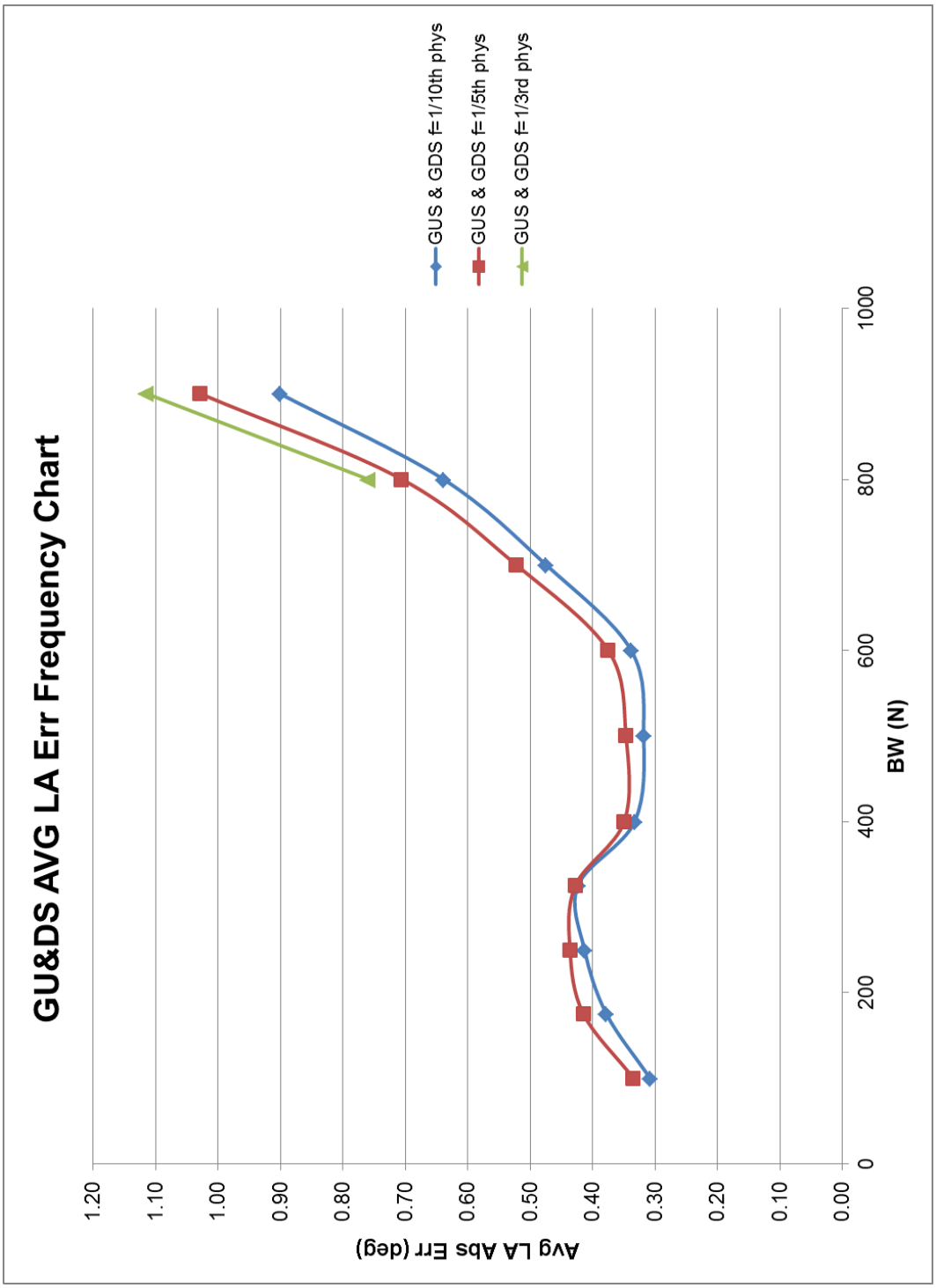

Figure F 3. GU&DS Avg LA Err frequency chart.

F.2. Going Up and Down Stairs Maximum Error Frequency Charts

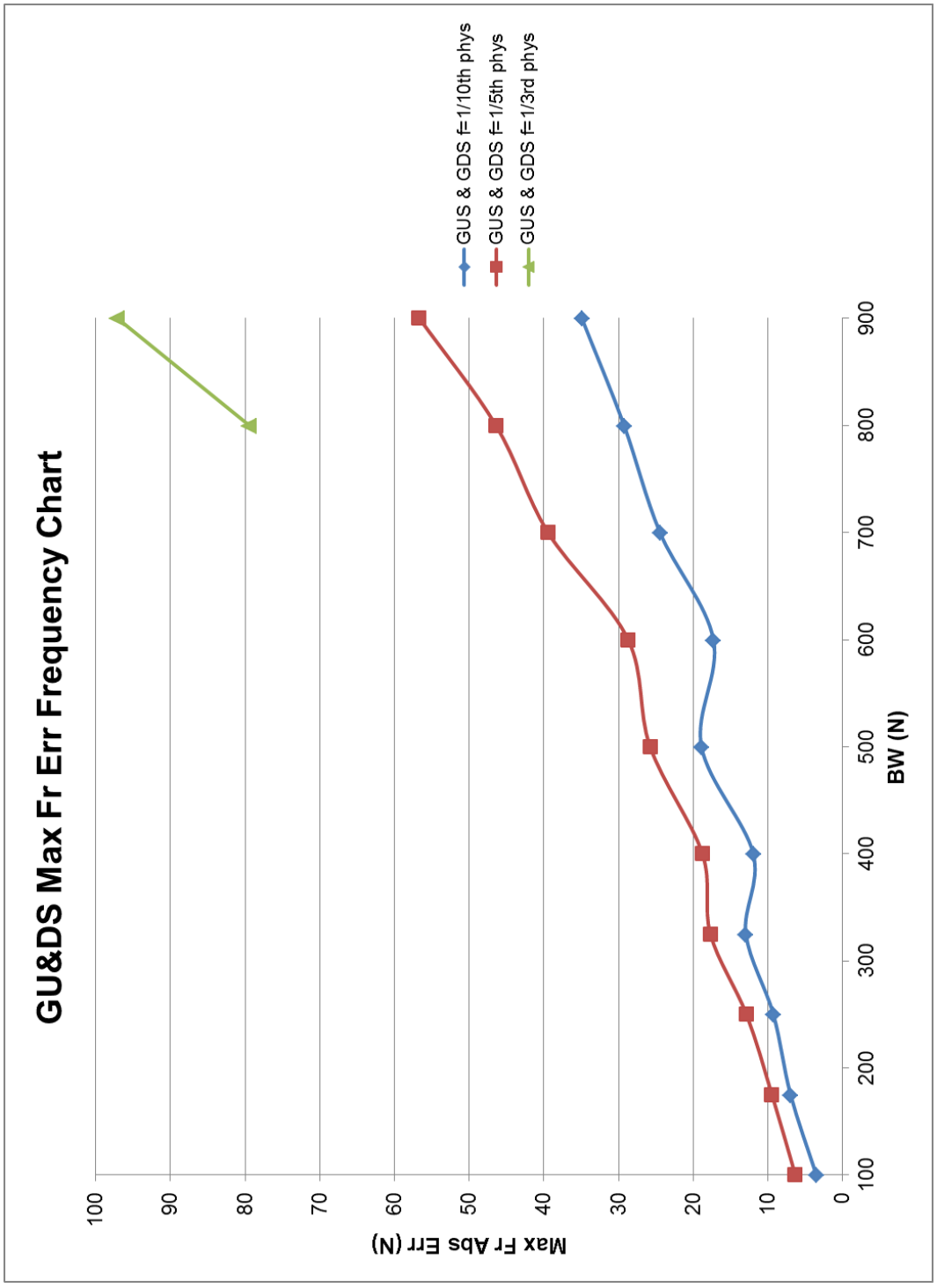

Figure F 4. GU&DS Max F_R Err frequency chart.

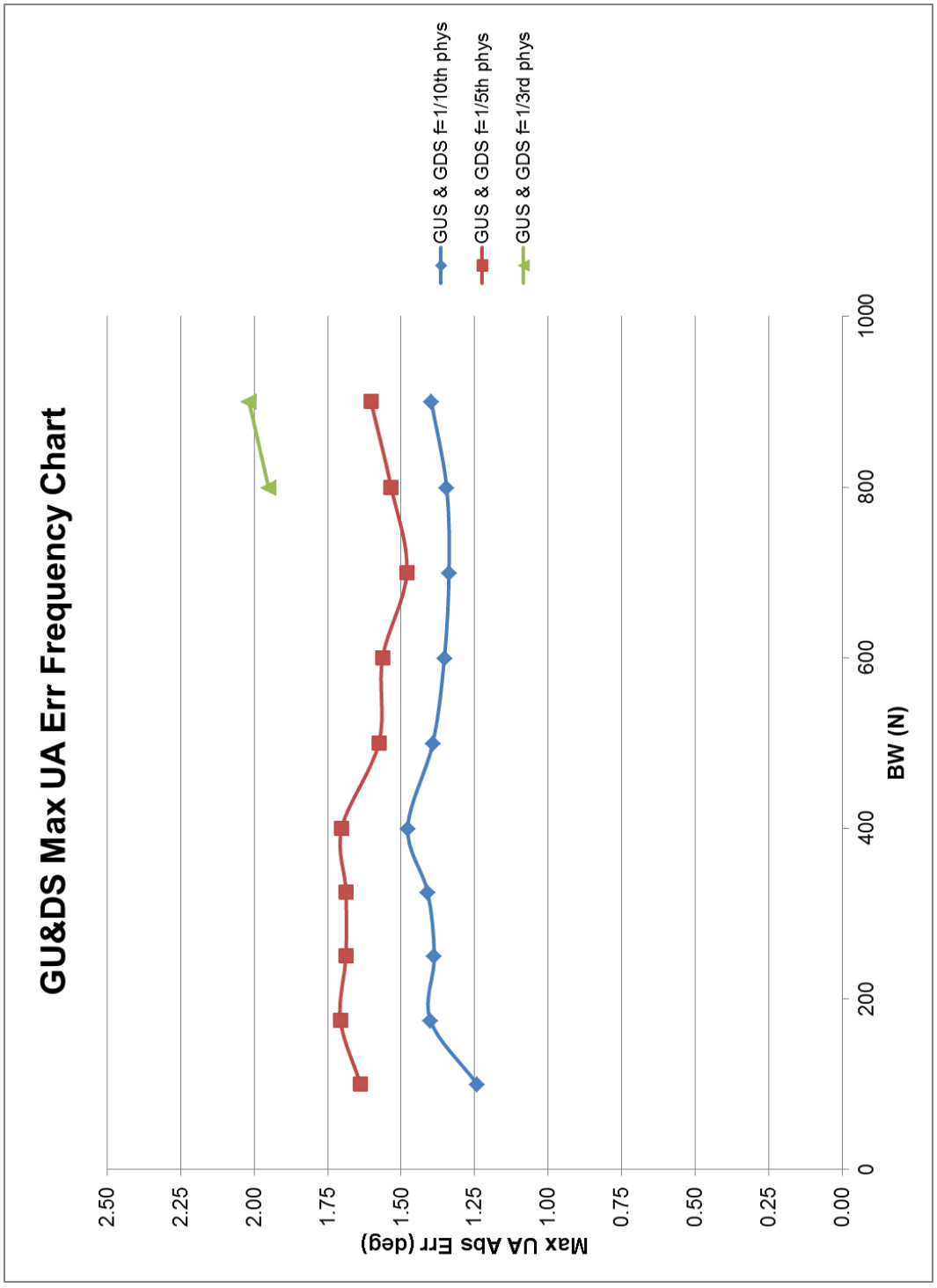

Figure F 5. GU&DS Max UA frequency chart.

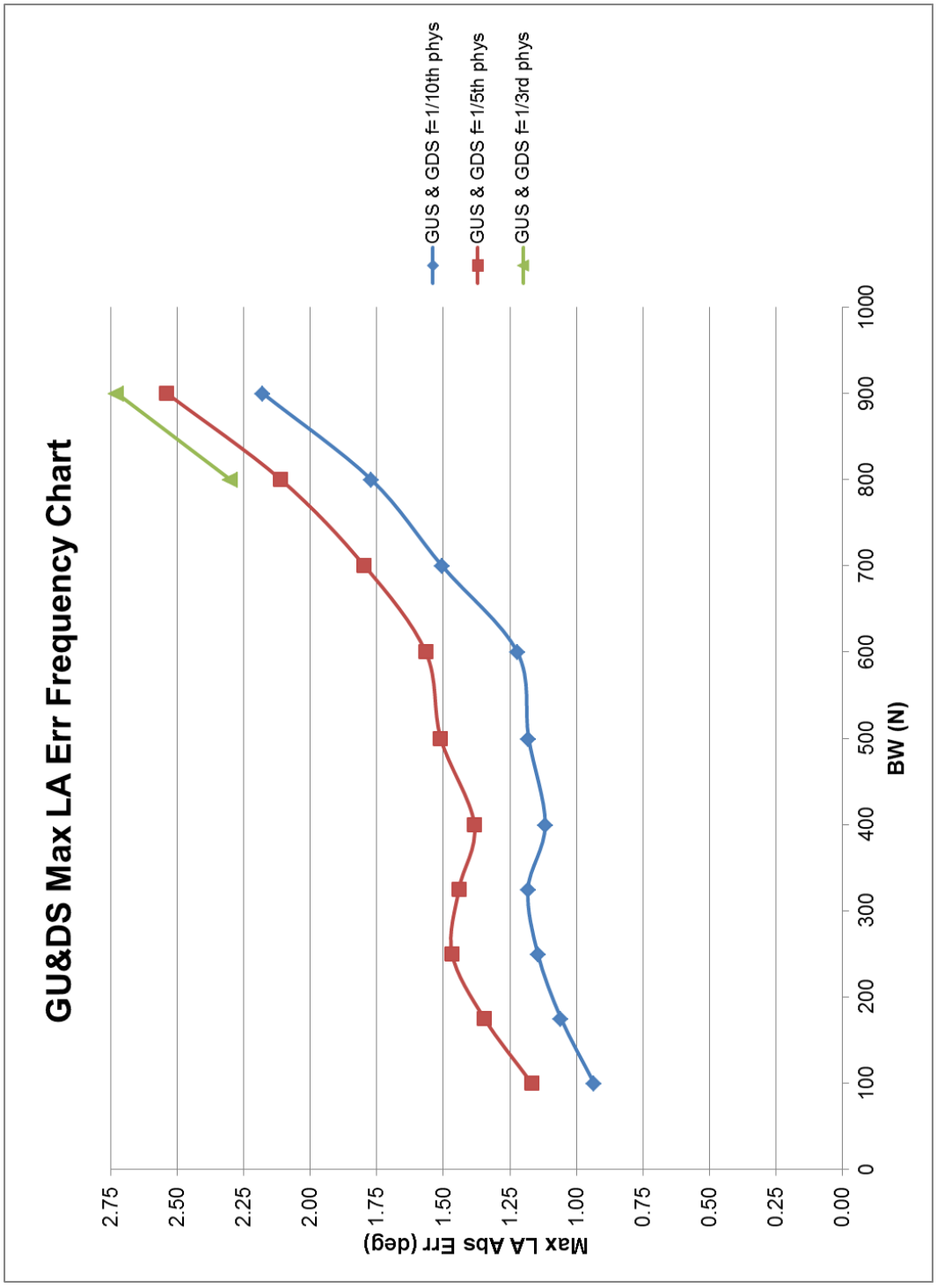

Figure F 6. GU&DS Max LA Err frequency chart.

F.3. Standing Up and Sitting Down Average Error Frequency Charts

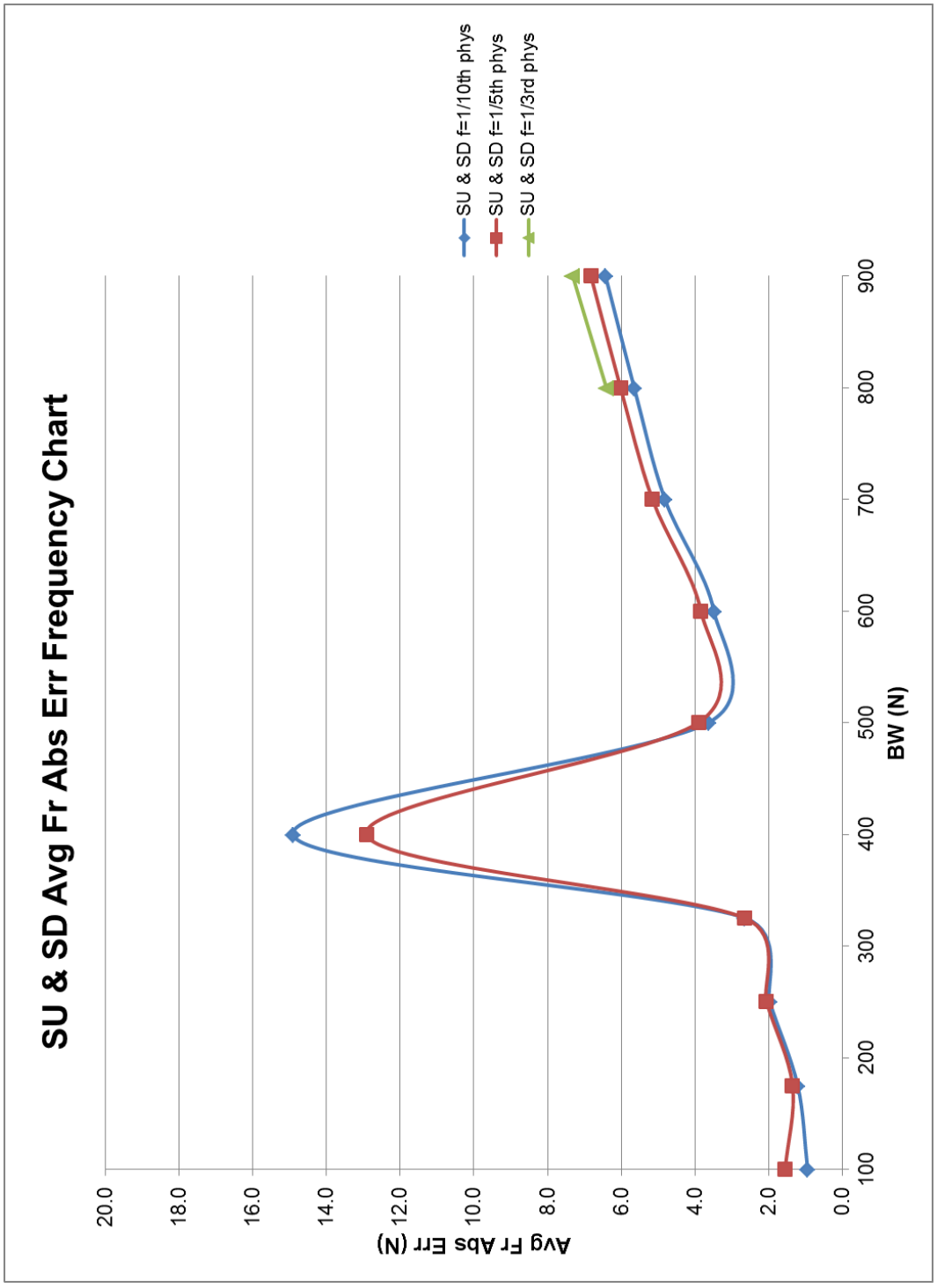

Figure F 7. SU & SD Avg F_R Err frequency chart.

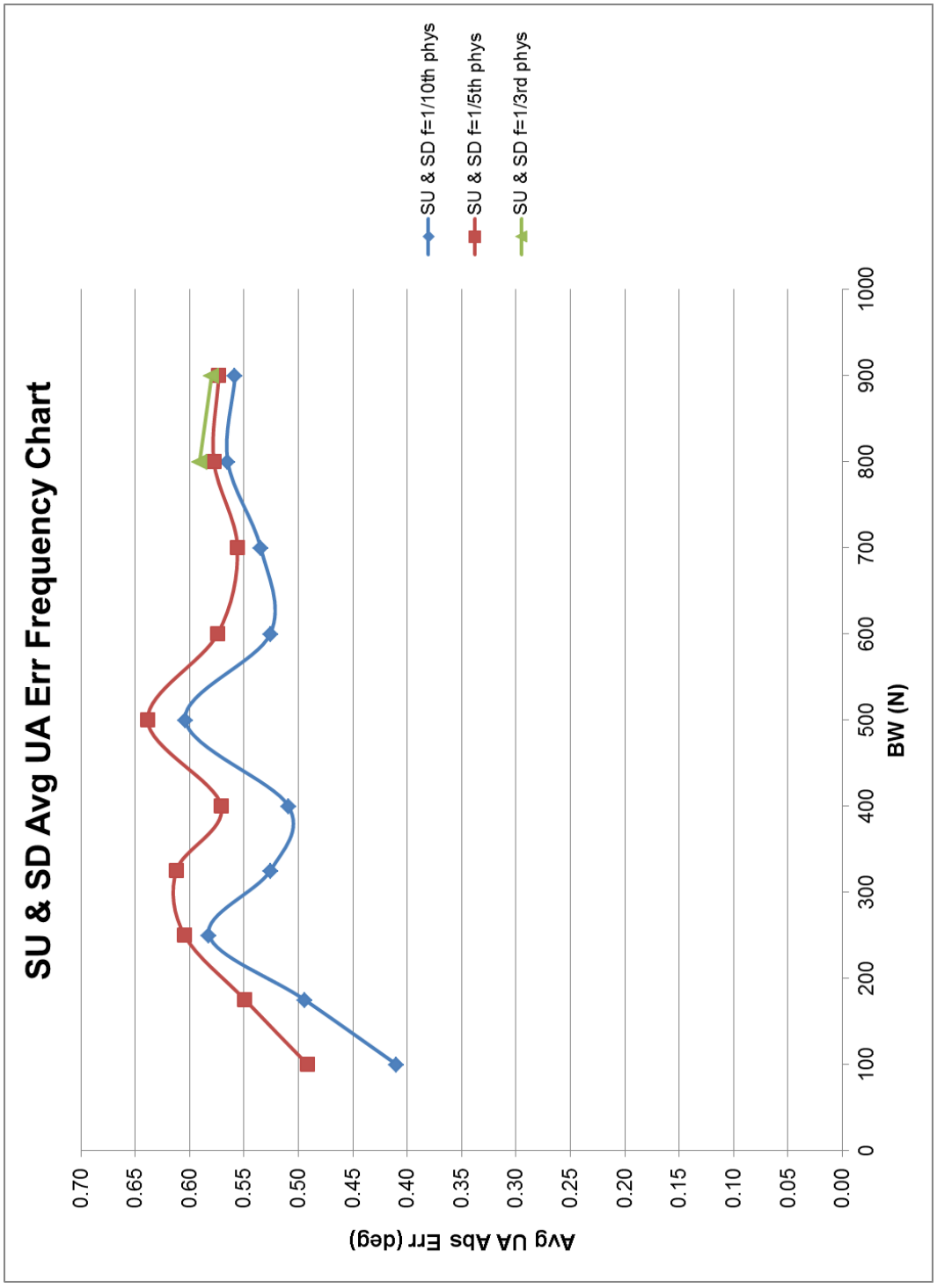

Figure F 8. SU & SD Avg UA Err frequency chart.

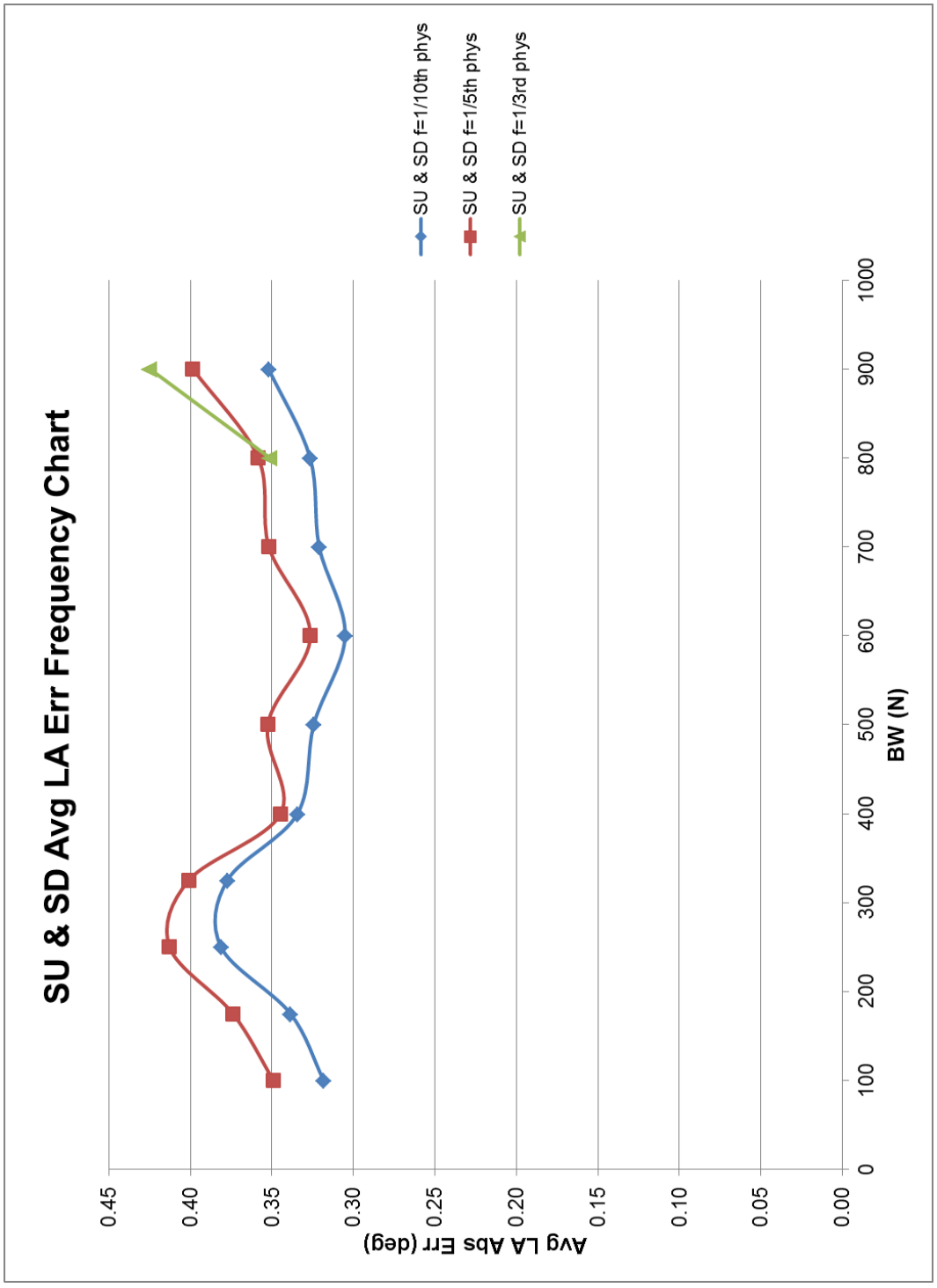

Figure F 9. SU & SD Avg LA Err frequency chart.

F.4. Standing UP and Sitting Down Maximum Error Frequency Charts

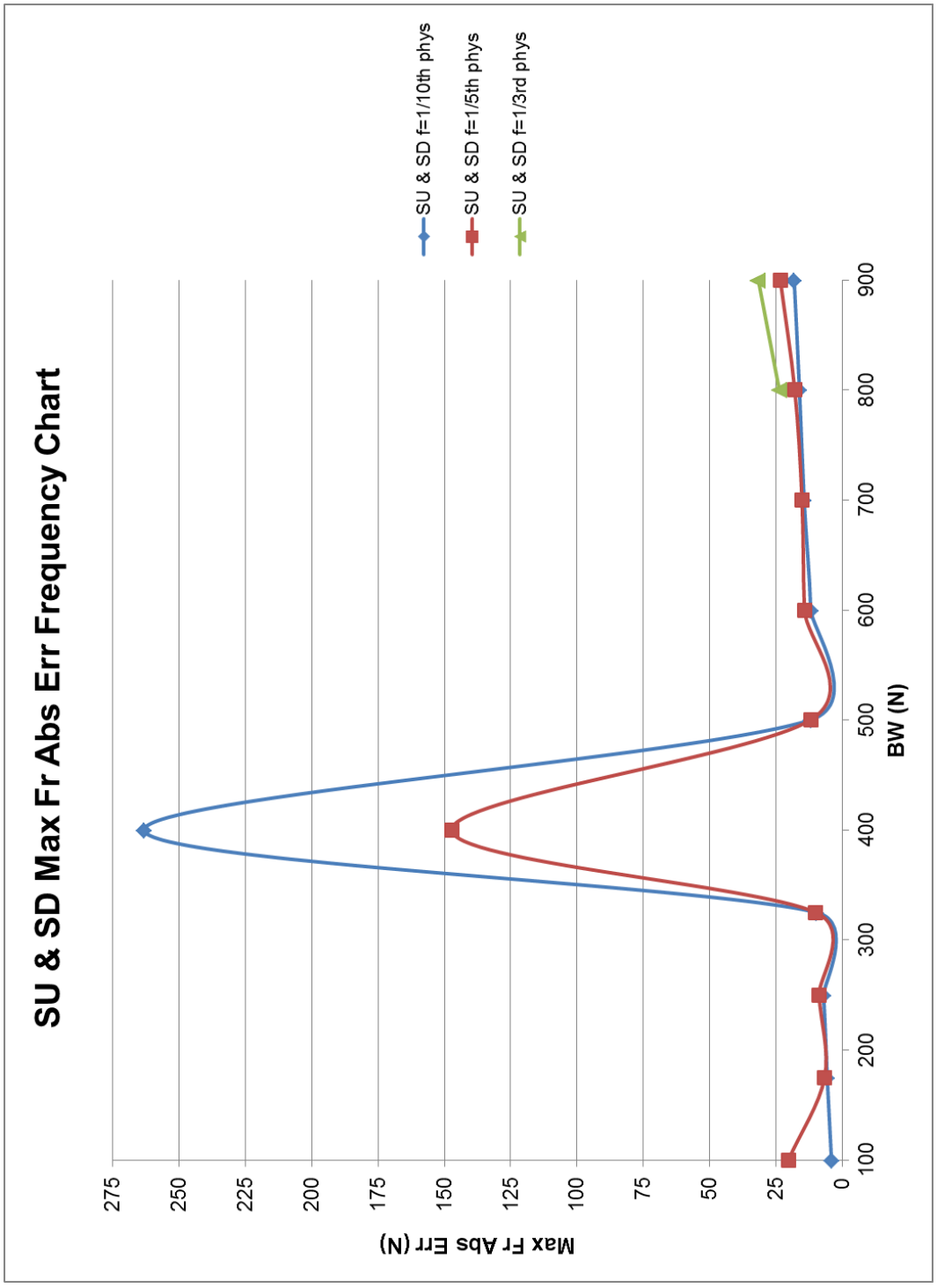

Figure F 10. SU & SD Max F_R Abs Err frequency chart.

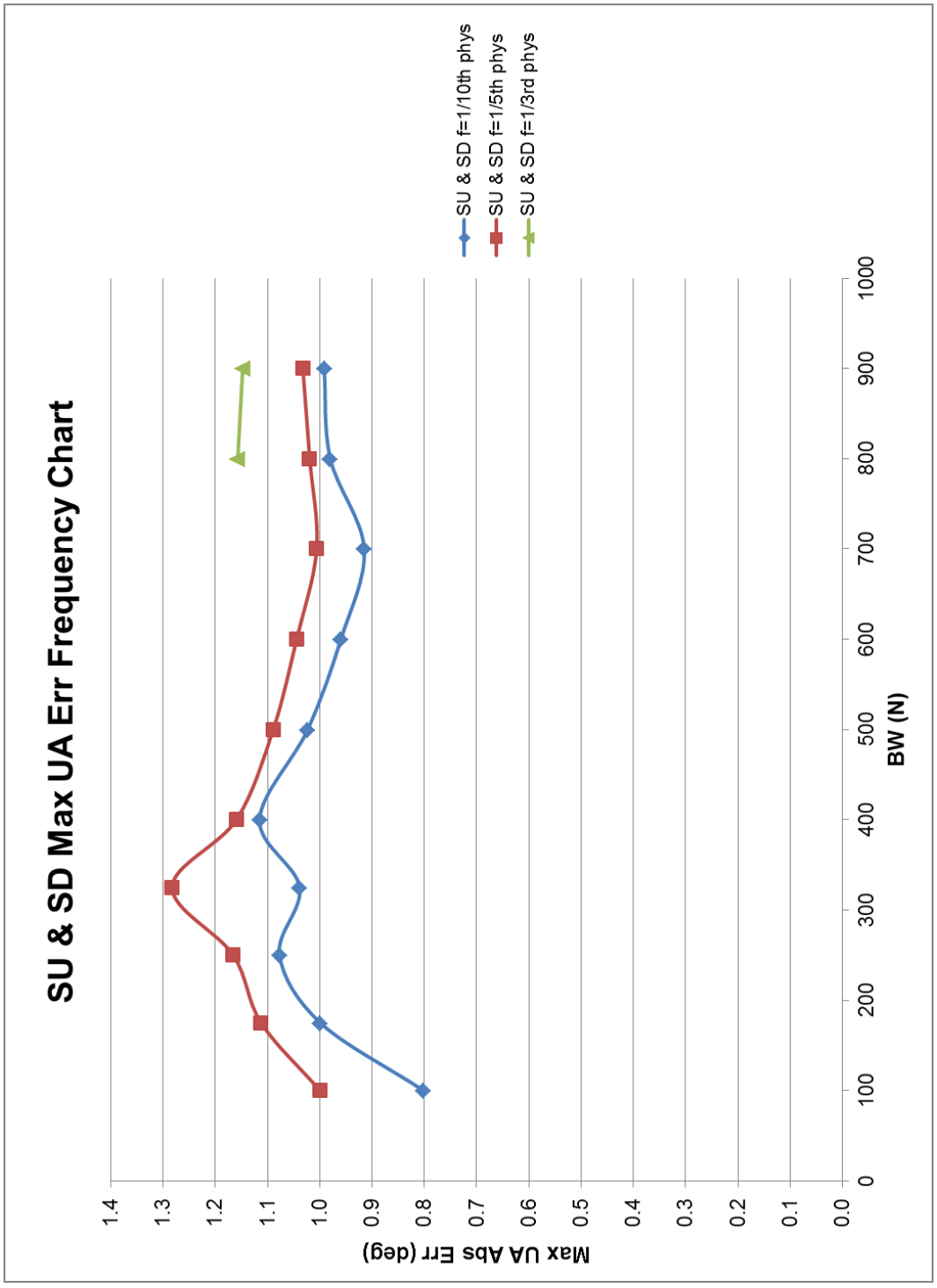

Figure F 11. SU & SD Max UA Err frequency chart.

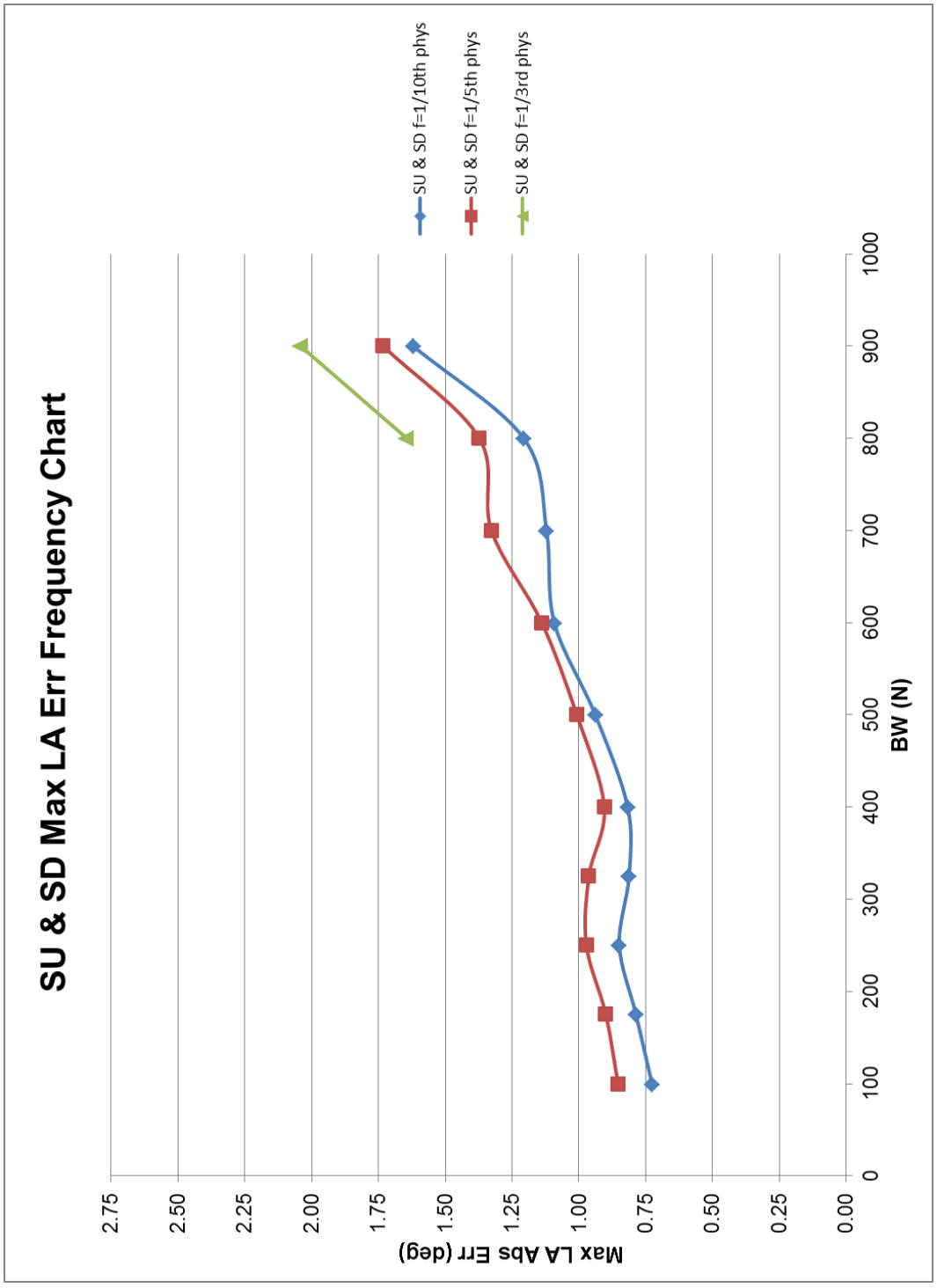

Figure F 12. SU & SD Max LA Err frequency chart.

F.5. Walking Normally Average Error Repeatability

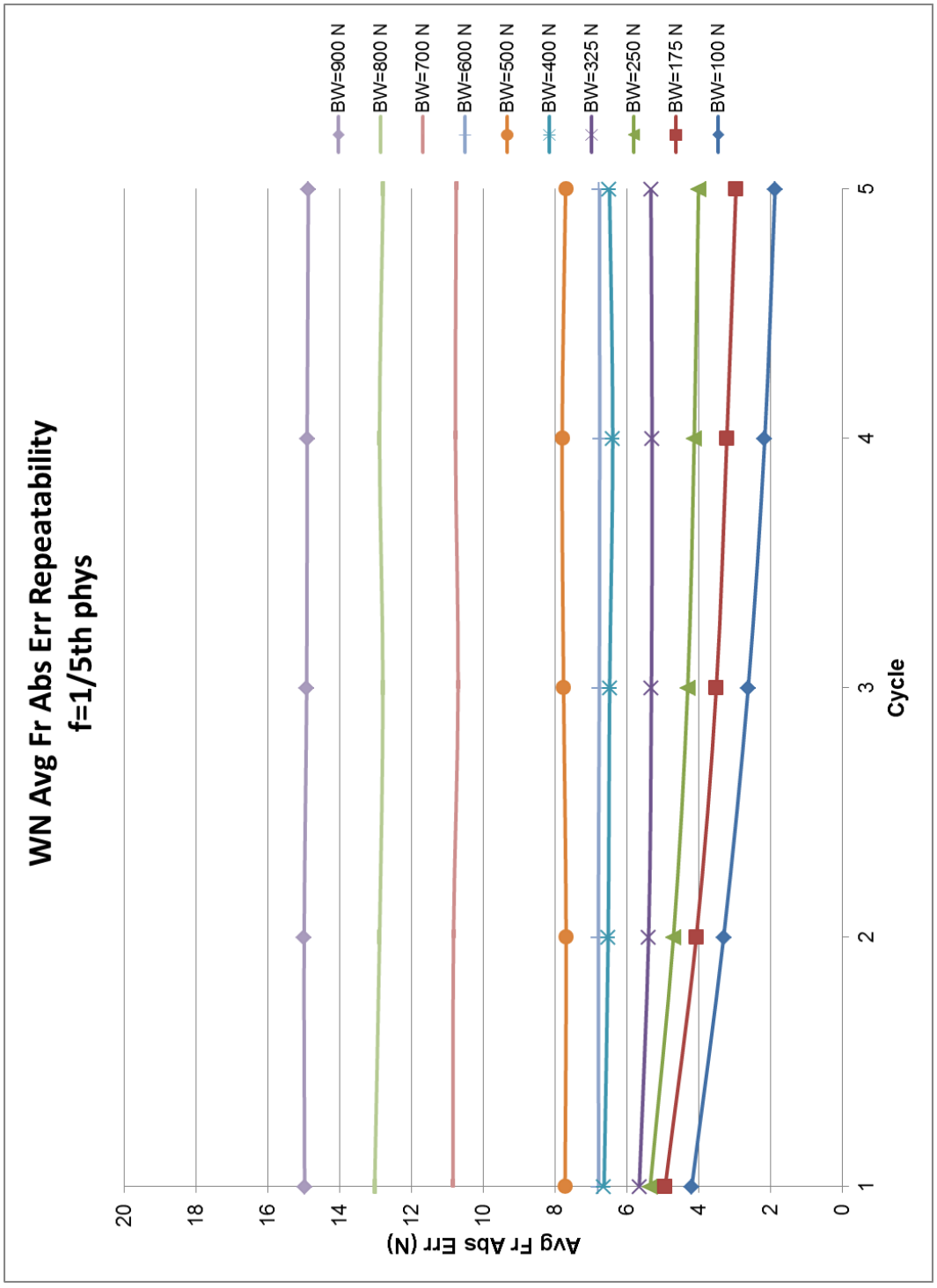

Figure F 13. WN Avg F_R Abs Err repeatability at 1/5th Phys.

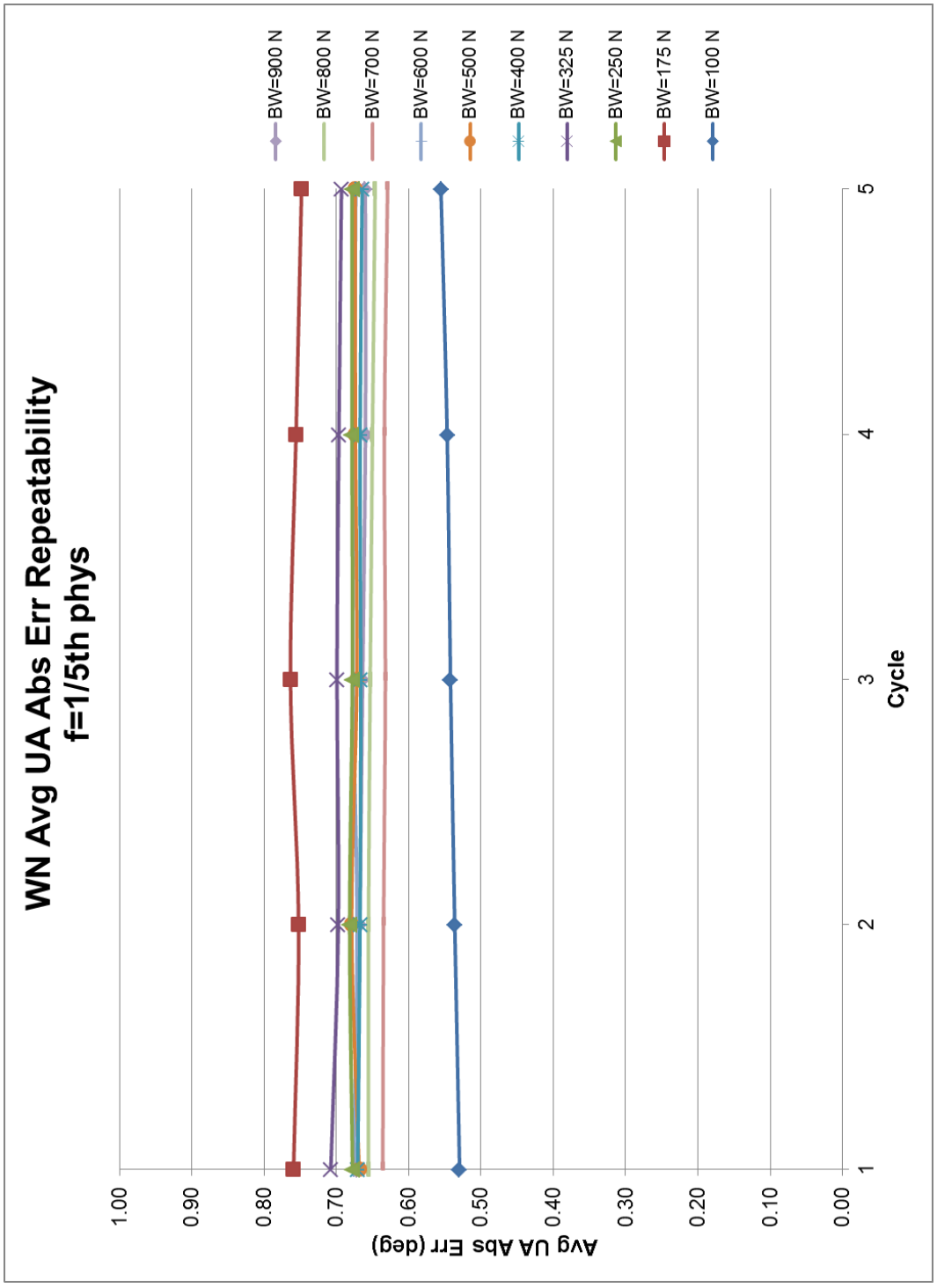

Figure F 14. WN Avg UA Abs Err repeatability at 1/5th Phys.

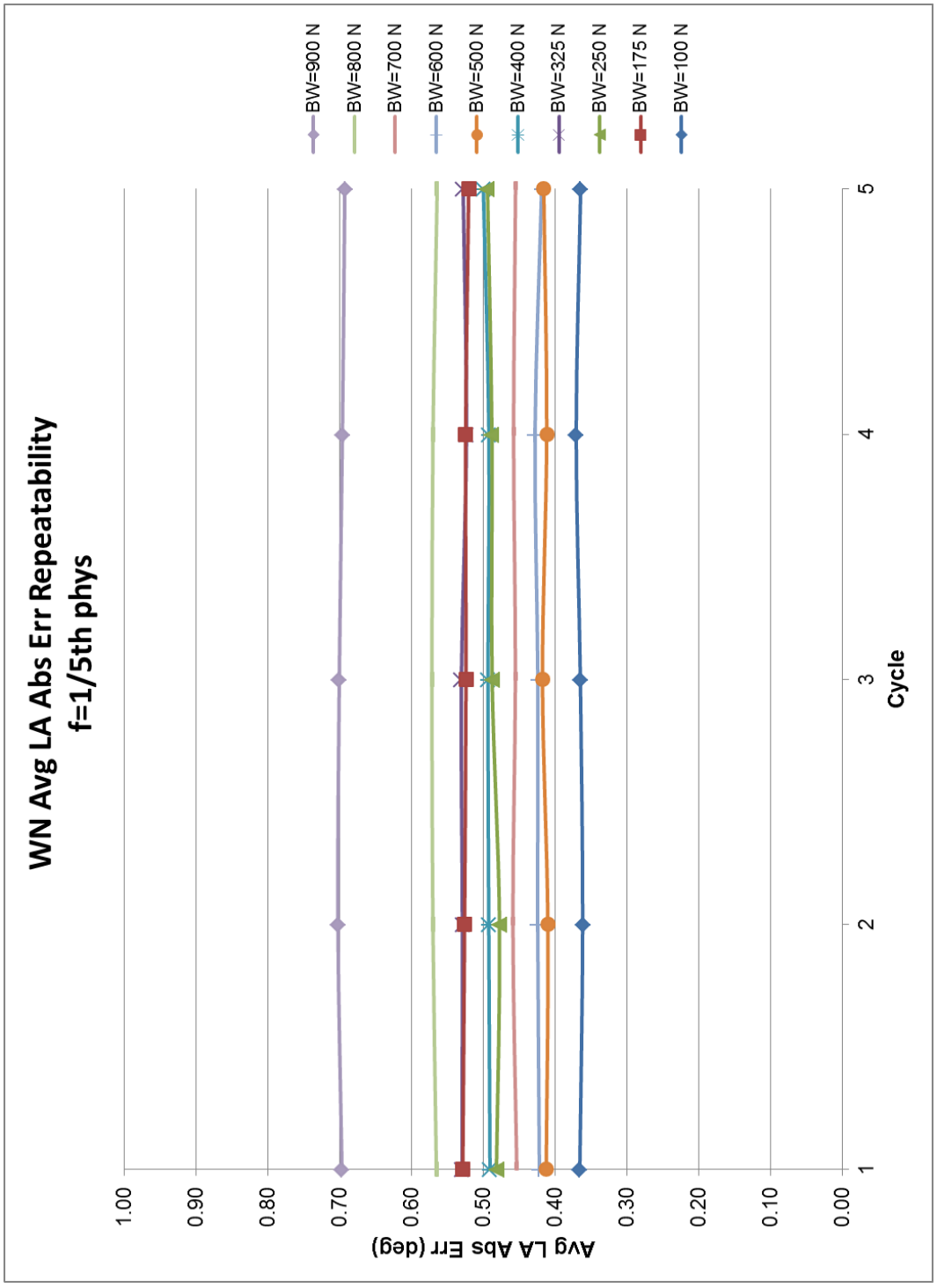

Figure F 15. WN Avg LA Abs Err repeatability at 1/5th Phys.

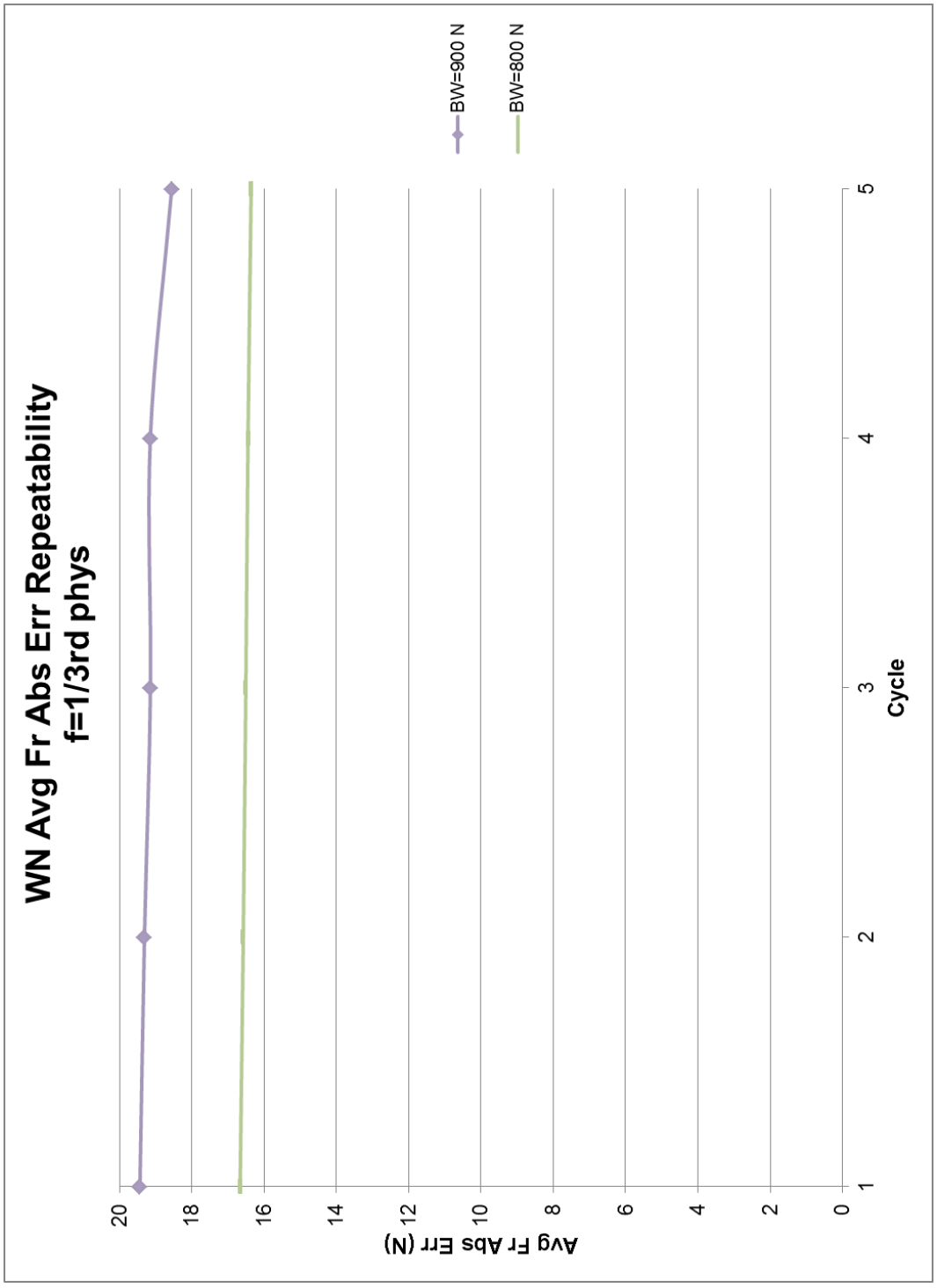

Figure F 16. WN Avg F_R Abs Err repeatability at 1/3rd Phys.

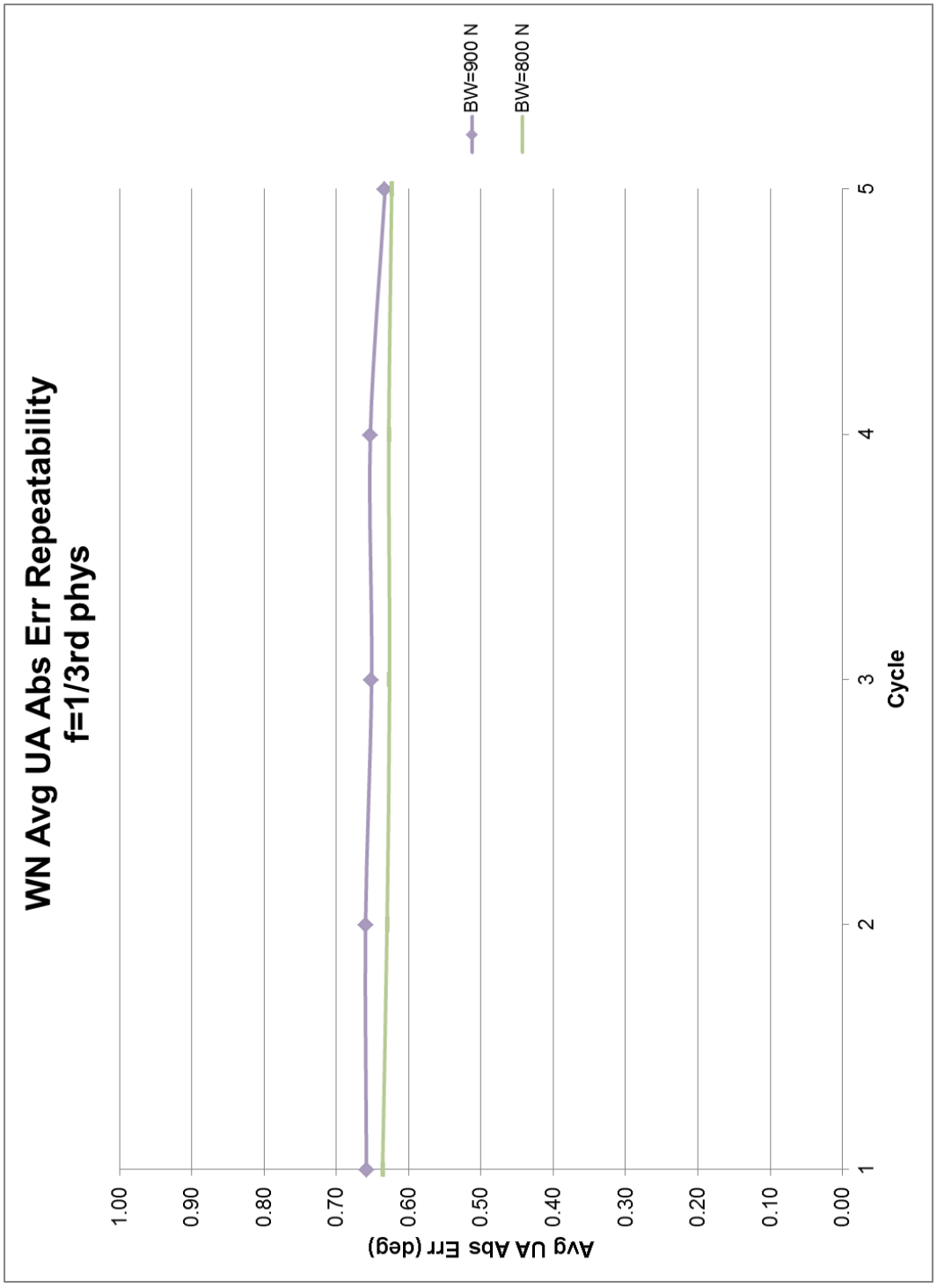

Figure F 17. WN Avg UA Abs Err repeatability at 1/3rd Phys.

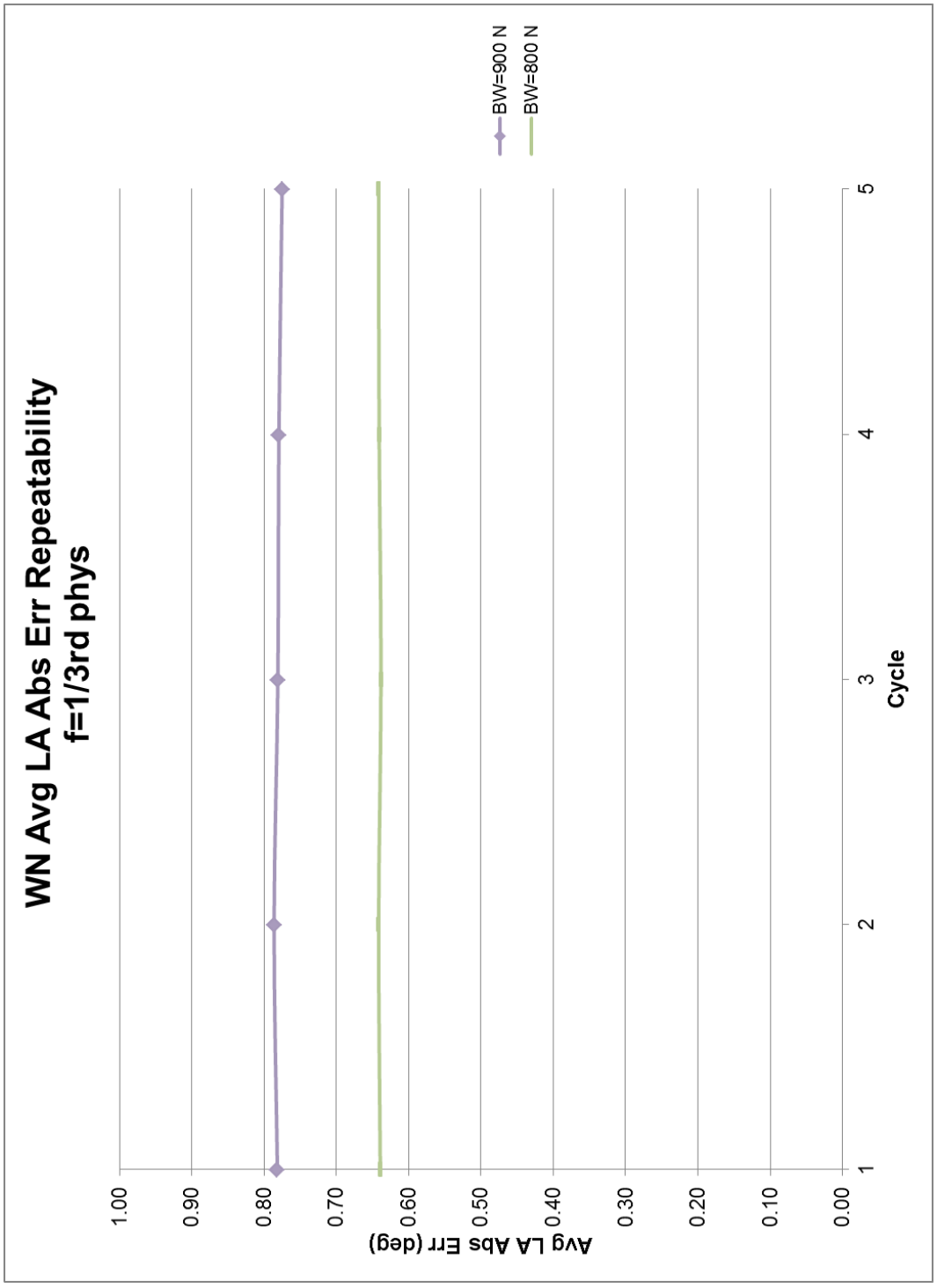

Figure F 18. WN Avg LA Err repeatability at 1/3rd Phys.

F.6. Walking Normally Maximum Error Repeatability

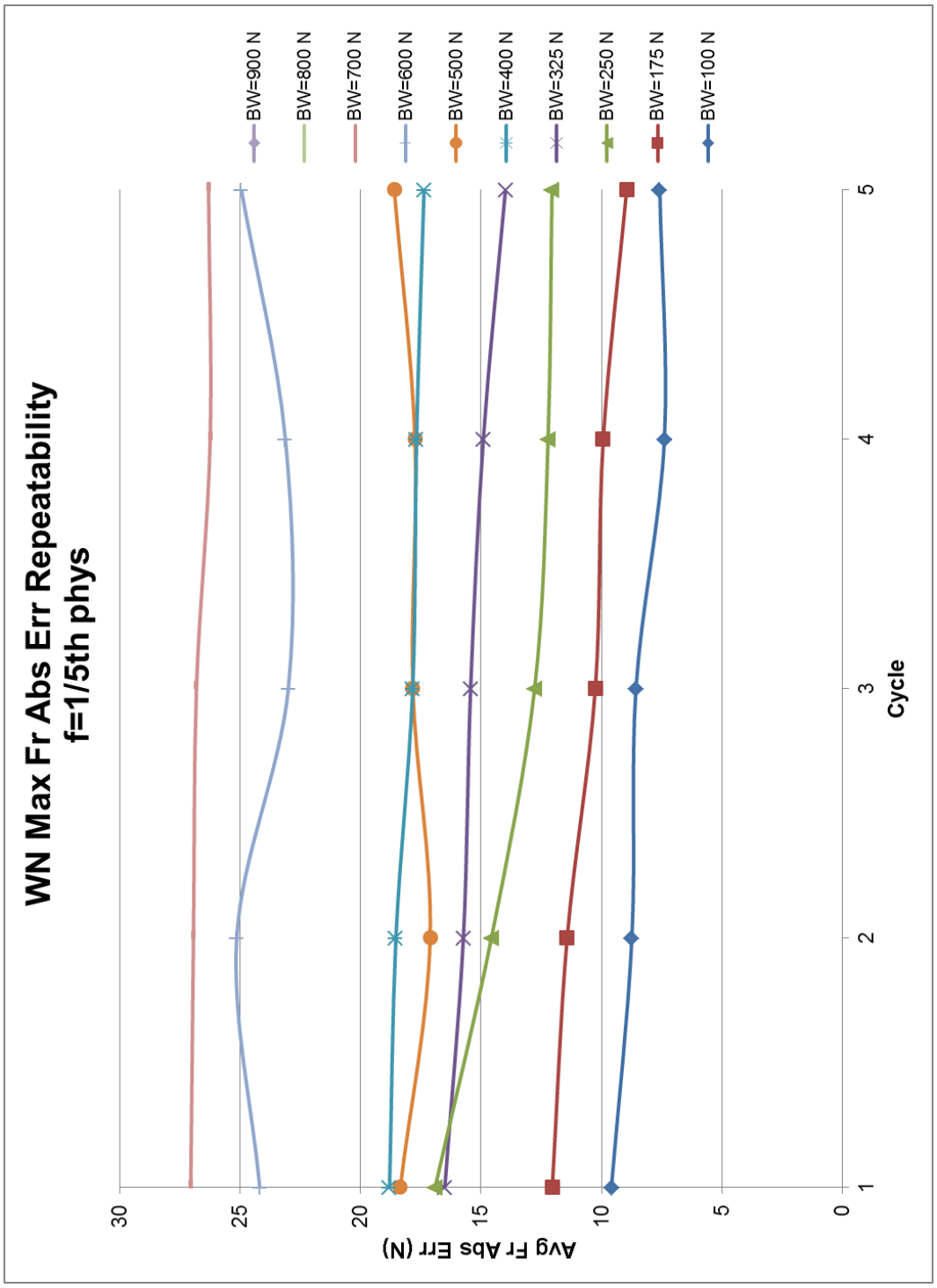

Figure F 19. WN Max F_R Abs Err repeatability at 1/5th Phys.

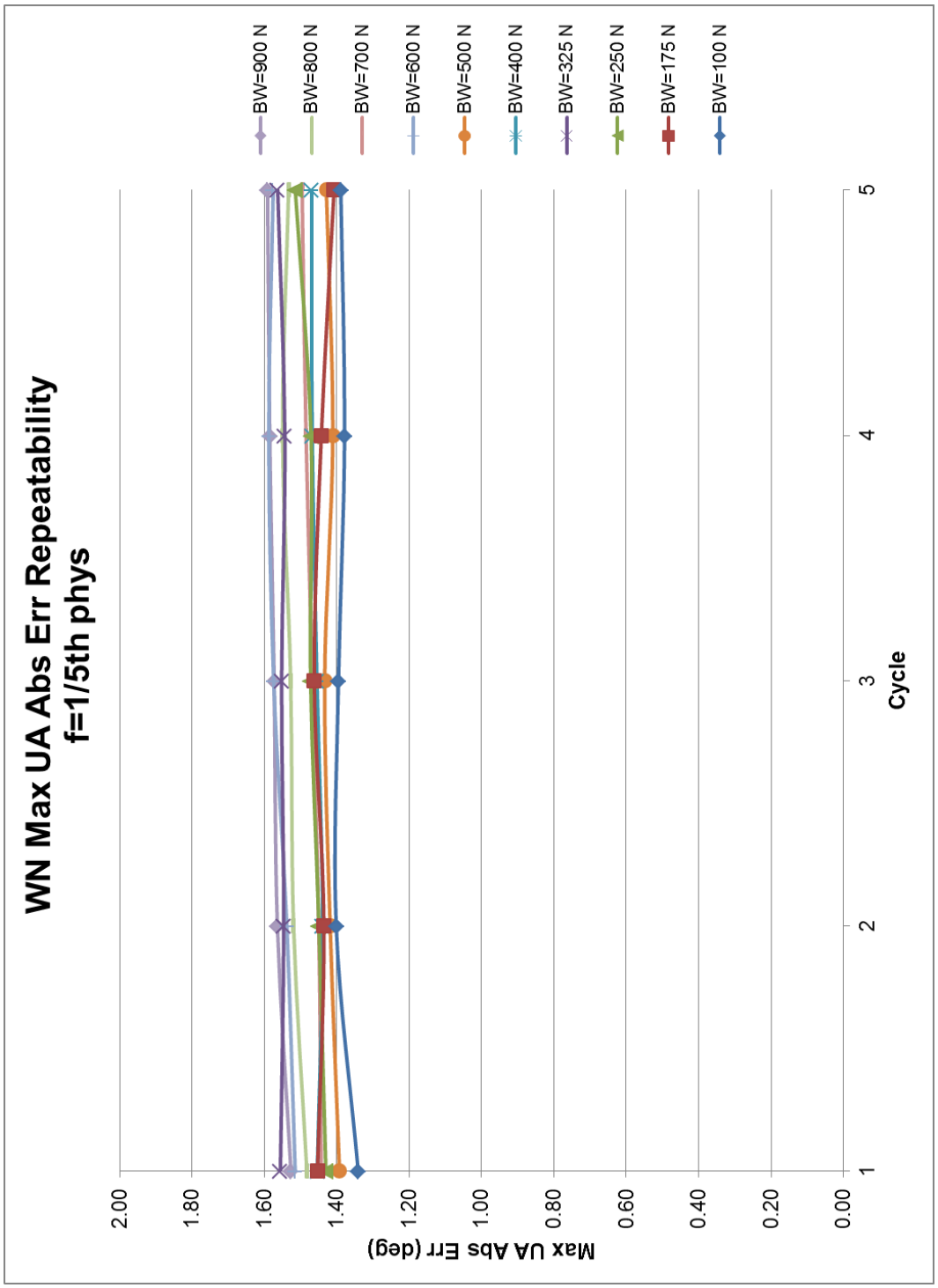

Figure F 20. WN Max UA Abs Err repeatability at 1/5th Phys.

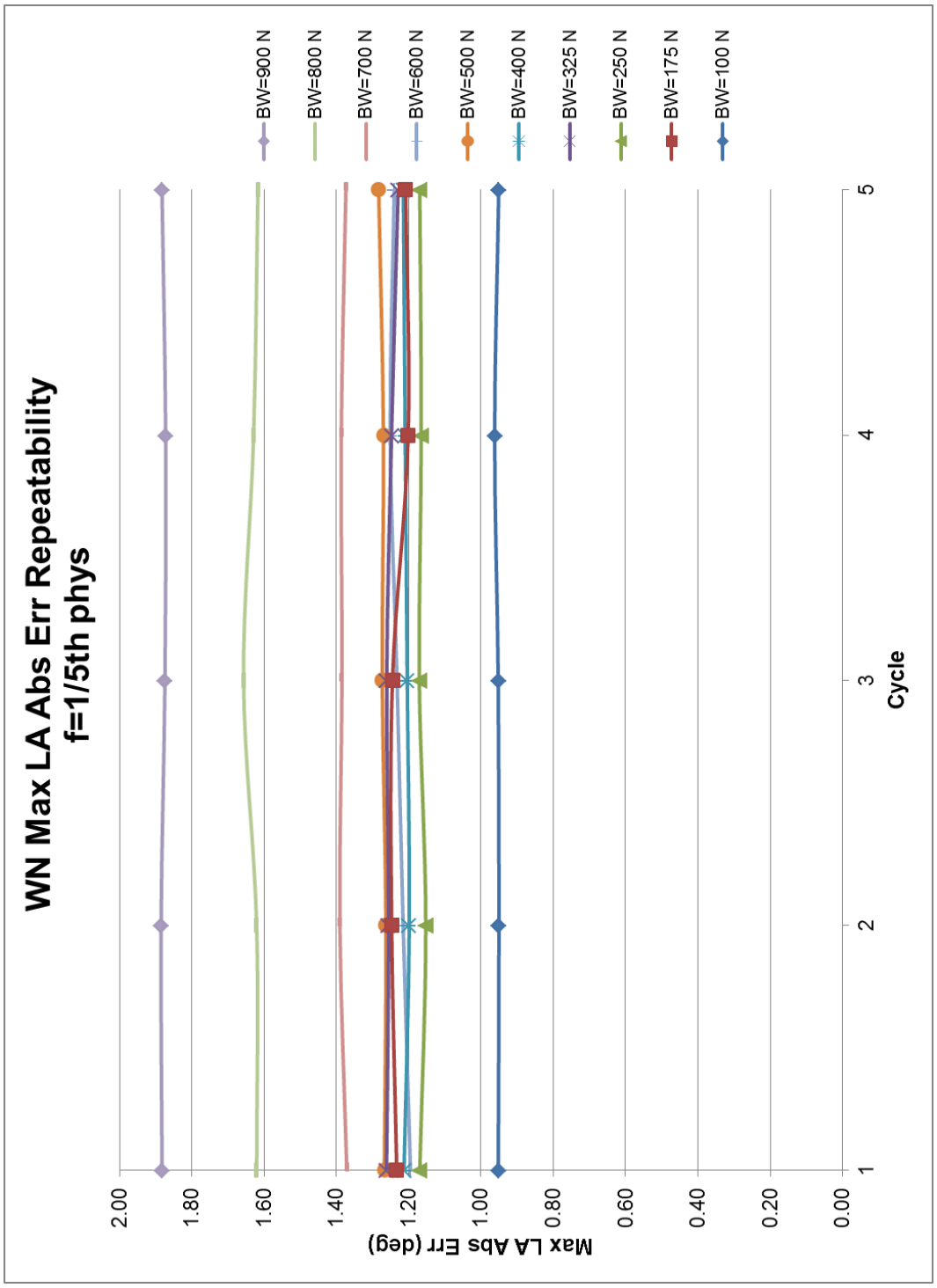

Figure F 21. WN Max LA Abs Err repeatability at 1/5th Phys.

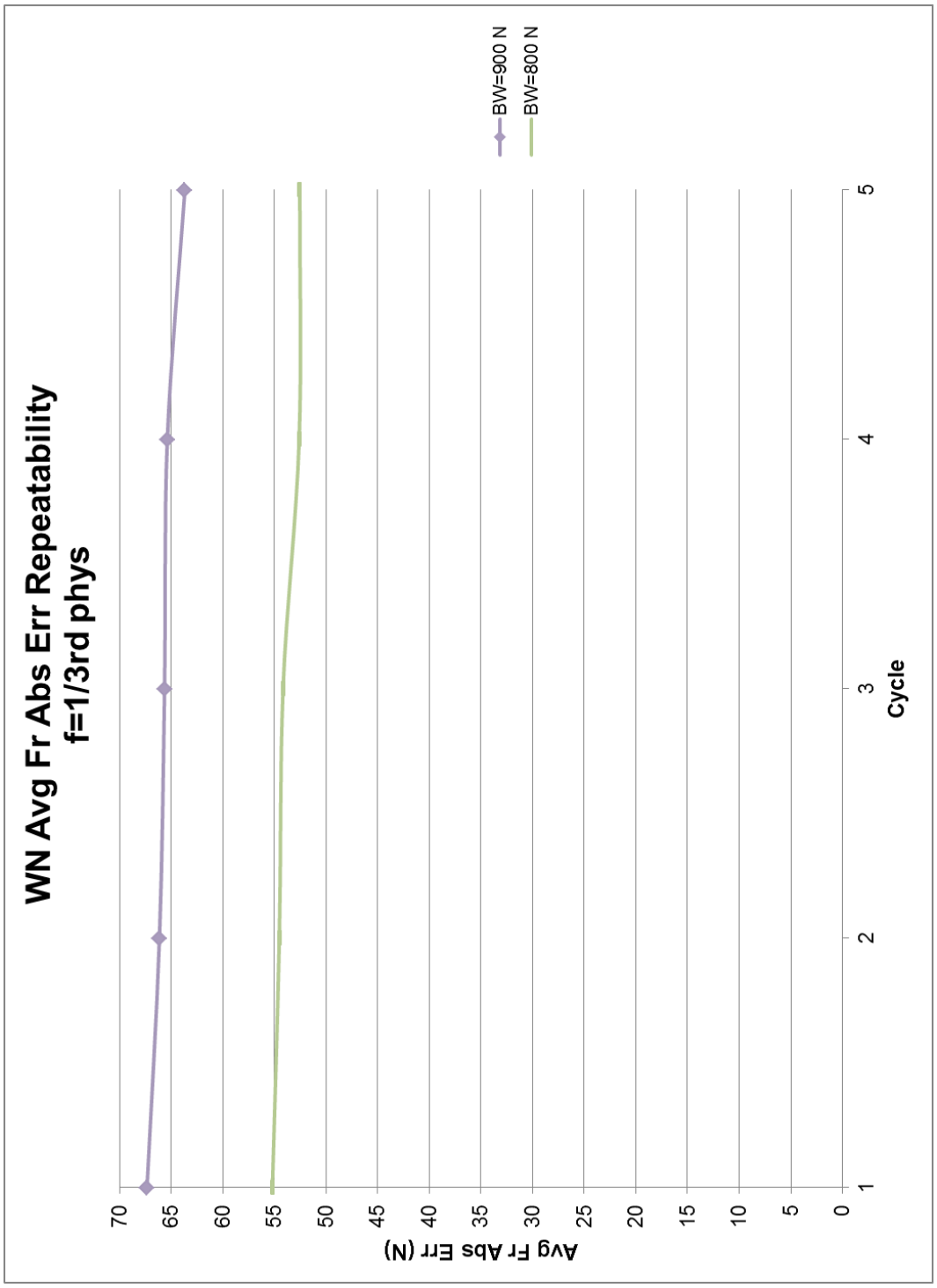

Figure F 22. WN Max F_R Abs Err repeatability at 1/3rd Phys.

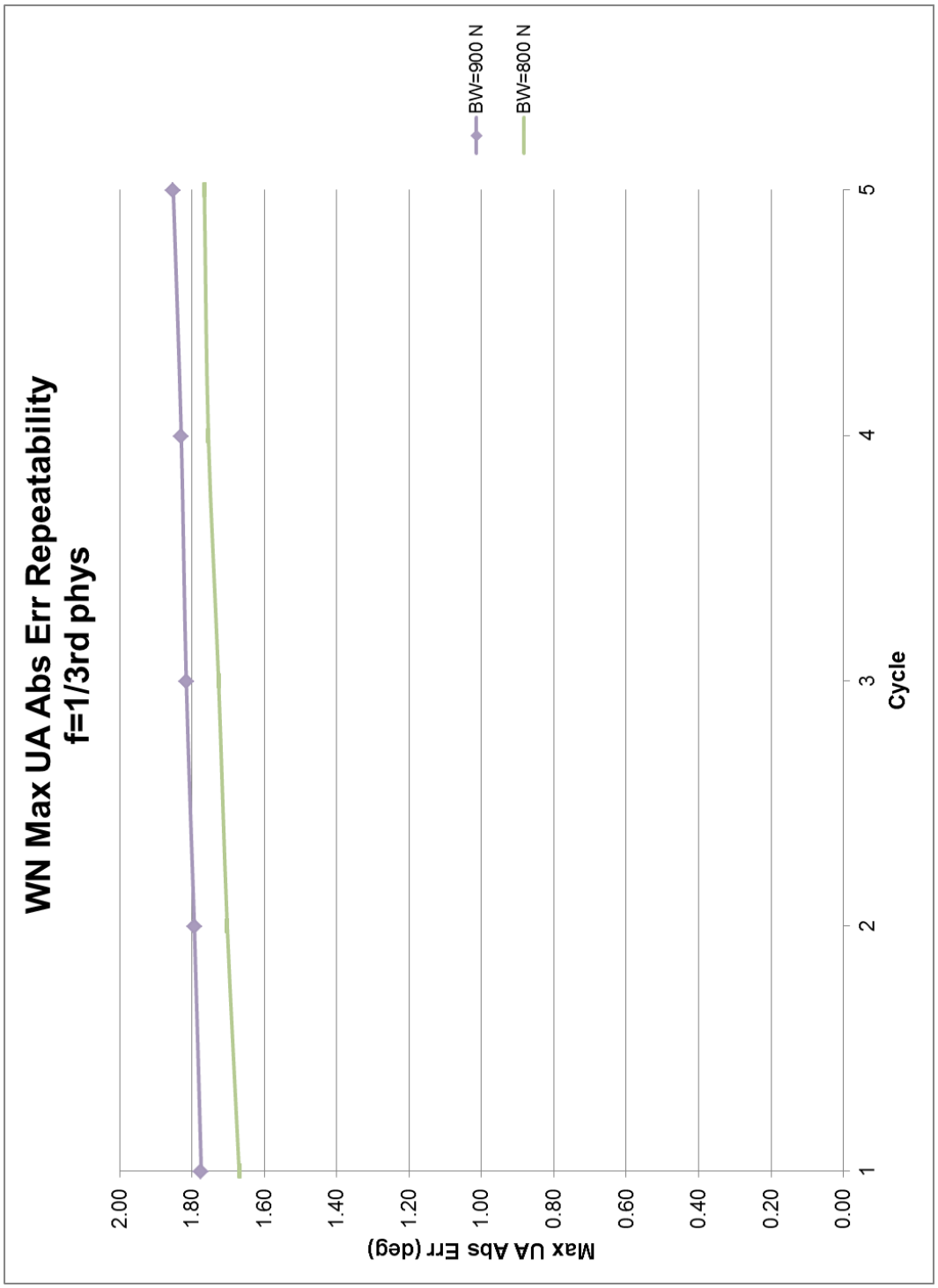

Figure F 23. WN Max UA Abs Error repeatability at 1/3rd Phys.

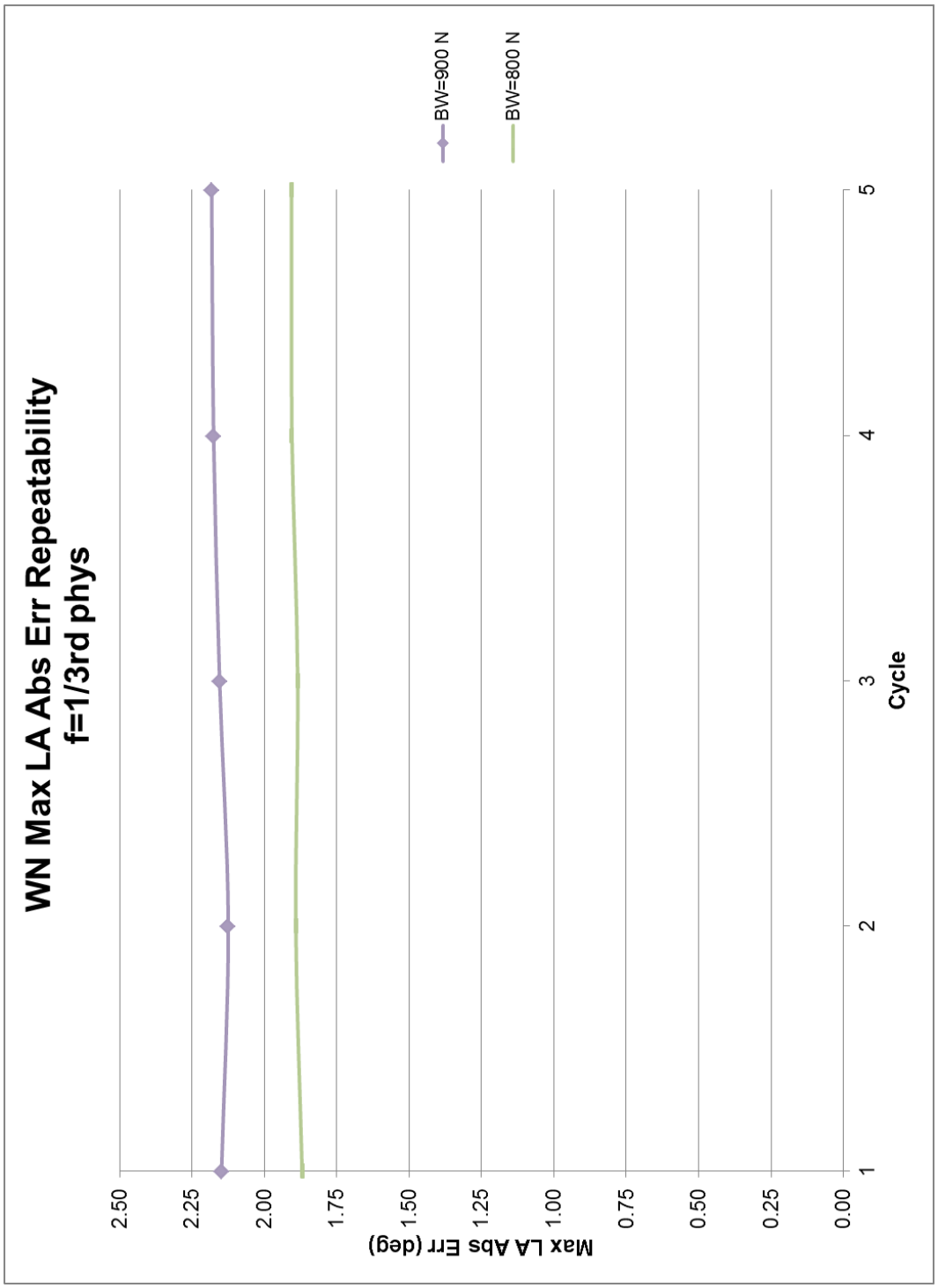

Figure F 24. WN Max LA Abs Err repeatability at 1/3rd Phys.